THE UNIVERSITY OF CHICAGO

BOSE-EINSTEIN CONDENSATES IN A SHAKEN OPTICAL LATTICE

A DISSERTATION SUBMITTED TO
THE FACULTY OF THE DIVISION OF THE PHYSICAL SCIENCES
IN CANDIDACY FOR THE DEGREE OF
DOCTOR OF PHILOSOPHY

DEPARTMENT OF PHYSICS

BY
LICHUNG HA

CHICAGO, ILLINOIS
JUNE 2016

To my family and friends

to explore strange new worlds,

to seek out new life and new civilizations,

to boldly go where no man has gone before.

-Star Trek

TABLE OF CONTENTS

LIST OF FIGURES

LIST OF TABLES

ACKNOWLEDGMENTS

Thanks to my thesis advisor Dr. Cheng Chin, for he sharing his great ideas and attitude of conducting science. Cheng has a very high standard in terms of examining quality of scientific results. I have been very lucky to adopt the scientific methodology from him. Outside physics, I also find him being a very kind person. He tries to be responsible and be available to all the group members. In my last few years of PhD, he is also very generous to let me working on the projects I have been very interested in. I appreciate the opportunities he has been offering in the course of the PhD training. Thanks to my senior lab fellow Dr. Cheng-Lung Hung, for the experience he transferred. I am inspired by his strong motivation about science and his working attitude, style and efficiency. Thanks to my senior lab fellow Dr. Xibo Zhang, for his kind education and careful work in my early stage of the PhD program, I won't be able to be experienced enough without his guidance. I like the genuine way he communicates and his excellent memories about all the tiny detail of his life and work. Thanks to my post doc Dr. Shih-Kuang Tung, for his patience and generosity. Shih-Kuang is a very determined person, and he is very experienced and knowledgeable in every aspect. He is a true leader who inspires colleagues to accomplish difficult tasks. Thanks to my post doc Dr. Colin Parker, for his constantly ingenious advices. I really like the beautiful mind Colin has. He is a very intuitive person who is supported by pieces of well-connected knowledge. I enjoy a lot in his critical comments and discussions. It's very helpful and inspires me to find out solutions. Thanks to my post doc Dr. Eric Hazlett for his kind supports. I appreciate the fact that he is always willing to take responsibility and share other people's burden. I also like the style that he organizes things in the life and try to make sure everything will be covered. Thanks to my post doc Dr. Ulrich Eismann for his encouragement and experimental assistance. Ulrich is a very creative physicist. In the early stage of setting up the optical projection system, he comes up with the idea of combing the imaging camera with the projection optics on a single breadboad, which makes the system robust and stable. While working with him, I get to be exposed to both the German style

robustness and the French style flexibility. Thanks to my post doc Dr. Chen-Yu Xu for his gentle advices about life and career. Chen-Yu is a knowledgeable scholar who has precise concepts about physics and things happening in the world. I like chatting with him and capturing the wisdom from him. Thanks to Logan Clark for the friendship and supports. Logan has a remarkable understanding, intuition and passion on science. He is also a very honest, caring, cheerful, and responsible person. Working with him is joyful. Thanks to Lei Feng, Gustaf Downs, and Klaus Hueck for all the wit, inspiration, and support in the past discussions. Thanks to Dr. Karina Jiménez-García, Dr. Brian DeSalvo, and Jacob Johensen for the nice chats about everything. I do not work directly with them, but I do enjoy the wisdom I received in every chance I ever had to interact with them. I also appreciate the efforts you had ever spent on commenting the paper draft or this thesis draft. Thanks to Dr. Brandon Anderson for his theoretical support. He is intelligent, knowledgeable, and efficient.

Thanks to JFI staffs Hellmut Krebs, Dave Smith, Qiti Guo, Mark Zaskowski, Maria Jimenez, and John Phillips for their supports. I like the way Helmut teaching young students about machining. It's always very gentle and precise. Dave is always very friendly and welcoming students to seek for help about electronics. Qiti is wisest person I meet in the institute and is always willing to share his wisdom about life with students. Mark is a very enthusiastic person. I like him being so energetic all the time. Maria always cares about students. I appreciate the love she has been giving. John has been very helpful in terms of managing the research environment of the institute. It's also very encouraging to see his smile and receive his greeting.

Thanks to Dr. Florian Schreck and his team members. Florian is the most honorable gentleman I have ever seen. I have been very lucky to visit and work with him briefly. He selflessly shares his experimental designs and ideas with the community. In particular, I like to join the lunch discussion he would have with his group members. It's like swimming in the pool of knowledge.

Special thanks to all the friends who have been very supportive in the past few years, especially to Dr. Peter Scherpelz, Dr. Scott Waitukaitis, Dr. Yi-Hung Tan (Carol), Chuan-ren Chung (Isaac), Naiqing Gu (Chris), Dr. Yuh-Chwen Lee (Grace), Chih-Chieh Hsu, Yung-Tsen Chen, Dr. Ru-Ting Huang, and Dr. Michael Reppert for the spiritual support, guidance, and suggestions about life.

Thanks to my family for letting me explore my own journey, especially to my grandfather for his constant support and understanding.

Finally, I want to thank God for giving me the chance to experience the world in a good way and in a bad way.

ABSTRACT

Motivated by the famous physicist Richard Feynman, we are eager to create a universal quantum simulator with ultracold atoms. Because of its versatile controllability and clean environment, ultracold atomic system serves as a versatile plateform for imitating quantum systems with energy scale, time scale and length scale which is many orders of magnitude different. Oftentimes, it's very difficult to conduct direct experiment on the system to be simulated. Through the universality of the physics law, one could reproduce the same physical phenomena in another system which could be tested in a more convenience energy scale, time scale and length scale.

In this thesis, we demonstrate three different examples of quantum simulation. With the help of optical lattices, we measure the equation of states of two-dimensional Bose gases, create effective ferromagnetic domains, and also create roton quasi-particle in the atomic superfluid. The last two items rely on the technique of lattice shaking, and we are able to engineer atomic dispersion and create a double-well structure in the momentum space by dynamically modulating the lattice potential. We take advantage of the high resolution imaging system to study the effective ferromagnetism and many-body excitation in this system.

The essential techniques we use include *in situ* imaging, optical projection, Feshbach resonance, and optical lattice. An 1-μm imaging resolution is achieved by implementing an aberration-compensated objective which also allows projecting optical potentials crafted with a digital micromirror device. The Feshbach resonance and optical lattice, on the other hand, allows us tuning the interaction strength to a strongly interacting regime while keeping the gas stable.

We first characterize the performance of static optical lattices by using it to enhance atomic interaction strength. From the weakly interacting regime to the strongly interacting regime, we study the critical behavior of two-dimensional Bose gas in the Berezinskii-Kosterlitz-Thouless transition and vacuum-to-superfluid transition. We compared the mea-

surements of the critical points with different theoretical predictions. The scaling of the critical point deviates from the mean-field prediction but is still captured by the classical field theory in the strongly interacting regime.

Through dynamically modulating the phase of the optical lattice, we create an effective ferromagnetic system where the quasi-momentum of the atoms represents the pseudo-spin in the corresponding effective ferromagnetism. Using a shallow optical lattice and tuning the atomic scattering length to a small value help the system remain stable. The lifetime of the system is long enough for us to measure the susceptibility and observe formation of domains. We present the analysis of spin correlation function. From the spin correlation function, we find domain walls tend to align along the short axis of the cloud.

We further investigate the many-body excitation spectrum with projection Bragg spectroscopy. The measurement reveals the existence of roton and maxon signatures in the dispersion. The roton and maxon energies scale with the chemical potential linearly which is an indication of many-body effect. The existence of roton leads to suppression of critical velocity of the system and is proved by a moving speckle experiment.

CHAPTER 1

INTRODUCTION

The experimental realization of Bose-Einstein condensate in ultracold dilute atomic gases requires sophisticated laser cooling techniques. It was first achieved in 1995 by Eric A. Cornell and Carl E. Wieman group at JILA [1] and Wolfgang Ketterle group in MIT [2]. They were awarded with Nobel Prize for this contribution in 2001. Later, the cooling method is generalized to create BEC for different atoms, including most of the alkaline metals and some of their isotopes. Hydrogen, metastable helium, some alkaline earth metal including Ca and Sr as well as transition metals Cr, Yb, Dy and Er all become possible to be cooled to condensation.

Creation of degenerate quantum gases opens an avenue for studying many-body physics in a dilute gas system. Starting from observation of collective behavior [3, 4], the condensate oscillation frequencies and damping rates are confirmed to depend on the interaction of the thermal cloud and condensate. Later, resolving the excitation mode of the condensate with Bragg spectroscopy [5, 6] provides better understanding of the BEC excitation.

With the ability to tune the atomic interaction strength through the use of a Feshbach resonance [7], novel dynamical many-body phenomena can be realized in a quantum gas. A Feshbach resonance occurs when two colliding atoms are energetically degenerate to a bound state. Through tuning the magnetic field, the relative energy difference can changed by the Zeeman effect. Donley *et al.* [8] observe "Bosenova" which is the collapse in ^{85}Rb followed by a sudden change of scattering length. Khaykovich *et al.* [9] and Strecker *et al.* [10] realize bright matter wave soliton by tuning the interaction strength to a small and negative value.

Today, the creation of degenerate quantum gas has been standardized. The full recipe of the apparatus [11] or control system [12] as well as numerous theses are available on the web. BEC has been the working horse for studying many-body physics [13], dynamics [14, 15] and novel quantum phenomena in a dilute gas system. Quantum simulation becomes a very powerful idea to take advantage the versatile control ability on the ultracold atoms.

The goal of this thesis is to create a toy model system for performing quantum simulation. With a phase modulated optical lattice, we engineer atomic dispersion and create two modes in momentum space. We observe effective ferromagnetism in this two-mode system and find formation of ferromagnetic domains. We further investigate the excitation in a single domain and measure a roton-maxon dispersion which resembles the excitation in superfluid helium. I will introduce the concept of quantum simulation and the technique of shaken optical lattice in the following sections.

1.1 Quantum simulation with ultracold atoms

In 1981, the Physics Nobel Laureate Richard Feynman envision the great idea of universal quantum simulator [16]: *"It's been noted time and time again that the phenomena of field theory (if the world is made in a discrete lattice) are well imitated by many phenomena in solid state theory (which is simply the analysis of a latticework of crystal atoms, and in the case of the kind of solid state I mean each atom is just a point which has numbers associated with it, with quantum-mechanical rules). For example, the spin waves in a spin lattice imitating Bose-particles in the field theory. I therefore believe it's true that with a suitable class of quantum machines you could imitate any quantum system, including the physical world."*

It's natural to request a universal quantum simulator for better understanding of the physics phenomena. To study a system which is inconvenient to perform experiments, we can test the physics in a more controllable environment. Ultracold atoms provide a clean, controllable and well modeled system for this particular application. Governed by the universality of the physics law, phenomena at very different energy scales and length scales can be created in an atomic cloud.

Cosmology belongs to the category that experiments are difficult to perform. One of the pioneering papers by T. W. B. Kibble describes the scaling between the size of cosmological topological defects, including monopoles, cosmological strings or domain walls, and the

universe cooling rate in a cosmological phase transition [17, 18]. The theory remains theoretically interesting, but was unable to be tested experimentally. Almost a decade later, W. H. Zurek made the connection between cosmological strings and vortex lines in the superfluid, and he proposed to test the theory in superfluid helium [19, 20]. The power-law dependence of topological defect density on the quench time is now named after them as Kibble-Zurek mechanism (KZM). KZM has been tested in ultracold atomic cloud with the defect in the form of soliton [21], vortex [22], and domains [23].

Going to the other extreme, physics on the length scale of atomic nucleon can also be studied with ultracold atoms. Motivated by the natural abundance of stable isotopes ^{12}C (three α particles) and ^{3}H (three nucleons), Vitaly Efimov predicts the existence of three-body bound states when two-particle interaction strength diverges [26]. He also explicitly claims that an additional bound state shows up when the scattering length is $e^{\pi} \approx 22$ times larger. It would have been very difficult to test the theory in an atomic nucleus since the nucleon scattering length can't be tuned easily. Fortunately, the atomic scattering length can be tuned through Feshbach resonance. First demonstrated in Cesium atoms, the three-body bound state has been confirmed [24]. Numerous further investigations of Efimov resonances are also reported [27, 28, 29, 30, 31, 32, 33, 34] thereafter. Further demonstrations of geometric scaling of Efimov states in a homo-particle [27, 32] and hetero-particle system [25] were also performed.

In the intermediate energy scale, there are also rich physics phenomena predicted for condensed matter systems. An important research topic is creation of artificial gauge field for ultracold neutral atoms. One of its goals is to realize Hofstadter-Harper Hamiltonian [35, 36] that describes the existence of fractal energy spectrum of electrons in irrationally magnetic fields (~10000 T) [43]. The concept of artificial gauge field, however, can bypass the need of high magnetic field. Exploiting the resemblance between the Lorentz force and the Coriolis force, vortex lattices [37, 38] in a rotating trap represent the superfluid version of flux lattices in the superconductor. Rotation becomes the analogy of the external

weak magnetic field. In pursuit of even higher effective local magnetic field, proposals of using Raman laser [39, 40], shaken optical lattice [41] or photon-induced tunneling in a superlattice potential [42] are experimentally conducted. With the use of laser-assisted tunneling in optical lattice, the Harper Hamiltonian is realized [43, 44], and the equivalent effective magnetic field corresponds to more than 1000 T.

1.2 Manipulating ultracold atoms with optical lattices

Optical lattice plays an important role in studying many-body physics with ultracold atoms. Neutral atoms in the periodic optical potential resemble electrons in the ionic lattice of a crystal in many perspectives, and both systems can be analyzed with the concept of band structure. The dynamics of ultracold bosonic atoms in the optical lattice can be described by a Bose-Hubbard model [45]. One important prediction from Bose-Hubbard model is the existence of Mott insulator phase that corresponds to a commensurate filling in the lattice. The theory drives motivation to experimentally confirm the existence of Mott insulator phase through measuring the loss of atomc coherence [46, 47] as well as the "wedding cake" density distribution signature in the optical dipole trap [48].

In addition to providing a platform for quantum simulation, optical lattice also allows versatile experimental controls. Through squeezing the atomic wavefunction in a tightly confined lattice potential, the atomic interaction can be dramatically enhanced. The interaction can be strong enough to prevent bosons coexisting in the same position. Fermionization of Tonks-Girardeau gas [49, 50] for one-dimensional bosons in a strongly interacting regime is experimentally observed in an optical lattice [51, 52].

Strong confinement from the optical lattice also provides the option to study a low dimensional system. When the ground state energy of the confinement is much larger than the rest energy scales including temperature, chemical potential, the dynamics in that dimension is frozen and can be ignored. Tuning the dimensionality of the quantum gas allows pivoting the symmetry of the Hamiltonian. In two dimensions, the scale invariance of the

equation of state in a Bose gas [53] originates from the continuous scaling symmetry between interaction and kinetic energy. In one dimension, a matter-wave bright soliton is possible to exist. A matter-wave soliton describes the dispersiveless phenomena when the matter-wave propagates in space [9, 10]. The nonlinear attractive interaction stabilizes the waveform of a one-dimensional gas during propagation. However, the imbalance between the attractive force and repulsive quantum pressure in a higher dimension would lead to implosion and dissipation.

1.3 Manipulating ultracold atoms with a shaken optical lattice

There are also a lot of degrees of freedom to access inside the optical lattice. The band structure theory gives good understanding about the energy and momentum state which atoms can populate. Through dynamically modulating the phase or amplitude of the lattice potential, atoms can be transferred between different states [54].

In a continuously driven system, Gemelke *et al.* also demonstrated parametric amplification in matter waves [55]. Through phase modulating the one-dimensional lattice in a frequency below vibrational resonance, atoms are prepared in a dressed band structure which gives an unstable equilibrium. Spontaneously population and amplification of atoms at the edges in the Brillouin zone happens due to collisions.

A different perspective of the band structure engineering is modification of the tunneling process in the optical lattice. Lignier *et al.* measure the dynamic suppression of tunneling in a shaken optical lattice [56]. Lattice shaking allows controlling the tunneling matrix while leaving the on-site interaction energy unchanged.

Recently, creation of novel quantum states and quantum phase transitions also becomes possible in a shaken triangular optical lattice. Through independent control of tunneling coefficients in a triangular lattice, J. Struck *et al.* are able to engineer the local phase of atoms in the single lattice site which resembles the classical vectors spin [41]. Depending on the relative strength of the tunneling energy, the system can go through transition from

ferromagnetic phase to anti-ferromagnetic phase or even exotic quantum phases. The same system is also used to realize a frustrated Ising-XY model [57].

A shaken optical lattice serves as an excellent tool for quantum engineering and allows new direction for realizing a universal quantum simulator. The goal of the thesis is to construct a new toy system based on a shaken optical lattice. We managed to create an effective ferromagnetic system and study its many-body excitation spectrum.

1.4 Our approach of quantum simulation with optical lattices

This thesis contains three directions for performing quantum simulation with optical lattices, including the equation of state measurements, creation of density order in an effective ferromagnetism, and creation of new type of quasi-particle.

Equation of state is used to characterize the thermodynamic properties of the system. In two dimensions, there exists a universal function of $\tilde{n}(\tilde{\mu})$ describing the state equation of the Bose gas at a fixed interaction strength, where $\tilde{n}$ is the atomic density normalized by the de Broglie wavelength, and $\tilde{\mu}$ is the chemical potential normalized by the thermal energy. Two distinct phases lie on different sides of the equation of state, including normal ($\tilde{\mu} \ll 0$) and superfluid ($\tilde{\mu} \gg 0$). The equation of state has been well characterized in the weakly interacting regime, and excellent agreement between theories and experiments has been demonstrated. However, disagreements between different theories show up when the interaction strength is large. We take advantage of the enhanced interaction strength from the optical lattices to create a stable strongly interacting two-dimensional Bose gas. At different sections of the equation of state, we extract the dependence of different physical quantities as a function of the interaction strengths.

We then proceed to realization of effective ferromagnetism in a quantum gas. Although the microscopic physics of the ferromagnetic system has been studied extensively, it's still fascinating to see long-range order builds up based on a short-range interaction. Spinor condensates have been used to simulate ferromagnetism, and the formation of domain or

spin texture were found with contact and dipole interactions. However, the long equilibration time, due to the weak spin-dependent interaction strength, makes the system hard to reach the ground state. To introduce a strong effective spin interaction, we engineer the atomic dispersion to create a double-well structure in the momentum space. The two ground states constitute pseudo-spins in our single component quantum gas. We characterize the phase transition, observe domain formation, and analyze the magnetization correlation function.

The ferromagnetic system also manifests existence of a new type of quasi-particle which resembles the roton excitation in superfluid helium. Landau first hypothesizes the existence of roton in the superfluid helium system based on the specific heat measurements. Later, a neutron scattering measurement verifies the roton signature in the excitation spectrum. Until now, the underlying mechanism of roton formation remains interesting. In our system, roton dispersion forms by having many-body interaction lifting the degeneracy between the two ground states. When the majority of the atoms occupy one of the wells, the symmetry breaks, and occupation of atoms in the other well costs energy. We call the excitation as roton. We study the dependence of the roton energy on the many-body interaction. We also measure the critical velocity limited by the roton mode.

1.5 Overview of the thesis

The main part of the thesis is based on investigation of an effective ferromagnetic system created with a shaken optical lattice. Before discussing about it, we will go through the theoretical background of the Bose-Einstein condensate, optical lattice, and the experimental setup.

Chapter 2 introduces the basic theoretical tools for understanding and manipulating degenerate Bose gases. We start with non-interacting Bose particles and calculate the condensation temperature. We then introduce interaction in our consideration. Through approximating the contact interaction with mean-field, we simplify the Schödinger equation with Gross-Pitaevskii equation. To understand the many-body excitation spectrum in the later

chapter, we use second quantization to calculate the Bogoliubov excitation spectrum. We will also briefly mention the Berezinskii-Kosterlitz-Thouless transition and superfluid-to-Mott insulator transition for understanding the experiment of strongly interacting two-dimensional gas.

Chapter 3 introduces Feshbach resonance and the theory of optical dipole force and optical lattice. We calculate the AC Stark effect from a far off-resonant laser which serves as a convenient tool for trapping and manipulating ultracold atoms. Moreover, imposing an optical standing wave on ultracold atoms modifies the dispersion of the atoms as well as the effective mass and effective interaction strength. The definition of atomic momentum is also replaced with quasi-momentum which is limited in the range of the photon recoil momentum. The atomic dispersion can be further modified through phase modulating the lattice. We use two-level model and Floquet model to calculate the dispersion.

Chapter 4 introduces experimental setup of the BEC system. We start with introducing the hardware including the vacuum system, laser system, control system and the magnetic field control. We then proceed to the cooling methods. Zeeman slowing enhances the atomic flux which is trappable by the magneto-optical trap. With sub-Doppler cooling from optical molasses and and degenerate Raman sideband cooling, we reach a temperature of 1 μK (a phase space density of 0.03) and are ready to perform evaporation. After forced evaporation, the caesium gas temperature reaches 10 nK and is fully condensed in the ground state. We will also spend a section to explain how we load the condensate to a quasi-two-dimensional trap. We then switch the gear and introduce the tools we used to probe and manipulate atoms. For probing, we introduce the absorption imaging technique and characterize the response function of the imaging system. For manipulating, we explain our method of creating optical lattice and lattice modulation. We also present the characterization of heating of atoms in the shaken optical lattice. Lastly, we introduce our projection system for creating an arbitrary optical potential with a digital micromirror device. With its dynamic controllability, we measure the excitation spectrum of the condensate.

Chapter 5 discusses the application of optical lattice on enhancing the atomic interaction strength for measuring the state equation of a strongly interacting two dimensional Bose gas. We perform measurements of the critical chemical potential and the critical density in the Berezinskii-Kosterlitz-Thousless transition and the superfluid-to-vacuum quantum phase transition. The combination of using optical lattice and Feshbach resonance allows us the access the strongly interacting regime while keeping atoms stable.

Chapter 6 discusses the application of a shaken optical lattice on the creation of effective ferromagnetism and observation of ferromagnetic domains. Through lattice shaking, we create a double-well dispersion. Atoms condensing at different wells can be represented as different pseudo-spins. We detect the density distribution of the pseudo-spin with time-of-flight. Through analyzing the relative strengths between Bragg peaks, we reconstruct the domain distribution. We also present the susceptibility measurement of atoms in the pseudo-spin component. In the end of the chapter, we analyze the correlation function of the domain structure. The domain wall tends to align along the short axis in order to reduce the energy cost.

Chapter 7 discusses the observation of roton-maxon excitation spectrum. We implement the projection Bragg spectroscopy to measure atomic dispersion. We observe roton and maxon signatures in the dispersion. To test that roton is a many-body effect, we measure the dependence of roton energy and maxon energy on the atomic interaction strength. We find both energies scale with the chemical potential linearly which agrees with the theory. Lastly, we measure the critical velocity with a moving speckle pattern. The suppression of the critical velocity due to the existence of roton dispersion is in agreement with Landau criteria.

Chapter 8 discusses the outlook of this research line and preliminary results on the observation of long-live coherent density order from roton. In an excited state, rotons can coexist with domain walls.

CHAPTER 2

BOSE-EINSTEIN CONDENSATE IN THREE AND TWO DIMENSIONS

To understand the properties of a quantum gas, we dedicate this chapter to explain the theory part of the system. We first present the Bose statistics and explain the mechanism of forming a Bose-Einstein condensate with a non-interacting gas. We then introduce interactions into our consideration. We use partial wave analysis to construct the concept of the scattering length which describes the interaction strength between atoms. In the mean-field picture, the macroscopic wavefunction can be tuned with single particle interaction. To simplify the many-body system, we use Gross-Pitaevskii equation to approximate the system at different limits. Lastly, we introduce the many-body excitations including phonon and vortex.

2.1 Bose-Einstein condensate in three dimensions

Back in 1924, Satyendra N. Bose introduced Bose statistics, and Albert Einstein predicted the existence of phase transition of non-interacting bosonic particle [59, 60, 61]. The Bose-Einstein statistics shows significant difference from the classical Maxwell-Boltzmann statistics at low temperatures. At low temperature or high density, a striking fact is the concept of number saturation in the excited states. Only a finite number of particles can occupy the excited states at a fixed temperature. When the phase-space density of the gas exceeds the critical value, particles condense in the ground state.

Formation of the Bose-Einstein condensate corresponds to a statistical phase transition. With a significant occupation of the ground state, the macroscopic wavefunction shares a common phase and shows coherence. To confirm the existence of coherence, earlier experiment demonstrates the interference between two independently prepared condensates [62]. The interference pattern is determined by the de Broglie wavelength defined by the velocity of the cloud.

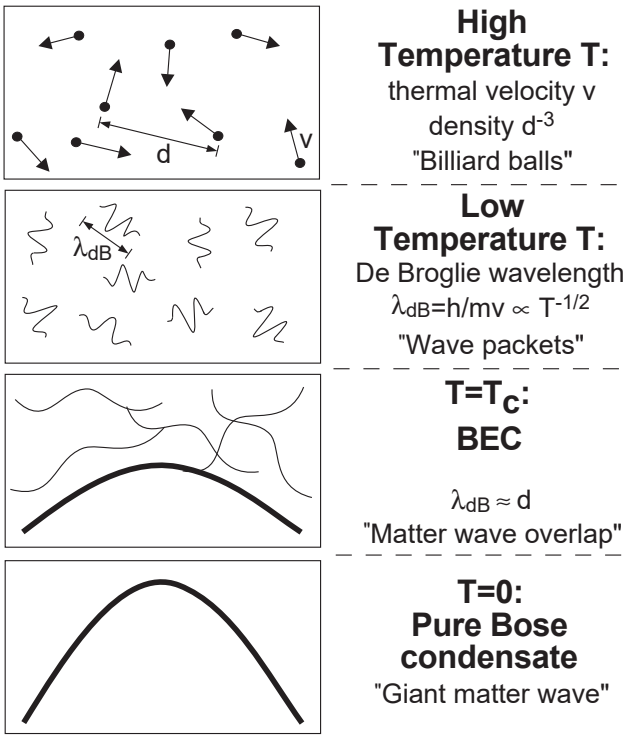

Figure 2.1: Particle-wave duality of Bose particles at different temperature. When the temperature reaches the critical temperature, the gas shows matter wave coherence among the sample. Figure reprinted from Ref. [58].

To quantitatively understand this phenomenon, we follow the treatment of Pethick [63]. We start with the Bose-Einstein distribution:

$$f(\epsilon_\nu) = \frac{1}{\exp[(\epsilon_\nu - \mu)/k_B T] - 1}, \tag{2.1}$$

where $f(\epsilon_\nu)$ gives the mean occupation number for non-interacting bosons at a single-particle state ν, ϵ_ν corresponds to the energy of the state ν, μ is the chemical potential of the system, k_B is the Boltzmann constant, and T is the temperature.

In three dimensions and homogeneous system, one state occupies a volume of $(2\pi\hbar)^3$ in phase space, where $h = 2\pi\hbar$ is the Planck constant. Given the volume of momentum space $4\pi p^3/4$ determined by the maximum momentum $p = \sqrt{2m\epsilon}$, one can immediately find the

total number of states $G(\epsilon)$ in an energy shell up to energy ϵ equal to

$$G(\epsilon) = V\frac{4\pi}{3}\frac{(2m\epsilon)^{3/2}}{(2\pi\hbar)^3} = V\frac{\sqrt{2}}{3\pi^2}\frac{(m\epsilon)^{3/2}}{\hbar^3}, \tag{2.2}$$

where m is the atomic mass, ϵ is the maximum kinetic energy, and V is the volume of the system. From the expression, we can calculate the density of states $g(\epsilon)$, which describes the degeneracy of a state of energy ϵ:

$$g(\epsilon) = \frac{dG(\epsilon)}{d\epsilon} = \frac{Vm^{3/2}}{\sqrt{2}\pi^2\hbar^3}\epsilon^{1/2} = C\epsilon^{1/2}, \tag{2.3}$$

where $C = \frac{Vm^{3/2}}{\sqrt{2}\pi^2\hbar^3}$.

Consider a system with $\mu = 0$, the total particle number in the excited states at temperature T is

$$N_{ex} = \int_0^\infty d\epsilon g(\epsilon) f(\epsilon) = C\Gamma(3/2)\zeta(3/2)(k_B T)^{3/2}, \tag{2.4}$$

where $\Gamma(x)$ is the gamma function, and $\zeta(x)$ is the Riemann zeta function. The numerical numbers can be found in the math table, and we have $\Gamma(3/2) = \sqrt{\pi}/2$ and $\zeta(3/2) = 2.612$.

A more conventional expression of the equation is to rewrite it as a phase space density $\bar{\omega} = n\lambda^3$ which describes number of particle contained in the volume equal to the cube the the thermal de Broglie wavelength $\lambda = h/\sqrt{2\pi m k_B T}$, where $n = \frac{N}{V}$ is the atomic density. When $\bar{\omega} > \bar{\omega}_c = \zeta(3/2) = 2.612$, particle condenses. For cesium atom with mass $m = 133$ amu and a typical atomic density $n = 10^{13}$ cm^{-3}, the critical temperature is $T_c \approx 60$ nK.

To increase T_c, one could try increasing the atomic density. However, inelastic collisions will eventually prevent the system reaching a high atomic density. In cold atoms, the dominant loss mechanism is three-body loss: three particles collide, two particles could form a molecule. The release energy would be distributed to the molecule and the remaining atom. Because three particles must be at the same point in space, the loss rate scales with density cube.

In recent condensed experiments, the realization of a BEC at room temperature has been achieved [64]. Through creating quasi-particles, such as exciton-polariton which is a mixture of electronic excitation and photon, the condensation critical temperature can be dramatically enhanced due to the high particle density (10^{19} cm^{-3}) and the low effective mass (10^{-11} times the atomic mass). However, the finite quasi-particle lifetime means that one would have to continuously pump the system with new quasi-particles in order to compensate the dissipation originated from the short lifetime (~ps).

2.2 Berezinskii-Kosterlitz-Thouless transition in two dimensions

We discuss superfluid vortex excitation, which is a topological defect with quantized angular momentum. Given a wavefunction $\psi(r) \sim e^{i\phi(r)}$, the corresponding velocity field can be written as $\vec{v}(r) = (\hbar/m) \cdot \vec{\nabla}\phi(r)$. To ensure that wavefunction is single valued, the phase accumulation of the wavefunction around the vortex needs to be a multiple of 2π. For the lowest excitation, one then find the velocity of the wavefunction equal to $\vec{v}(r) = \hbar/mr\vec{\theta}$, where r is the distance from the vortex core. The velocity near the center of the vortex diverges, and the density vanishes. The size of the vortex equals to the healing length ξ.

As was pointed out by Berezinskii, Kosterlitz and Thouless [68, 69], the vortex and anti-vortex can form bound pairs in a two-dimensional Bose fluid. The superfluidity remains when the vortex exists in the form of bound state. However, vortex and anti-vortex start to unbind from each other in the sample when the temperature exceed a certain critical temperature T_{BKT}.

To estimate the critical temperature, we calculate the excitation energy E_v and the entropy S_v of a free vortex:

$$E_v = \int_{\xi}^{R} \frac{1}{2} n_s \left(\frac{\hbar}{mr}\right)^2 d^2r = kTn_s\lambda_{dB}^2 \ln\frac{R^2}{\xi^2}; \tag{2.5}$$

$$S_v = \ln\frac{R^2}{\xi^2}, \tag{2.6}$$

where R is the system size, ξ is the healing length, and n_s is the superfluid density.

Consider the free energy of the vortex:

$$F = E_v - TS_v = kT(n_s\lambda_{dB}^2 - 4)\ln\frac{R^2}{\xi^2}, \tag{2.7}$$

where $\lambda_{dB} = \frac{h}{\sqrt{2\pi m k_B T}}$ is the de Broglie wavelength. The proliferation of free vortices become energetically favorable when the superfluid phase space density $n_s\lambda_{dB}^2$ exceeds 4. One then finds:

$$T_{BKT} = \frac{h^2 n_s}{8\pi m k_B}. \tag{2.8}$$

The system remains in the superfluid phase at $T < T_{BKT}$, and it enters the normal phase when $T > T_{BKT}$.

A more elaborated theory discusses the modification of the critical point by the interaction. A microscopic theory introduced by Popov [70] argues that the critical density should follow the interaction strength logarithmically [70]:

$$n_c\lambda_{dB}^2 = \ln\frac{\xi\hbar^2}{mg}, \tag{2.9}$$

where ξ is a universal constant, m is the atomic mass, and g is the dimensionless interaction strength. For the critical chemical potential, one can also write down the explicit form

$$\frac{\mu_c}{k_B T} = \frac{g}{\pi}\ln\frac{\xi_\mu\hbar^2}{mg}, \tag{2.10}$$

where ξ_μ is also a universal constant. A Monte Carlo simulation based on the classical ϕ^4 theory determines the constant to be $\xi = 380 \pm 3$ and $\xi_\mu = 13.2 \pm 0.4$ [71, 72].

2.3 Gross-Pitaevskii Equation

To calculate interactions in a many-body system, we use the mean-field theory to reduce the many-body problem into a single particle problem. A mean-field approximates the interactions of all the other particles with an average background field. With the contact interaction redefined, the Schrödinger equation is now rewritten in the following form:

$$\left[-\frac{\hbar^2}{2m}\nabla^2 + V_{ext}(r) + \frac{4\pi\hbar^2 a}{m}|\psi(r)|^2\right]\psi = \mu_0\psi(r), \tag{2.11}$$

where $V_{ext}(r)$ is the external trapping potential, the nonlinear term $|\psi|^2$ represents the background mean-field, and μ_0 is the chemical potential of the gas. With the inclusion of the nonlinear interaction term, this nonlinear Schrödinger equation is better known as Gross-Pitaevskii equation (GP equation).

For a slowly varying external potential, the contribution from the kinetic energy of the GP equation can be ignored. Known as the Thomas-Fermi Approximation, the local atomic density is given approximately by

$$n(r) = |\psi(r)|^2 = \frac{m}{4\pi\hbar^2 a}(\mu_0 - V_{ext}(r)). \tag{2.12}$$

In a harmonic trap, the density $n(r)$ is equivalent to an inverse parabola up to the Thomas-Fermi radius $R_{\mathrm{TF}} = \sqrt{\frac{2\mu_0}{m\omega_0^2}}$, where ω_0 is the trap frequency. However, the interaction energy at the edge of the cloud no longer overwhelms the kinetic energy due to the lower density, and this approximation fails. This can be estimated by setting $-\frac{\hbar^2}{2m}\nabla^2 = \frac{4\pi\hbar^2 a}{m}|\psi(r)|^2$. For a steep potential, the spatial variation of the wavefunction is limited by the kinetic energy. The healing length $\xi = \frac{1}{\sqrt{8\pi na}}$ characterizes the natural length scale of the edge. With a typical density of 10^{13} cm^{-3} and a scattering length of 200 a_0, $\xi \sim 600$ nm which is much smaller than the resolution of conventional imaging system which is on the order of few μm.

In an equilibrated sample, one can apply local density approximation (LDA) and treat

the local patch of the BEC as a homogeneous gas in equilibrium with other patches. When the chemical potential is large compared to the harmonic oscillator spacing $\hbar\omega$, $V_{ext}(r)$ can be considered as an offset of local chemical potential, and one can assign a local chemical potential $\mu(r) = \mu_0 - V_{ext}(r)$ to the gas.

2.4 Bogoliubov excitation spectrum

To understand the elementary excitations of a BEC, we introduce the Bogoliubov approximation to calculate the excitation spectrum. We perform this calculation based on the framework of second quantization. Consider N particles in a box of volume V, the wavefunction can be decomposed to the linear combination of plane waves:

$$\psi(r) = \frac{1}{V^{1/2}} \sum_p e^{ip\cdot r/\hbar} \hat{a}_p. \tag{2.13}$$

The second quantized Hamiltonian in free space can be written as

$$\hat{H} = \sum_p \epsilon_p^0 \hat{a}_p^\dagger \hat{a}_p + \frac{U_0}{2V} \sum_{p,p_1,p_2} \hat{a}_{p_1+p}^\dagger \hat{a}_{p_2-p}^\dagger \hat{a}_{p_1} \hat{a}_{p_2}, \tag{2.14}$$

where $\epsilon_p^0 = p^2/2m$ is the kinetic energy, and $U_0 = \frac{4\pi\hbar^2 a}{m}$ is the interaction strength. The operator $\hat{a}_p$ and $\hat{a}_p^\dagger$ is the respective annihilation and creation operator for particle of momentum p, and they satisfy the following commutation relations:

$$[\hat{a}_p, \hat{a}_{p'}^\dagger] = \delta_{p,p'}, \ [\hat{a}_p, \hat{a}_{p'}] = 0, \ [\hat{a}_p^\dagger, \hat{a}_{p'}^\dagger] = 0. \tag{2.15}$$

The statistical BEC transition suggests the number of the ground state particle, N_0 is macroscopically occupied, i.e. $N_0 \gg 1$. Therefore:

$$\hat{a}_0^\dagger |N_0\rangle \approx \sqrt{N_0} |N_0 + 1\rangle \text{ and } \hat{a}_0 |N_0\rangle = \sqrt{N_0} |N_0 - 1\rangle, \tag{2.16}$$

since $N_0 \pm 1 \approx N_0$, where N_0 is the number of particle in the condensate. We approximate $\hat{a}_0^\dagger$ and $\hat{a}_0$ with $\sqrt{N_0}$, and the Hamiltonian can be further simplified as

$$\hat{H}_{\text{Bog}} = \frac{N_0^2 U_0}{2V} + \sum_{p\neq 0}\left[\left(\epsilon_p^0 + 2n_0U_0\right)\hat{a}_p^\dagger\hat{a}_p + \frac{n_0U_0}{2}\left(\hat{a}_p^\dagger\hat{a}_{-p}^\dagger + \hat{a}_p\hat{a}_{-p}\right)\right], \tag{2.17}$$

where $n_0 = N_0/V$ is the density of ground state particles. Note that the total number of particles is

$$N = \sum_p \hat{a}_p^\dagger\hat{a}_p = N_0 + \sum_{p\neq 0}\hat{a}_p^\dagger\hat{a}_p, \tag{2.18}$$

and we further rewrite the Hamiltonian as

$$\hat{H}_{\text{Bog}} = \frac{N^2 U_0}{2V} + \sum_{p\neq 0}\left[\left(\epsilon_p^0 + n_0U_0\right)\hat{a}_p^\dagger\hat{a}_p + \frac{n_0U_0}{2}\left(\hat{a}_p^\dagger\hat{a}_{-p}^\dagger + \hat{a}_p\hat{a}_{-p}\right)\right]. \tag{2.19}$$

The first term represents the overall mean-field energy shift of the condensate and can be ignore in the following calculations.

To diagonalize $\hat{H}_{\text{Bog}}$ we define a new set of operators $\hat{b}_p$ and $\hat{b}_{-p}^\dagger$:

$$\begin{aligned}\hat{b}_p &= u_p\hat{a}_p + v_p\hat{a}_{-p}^\dagger, \\ \hat{b}_{-p}^\dagger &= u_p\hat{a}_{-p}^\dagger + v_p\hat{a}_p.\end{aligned} \tag{2.20}$$

The excitation energy of the diagonalized operators can then be written as

$$\hat{H}_{\text{Bog}} = \sum_{p\neq 0}\epsilon_p\hat{b}_p^\dagger\hat{b}_p. \tag{2.21}$$

With additional constraint to have the new operators satisfying the standard commutation relations:

$$\left[\hat{b}_p, \hat{b}_{p'}^\dagger\right] = \delta_{p,p'}, \quad \left[\hat{b}_p,\ \hat{b}_{p'}\right] = 0. \tag{2.22}$$

We arrive the result that

$$u_p = \cosh t, \;\; v_p = \sinh t, \tag{2.23}$$

where t can be written in the following implicit form

$$\tanh t = \frac{n_0 U_0}{\left(\epsilon_p^0 + n_0 U_0\right)}. \tag{2.24}$$

The excitation spectrum ϵ_p is found to be

$$\epsilon_p = \sqrt{\epsilon_p^0 \left(\epsilon_p^0 + 2 n_0 U_0\right)}. \tag{2.25}$$

In the low momentum limit $p \sim 0$, the dispersion is linear, and the slope corresponds to the speed of sound of the phonon mode:

$$c = \sqrt{\frac{n_0 U_0}{m}}. \tag{2.26}$$

The fact that $c \neq 0$ gives us the hint of superfluidity. With an obstacle moving with a velocity slower than the c in the condensate, there is no available state for the condensate to be excited to. The speed of sound c then corresponds to the critical velocity.

In the high momentum limit, the excitation recovers a particle-like behavior, and the excitation energy scales with momentum square $\epsilon_p \propto p^2$.

2.5 Superfluid-Mott insulator transition

One can model bosons confined in the optical lattice with Bose-Hubbard model [45]. The Hamiltonian can be written as

$$H = -J \sum_{<i,j>} \hat{a}_i^\dagger \hat{a}_j + \sum_i \epsilon_i \hat{n}_i + \frac{1}{2} U \sum_i \hat{n}_i (\hat{n}_i - 1), \tag{2.27}$$

where $\hat{a}_i^\dagger$ ($\hat{a}_j$) is the creation (annihilation) operator in the lattice site i (j), $\hat{n}$ is the number operator, ϵ denotes the energy offset due to the external harmonic confinement, and U is the on-site interaction energy.

The interaction energy U depends on the spread of the wavefunction in the individual lattice site. A stronger confinement gives a higher U. The tunneling energy J, which calculates the rate atoms hop from one site to another, would be suppressed in a deep lattice. In a deep enough lattice where the interaction energy overwhelms the tunneling energy, there is a quantum phase of Mott insulator which has distinct properties compared to the superfluid phase in the weak lattice.

In the superfluid phase, atoms can tunnel between different sites and remain coherent. In a homogeneous sample (ϵ_i = constant), the wavefunction for N particles distributing in M lattice sites is well approximated by

$$|\Psi_{SF}\rangle \propto \left(\sum_{i=1}^{M} \hat{a}_i^\dagger\right)^N |0\rangle. \tag{2.28}$$

The number fluctuations of this state follow Poisson statistics, and the variance equals the mean particle number in a single site.

In the Mott insulator phase, the ground state wavefunction can be described with an integer number of particle filling an individual lattice site. For a density of n particles per lattice site, the wavefunction is written as

$$|\Psi_{MI}\rangle \propto \prod_{i=1}^{M} \left(\hat{a}_i^\dagger\right)^n |0\rangle. \tag{2.29}$$

Since the interaction energy scales with number of pair in the individual lattice site, the atom number fluctuation in the Mott insulator phase is suppressed in order to avoid the excess energy costed by having a large number of particles occupying in a single site. The gas also loses coherence between sites in the Mott insulator phase [46, 47].

Superfluid-Mott insulator transition is one of the prototype quantum phase transitions

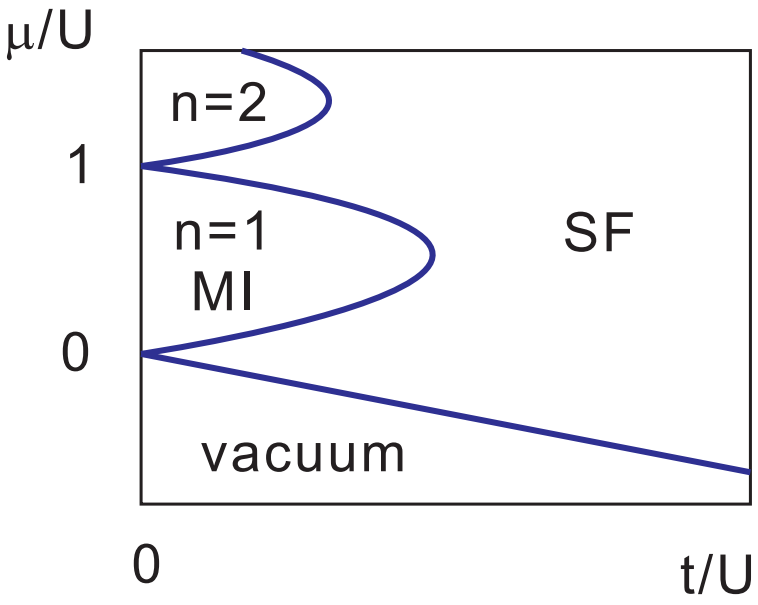

Figure 2.2: Zero temperature phase diagram of the Bose-Hubbard mode. The system goes through the quantum phase transition from an insulator phase to a superfluid phase by changing the tunneling strength or the chemical potential. The vacuum phase corresponds to the $n = 0$ Mott insulator phase.

which involve with a critical point at zero temperature. In the framework of the Bose-Hubbard model, the chemical potential controls number occupation in an individual lattice site. When the chemical potential μ smaller than zero, the system occupies the vacuum state ($n = 0$ Mott insulator). The system enters $n = 1$ or higher number occupation of insulator phase at a higher chemical potential. The system enters superfluid phase when the tunneling energy t overcomes the energy cost from the interaction energy U. Fig. 2.2 shows illustration of the zero temperature phase diagram of the Bose-Hubbard model.

CHAPTER 3

CONTROL OF ATOMIC QUANTUM GAS

We will be going through two techniques we use intensively for controlling the atoms, i.e. Feshbach resonance and optical lattices. Feshbach resonance allows tuning the atomic interaction strength with magnetic field. We start with the scattering theory by introducing the concept of partial wave expansion in the collision. We then focus on the s-wave contact interactions and calculate the s-wave scattering length.

Before discussing the optical lattice, we first explain the origin of optical dipole force. Optical dipole trap provides convenient trapping potential regardless of the magnetic moment of the atoms. With a well aligned gaussian beam, one can engineer the local trapping potential, including the trap depth and trap frequency. Through interfering two laser beams, the periodic optical potential formed from the interference fringe serves as an optical lattice. Atoms in the optical lattice resemble electrons in the ion crystal. One can write down the band structure which describes the low energy excitation spectrum of the atom. We will go through the physics of optical trapping and its application in ultracold atoms. We then calculate the band structure of atoms in the optical lattice. In the end of the chapter, we will discuss the way to engineer the band structure through modulation.

3.1 Feshbach resonance

Feshbach resonances [7] allow for the tuning of the scattering length a, by changing an external magnetic field. As was introduced in the previous section, the scattering length describes the collision between two atoms and can be derived from calculating the collisional phase shift. The strength of the phase shift can be estimated by calculating the coupling between different channels. In the simplest model, one can use an "entrance channel" (free atoms state) and a "closed channel" channel (molecular bound state) for this calculation. The phase shift depends on the coupling strength and the energy difference between two

channels. Typically, the spin configurations at the two channels are different. Therefore one can change the relative energy of the channels by a magnetic field. The dependence of the scattering length on the external magnetic field can be written as

$$a(B) = a_{bg}\left(1 - \frac{\Delta B}{B - B_0}\right), \tag{3.1}$$

where a_{bg} is the background scattering length, ΔB is the width of the resonance, and B_0 is the resonance position. An microscopic analytical model of the functional form of the Feshbach resonance can be found in Ref. [67].

3.1.1 s-wave interactions

For two atoms interacting with each other through collisions, the two-body collision between atoms can be decomposed to partial waves. Different partial wave components of the scattering potential $V_{\text{eff}}(R)$ can be written as

$$V_{\text{eff}}(R) = V(R) + \frac{\hbar^2 l(l+1)}{2MR^2}, \tag{3.2}$$

where $V(R)$ is the radial potential given by the van der Waals attractive interaction and the short range repulsive force, M is the reduced mass, l is the orbital quantum number. One can calculate the equilibrium radial distance and the corresponding repulsive potential barrier. For caesium atoms, the barriers are 37 μK, 191 μK, and 540 μK for $l = 1, 2, 3$ (p, d, and f-wave components) [65]. In the temperature regime of the ultracold atomic gas (< 60 nK), we only need to consider the s-wave contact interaction.

3.1.2 s-wave scattering length

Due to the centrifugal barrier, atoms don't collide with a higher partial wave. Interactions between dilute ultracold alkaline atomic gases can be modeled with an s-wave interaction,

and the interaction strength is described by the s-wave scattering length a. We review the scattering theory [65, 66] for better understanding the atomic collision.

Consider a wavefunction $\psi_0(x) = \frac{e^{i\mathbf{k}\cdot\mathbf{x}}}{(2\pi)^{3/2}}$ propagating in the space. After colliding with a fixed local potential $V(x')$, the far-field (r large) asymptotic result can be written as

$$\psi(x) = \frac{1}{(2\pi)^{3/2}}\left[e^{i\mathbf{k}\cdot\mathbf{x}} + f(\mathbf{k}', \mathbf{k})\frac{e^{ik'r}}{r}\right], \tag{3.3}$$

where $\mathbf{k}' = k'\frac{\mathbf{x}}{|x|}$, $r = |\mathbf{x}|$ and f is given by

$$f(\mathbf{k}', \mathbf{k}) = -\frac{2m}{4\pi\hbar^2}(2\pi)^3 \int d^3x' \frac{e^{-i\mathbf{k}'\cdot\mathbf{x}'}}{(2\pi)^{3/2}} V(x')\langle\mathbf{x}'|\psi\rangle. \tag{3.4}$$

From f, we can calculate the scattering cross-section and its angular dependence:

$$\frac{d\sigma}{d\Omega} = |f(\mathbf{k}', \mathbf{k})|^2, \tag{3.5}$$

which describes the scattering probability per unit solid angle Ω at an angle given by $\mathbf{k}'$ and $\mathbf{k}$.

The measurement of the scattering cross section has been an important tool in the physics community. In high energy physics community, scattering experiments give us information about particle sizes, and interaction strength. In condensed matter systems, X-ray scattering and neutron scattering off materials reveals the crystal structure of a bulk material.

To calculate the scattering cross section more quantitatively, we introduce the concept of scattering phase shifts. We start with a partial wave expansion of the incident plane wave:

$$\frac{e^{i\mathbf{k}\cdot\mathbf{x}}}{(2\pi)^{3/2}} = 4\pi\frac{1}{(2\pi)^{3/2}}\sum_{lm} i^l Y_{lm}(\hat{\mathbf{k}})Y_{lm}(\hat{\mathbf{k}'})j_l(kr), \tag{3.6}$$

where $Y_{lm}(\hat{\mathbf{k}})$ are the spherical harmonics, and $j_l(\rho)$ is the spherical Bessel function of order

l, which has the following asymptotic form:

$$j_l(\rho) = \frac{1}{\rho}\cos\left[\rho - \frac{(l+1)\pi}{2}\right]. \tag{3.7}$$

In the far-field, the wavefunction can be approximated as the following:

$$\psi(\mathbf{r}) = 4\pi\frac{1}{(2\pi)^{3/2}}\frac{1}{2ik}\sum_{lm} Y_{lm}(\hat{\mathbf{k}})Y_{lm}(\hat{\mathbf{k}'})\left[-\frac{e^{-i(kr-l\pi)}}{r} + [1 - T_l(k)]\frac{e^{ikr}}{r}\right], \tag{3.8}$$

where $T_l(k)$ is the transition matrix, and it describes the angular dependence of the scattering amplitude:

$$f(\mathbf{k}, \mathbf{k'}) = -\frac{4\pi}{2ik}\sum_{lm} Y_{lm}(\hat{\mathbf{k}})Y_{lm}(\hat{\mathbf{k}'})T_l(k). \tag{3.9}$$

We now arrive at the conclusion that a scattering event shifts the asymptotic phase of the propagating wavefunction.

Given the constraint of particle number conservation, the amplitude of $S_l = 1 - T_l(k)$ must equal one, where S_l is the S-matrix. With a conventional definition of $S_l = e^{2i\delta_l}$, the wavefunction can be simplified to

$$\psi(r) \approx \frac{\cos(kr + \delta_l - l\pi/2)}{kr}, \tag{3.10}$$

where δ_l is the scattering phase shift. We further rewrite the elastic collisional cross-section as

$$\sigma_{el} = \int d\Omega |f(\mathbf{k'}, \mathbf{k})|^2 = \frac{4\pi}{k^2}\sum_l (2l+1)\sin^2\delta_l. \tag{3.11}$$

Finally, we calculate the s-wave scattering length from the collisional phase shift. Writing the wavefunction in the form of $u(r) = r\psi(r)$, the Schrödinger equation can be expressed as

$$\frac{d^2u(r)}{dr^2} + k^2u(r) = 0. \tag{3.12}$$

In the limit of $k \approx 0$, the approximation solution is

$$u(r) = 1 - \frac{r}{a}, \tag{3.13}$$

where a is the s-wave scattering length. Combining Eq.3.10 and Eq.3.13, we get

$$\frac{1}{u(r)}\frac{du(r)}{dr} = k\cot(kr + \delta_0) = \frac{1}{r-a}. \tag{3.14}$$

When projecting the to the limit of $r = 0$, the expression for the scattering length can be solved from

$$k\cot\delta_0 = -\frac{1}{a}. \tag{3.15}$$

When $\delta_0 = \pi/2$, the scattering length diverges, and the system reaches unitarity. With the knowledge of a, one can write down the interaction energy based on the scattering length as the following:

$$U(r) = \frac{4\pi\hbar^2 a}{m}\delta(r), \tag{3.16}$$

where δ is the delta function. A positive a gives repulsive interaction, and a negative a gives attractive interaction.

3.2 Optical dipole potential

The oscillating electric field of the laser light induces dipole moment d of the atoms, and the dipole energy shifts the ground state level. To calculate the trapping force, we assume a two-level atom which has the ground state $|g\rangle$ and the excited state $|e\rangle$ separated by an energy difference of $\hbar\omega_0$, where $2\pi\hbar$ is the Planck constant and ω_0 is the transition frequency. The two levels can be coupled with a coherent electromagnetic radiation $E(r,t) = E_0\hat{\epsilon}\cos(\omega t)$ with a coupling strength W:

$$W = \langle e| - d\cdot E(t)|g\rangle = \frac{\hbar\Omega}{2}(e^{i\omega t} + e^{-i\omega t}), \tag{3.17}$$

where $\Omega = -\frac{eE_0}{\hbar}\langle e|r\cdot\tilde{\epsilon}|g\rangle$ is the Rabi frequency.

In the rotating wave approximation, the Hamiltonian can be written in a time-independent form:

$$\hat{H} = \frac{\hbar}{2}\begin{bmatrix} -\delta & \Omega \\ \Omega^* & \delta \end{bmatrix}, \tag{3.18}$$

where $\delta = \omega - \omega_0$ is the detuning of the light field.

By diagonalizing the Hamiltonian, one gets a new set of eigenvalues:

$$E = \pm\frac{\hbar}{2}\sqrt{\delta^2 + \Omega^2}. \tag{3.19}$$

With $|\delta| \gg \Omega$, one finds

$$\Delta E_g = -\frac{\hbar\Omega^2}{4\delta}. \tag{3.20}$$

In an atomic system, the strength of induced dipole depends on the transition frequency and the linewidth. The Rabi frequency can be written as

$$\Omega^2 = \frac{I}{2I_{sat}}\Gamma^2, \tag{3.21}$$

where Γ is the linewidth of the transition, I is the laser intensity and I_{sat} is the saturation intensity of the transition:

$$I_{sat} = \frac{\hbar\omega_0^3}{12\pi c^2}\Gamma. \tag{3.22}$$

The time-averaged potential is proportional to the laser intensity $V(r) = \frac{3\pi c^2}{2\omega_0^3}\frac{\Gamma}{\delta}I(r)$. A red-detuned laser beam gives negative optical potential which attracts atoms.

The gaussian beam profile of the trapping laser leads to a spatial variation of the trapping potential. For a condensate, the potential variation can be absorbed in the definition of local chemical potential as an offset as was discussed in the earlier chapter. In the framework of local density approximation, one can then extract thermodynamic quantities from the in situ image of the gas. In a thermally equilibrated sample, one can determine the equation

of state $\mu(n)$ as well as the pressure $P = \int n d\mu$.

In an advanced application of optical trapping, one can also apply the so-called dimple trick to create BEC at a higher temperature. Through applying a narrower and tighter trap in the center of the gas, the local atomic density can be enhanced in that region. The gas in the outer region of the dimple trap serves as a thermal reservoir and keeps the temperature as a constant. The overall result is the enhancement of the phase space density in the dimple trap.

Through focusing the laser beam in a tiny region, one can use the optical potential as an obstacle and perturb the system locally. Desbuquois *et al.* use a moving optical potential to stir a condensate and measure the critical velocity [76]. With a stirring velocity higher than the critical velocity of the superfluid, the system would be heated. One can use this method to determine the critical density of superfluid transition then.

Optical potential also allows creating versatile confinement geometry. Originated in the electronic system, it's found that the conductance of electrons through a constriction is quantized. Number of available conduction channel depends on the chemical potential, and it increases in a quantized way. This is the well known as quantum point contact. Esslinger group use an optical potential to create a tiny constriction in a Fermi gas [14, 15], and the atomic system shows resemblance of quantum point contact in an electronic system.

To create a homogeneous sample, one can load BEC in a three-dimensional uniform potential. With an optical box potential formed with blue-detuned laser beams, Gaunt *et al.* demonstrated quasiuniform BEC in free space. The density of state has subtle difference in a free space and in a harmonic trap, and the critical point of the phase transition can be altered.

3.3 Optical lattice

An one-dimensional optical lattice can be created by interfering two laser beams. Bose-Hubbard model (BHM) describes the many-body Hamiltonian of ultracold atoms with finite

kinetic energy and interaction energy:

$$H = -J \sum_{<i,j>} \hat{a}_i^\dagger \hat{a}_j + \sum_i \epsilon_i \hat{n}_i + \frac{1}{2} U \sum_i \hat{n}_i(\hat{n}_i - 1). \tag{3.23}$$

BHM anticipates the phase diagram composed of the superfluid phase and the Mott insulator phase. Distinct differences between the two phases exist in many ways. The suppressed number statistics in the insulator phase is related to its incompressible nature. The loss of coherence in the insulator phase also has been studied extensively.

With interference between multiple lasers, novel band structures in complicated lattices were also demonstrated. Rich physics can be studied based on sophisticated phase locking technique between different lasers. Examples include like frustrated XY model in the triangular lattice, band structures in a kagome lattice [73, 74], and artificial gauge field in superlattices.

Moreover, optical lattices can be used as a tool to study low dimensional physics. For atoms loaded in an extremely deep lattice, one can ignore the physical degree of freedom of the wavefunction in that dimension. When the temperature and chemical potential is much smaller than the spacing of the harmonic quantum level, the wavefunction can be considered to be frozen in the ground state. An one-dimensional system can be created by applying two orthogonal deep lattices on atoms. As was shown by Girardeau [49], the wavefunction of hard-core bosons have diminished overlapping in a 1D strongly interacting system. The bosonic wavefunction then has resemblance of the fermionic behavior. The modification on the quantum statistics causes enhanced phase fluctuation at zero temperature. The phase fluctuation prohibits condensation of the classical gas in the low atom number limit. One needs to have more particles in order to recover the expected Thomas-Fermi profile given by the Gross-Pitaevskii equation.

Another novel phenomenon in an one-dimensional system is the realization of matter wave bright soliton. With the introduction of nonlinear attractive interaction between particle,

matter wave can propagate without dispersion. The competition between attraction and the quantum pressure supports the existence of soliton. The attraction overcomes the quantum pressure and leads to severe particle loss in a higher dimension.

3.3.1 Band structure

The wavefunction $\phi(x)$ of the condensate in the weak periodic potential $V(x) = U_0 \sin^2(kx)$ satisfies the Schrödinger equation:

$$-\frac{\hbar^2}{2m}\frac{d^2}{dx^2}\psi(x) + V(x)\psi(x) = E\psi(x). \tag{3.24}$$

Given the periodicity, Bloch theorem [75] states that the wavefunction can be written as $\psi(x) = \phi_q^n(x) = e^{iqx}u_q^n(x)$, where q is the quasi-momentum and is limited in the range of $[-\pi/d, \pi/d]$, n is the quantum number, and $u_q^n(x) = u_q^n(x+d)$ describe the periodic wavefunction. The Schrödinger equation can be rewritten in the following form:

$$-\frac{\hbar^2}{2m}\nabla^2\phi_q^n(x) + U_0 \sin^2(kx)\phi_q^n(x) = E_q^n\phi_q^n(x). \tag{3.25}$$

The wavefunction now shows resemblance of Mathieu's differential equation $d^2y/dx^2 + (a - 2s\cos 2x)y = 0$ as

$$\frac{\partial^2 y}{\partial x^2} + \left(\frac{E_q^n}{E_R} - \frac{U_0}{2E_R} + \frac{U_0}{2E_R}\cos(2x)\right) = 0, \tag{3.26}$$

where $E_R = \hbar^2k^2/2m$ is the recoil energy. At a given lattice depth $s = -U_0/4E_R$, the band structure $E_q^n = a - 2s$ can be found by finding a certain characteristic value a to satisfy the equation. The solution of the wavefunction can be described with modified Mathieu functions of the first kind which have a closed form representation and are constructed with Bessel functions.

In the tight binding model, one can then calculate the Wannier function which is a new set of complete basis and describes the most available localized wavefunction given by an

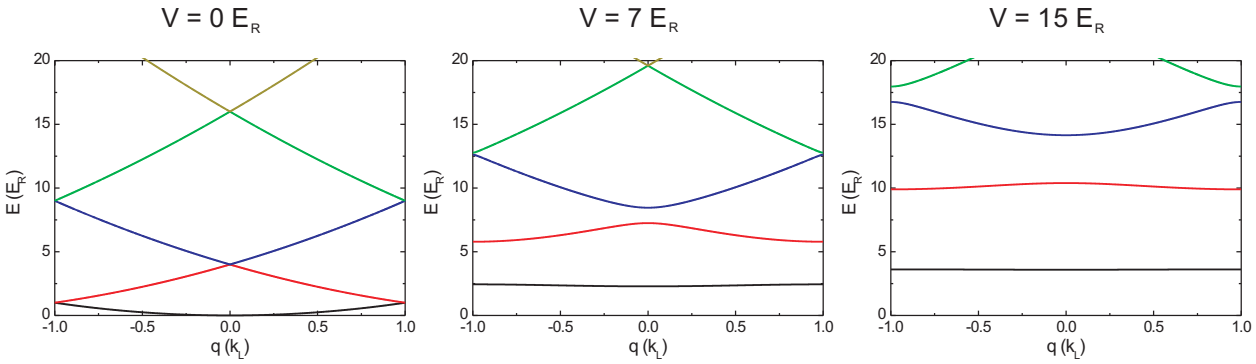

Figure 3.1: Band structures in a one dimensional optical lattice with different lattice depths.

individual band:

$$\omega_n(x - x_i) = \frac{1}{L}\sum_q e^{-iqx_i}\phi_q^n(x) = \frac{1}{L}\sum_q e^{-iq(x-x_i)}u_q^n(x). \tag{3.27}$$

Wannier wavefunction provides convenient way to calculate tunneling energy and on-site interaction in the Bose-Hubbard model:

$$t = \int dx\omega_0(x+d)\hat{H}_0\omega(x); \tag{3.28}$$

$$U = g\int dx|\omega_0(x)|^4, \tag{3.29}$$

where $\hat{H}_0 = \frac{\hbar^2\hat{p}^2}{2m} + V(x)$ and $g = \frac{4\pi\hbar^2 a}{m}$ is the interaction strength. The band structure can be related to the tunneling energy t in the following way:

$$E_q = -2t\cos qd, \tag{3.30}$$

thus the tunneling energy is equivalent to a quarter of the band width.

A suppressed tunneling energy in a lattice is the reflection of reduced kinetic energy or an enhanced atomic effective mass m^*. The lattice potential in the Schrödinger equation can be absorbed in the redefined atomic mass and interaction strength, and one can estimate

the effective mass through calculating the ground band curvature:

$$\frac{1}{m^*} = \frac{1}{\hbar^2}\frac{d^2}{dq^2}E_q^0. \tag{3.31}$$

The enhanced local density can also be absorbed in the effective interaction strength.

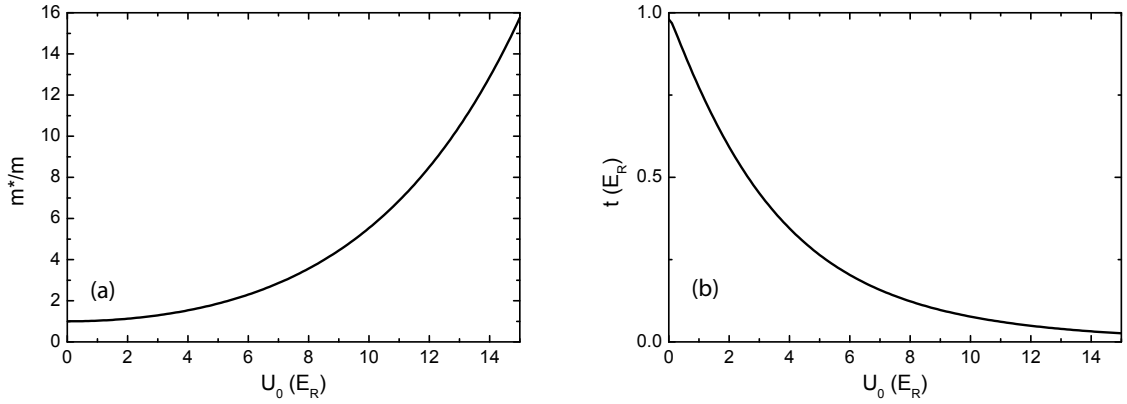

Figure 3.2: Dependence of effective mass m^* and tunneling energy t on the lattice depth.

3.3.2 Projecting the wavefunction in the free space

Time-of-Flight (TOF) is an important technique to measure the atomic temperature and coherence for ultracold atomic physics. Releasing atoms from the trapping potential converts the original wavefunction back to the free space basis.

For atoms in the optical lattice, one can then decompose the Bloch states ϕ_q^n to discrete plane-wave basis $|\phi_p\rangle$:

$$\phi_q^n = \sum_{m=-\infty}^{\infty} a_{n,q}(m)|\phi_{q+2m\hbar k}\rangle. \tag{3.32}$$

The coefficient $a_{n,q}(m)$ depends on the lattice depth. After TOF, one gets replicas of clouds with a well-defined momentum difference.

3.4 Modulating the lattice

Lattice modulation provides a high degree of freedom to engineer the single particle dispersion of atoms in the optical lattice. First discovered by Gemelke *et al.* that the parametric amplification of matter wave can happen through engineering the band structure with modulation [55]. Later, Lignier *et al.* demonstrated engineering of the tunneling coefficient between lattice sites can even lead to a negative tunneling coefficient [56]. In the band structure perspective, a negative tunneling coefficient corresponds to a negative effective mass. Below, we will introduce the math we used to calculate the band structure in a driven system [77]. An important feature in our lattice modulation technique is to use a near detuned modulation frequency with respect to the frequency defined by the band gap. In this configuration, a significant modification on the band structure can happen even by applying a modulation amplitude which is much smaller than the lattice constant. This gives us a minimum heating rate and a long sample lifetime. In the end of the section, we also provide experimental measurement on the loss coefficient with different modulation configurations in our system.

3.4.1 Band hybridization

Similar to the dipole coupling between two electronic states with a coherent laser light, one can also couple two energy bands in the optical lattice by phase modulating the lattice potential. The modulation coupling W can be modeled as

$$W(t) = W_0 \cos(\omega t) = \langle e|\hat{W}(t)|g\rangle = \langle e|F(t)\hat{x}|g\rangle, \tag{3.33}$$

where $F(t) = F_0 \cos\omega t$ corresponds to the dipole force from the displaced lattice potential. With a given maximum displacement of x_0 and $x_0 \ll d$ where d is the lattice constant, we have $F_0 = 2U_0 k^2 x_0$ where U is the lattice depth. For deep enough lattice $\langle e|\hat{x}|g\rangle = l/\sqrt{2}$, where $l = (\hbar/m\omega_0)^{1/2}$ is the harmonic oscillator length, and ω_0 is the trap frequency in the

individual lattice site.

Applying this coupling in the energy bands in the optical lattice and using the rotating wave approximation, one can write down the Hamiltonian as

$$\hat{H}_{RWA} = \begin{bmatrix} E_e(q) - \hbar\omega & W_0/2 \\ W_0/2 & E_g(q) \end{bmatrix}, \tag{3.34}$$

and the eigenenergies can be written as

$$E_\pm = E \pm \frac{\sqrt{\hbar^2\delta^2 + W_0^2}}{2}, \tag{3.35}$$

where $E = (E_e + E_g - \hbar\omega)/2$, and $\delta = \hbar\omega - \Delta E$ is the detuning from the band gap $\Delta E = E_e - E_g$. With a detuning much smaller than the width of the bands, one can locally engineer the coupling at a certain q.

3.4.2 Floquet model

The single-particle physics of an atom with mass m in a (1D) time-dependent optical lattice formed by retro-reflected light of wavelength λ_L is governed by the Hamiltonian:

$$H(t) = -\frac{\hbar^2}{2m}\frac{\partial^2}{\partial x^2} + U_0 \sin^2 \frac{2\pi}{\lambda_L}[x - x_0(t)], \tag{3.36}$$

where $\lambda_L/2$ is the lattice constant, U_0 is the lattice depth, and $x_0(t)$ is the time-dependent lattice offset. For periodic lattice offsets $x_0(t+\tau) = x_0(t)$, the Hamiltonian is characterized by temporally and spatially periodic Floquet states. In analogy with spatially periodic Bloch states, which define momentum only up to an overall lattice momentum, the Floquet states define energy only up to an overall energy $E = h/\tau$, corresponding to the absorption or emission of one quantum of energy at the shaking frequency.

We first compute the time average band structure by diagonalizing the time-averaged

potential $H_0(k) = \langle H(k,t)\rangle$ for each momentum and express the time-dependent Hamiltonian as $H(k,t) = H_0(k) + H'(k,t)$. We then break this Hamiltonian into 100 discrete time steps and compute the Trotter product of the time evolution operator (with $\hbar = 1$):

$$U(k,\tau) = \int_0^\tau dt e^{iH(k,t)} \approx \prod_{n=0}^{N} \left(e^{i\Delta t H_0(k)}\right)\left(1 + i\Delta t H'(k, n\Delta t)\right). \tag{3.37}$$

Finally we numerically diagonalize $U(k,t)$ to obtain the eigenstates and energies (up a factor τ).

Fig. 3.3 shows the dispersion of the lowest Floquet band for several shaking amplitudes, and barrier height between the minima of the dispersion. In general, the Floquet bands $|k,t\rangle_n$ will be periodic time-dependent superpositions of many of the unshaken bands $|k\rangle_n^0$ (i.e. the bands obtained with no shaking). However, in our case the band spacing is sufficiently anharmonic that only the lowest two bands are near-resonant for k near k^*, and modulation is sufficiently weak that higher order terms are negligible. To obtain numerical dispersions for this Hamiltonian, we consider only the lowest 21 momentum states around the desired momentum k, that is, $k-20k_L, k-18k_L, \ldots, k, \ldots, k+18k_L, k+20k_L$, with $k_L = 2\pi/\lambda_L$. This is more than enough states to describe the lowest band, and similar results are obtained using fewer states.

Therefore, the lowest band $\phi_q^{0*}(t)$ is effectively a superposition of the lowest bare states ϕ_q^0 and ϕ_q^1, that is, $\phi_q^{0*}(t) = \alpha(t)\phi_q^0 + \beta(t)\phi_q^1$, where $\alpha(t)$ and $\beta(t)$ are time-dependent amplitudes. Under our conditions with $U_0 = 7E_R$, $d = 532$ nm and $\Delta x = 65$ nm, $|\alpha| \approx 0.95$, and $|\beta| \approx 0.25$. The relative phase evolves by 2π over the course of a shaking cycle.

3.4.3 Heating in the shaken optical lattice

Heating and atomic loss in a shaken optical lattice could be problematic for realizing a Floquet ground state. We get around this problem by using a shallow optical lattice where the lattice potential is anharmonic enough to avoid continuous resonant excitation. With

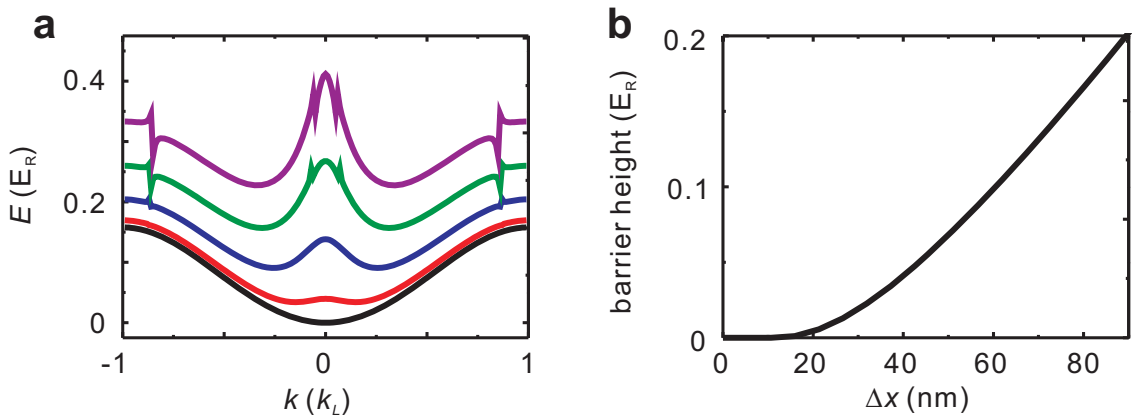

Figure 3.3: **a** Calculated dispersion of the lowest Floquet band with different amounts of shaking (listed as peak-to-peak, from bottom to top): no shaking, 21 nm, 43 nm, 64 nm, and 85 nm. The lattice depth is 7 E_R, and the lattice constant is $d = 532$ nm. The sharp features correspond to weak coupling with bands above the lowest two. **b** Height of the barrier between the two wells as a function of the shaking amplitude.

near resonant shaking, we can also reduce the shaking amplitude as well as the heating. In this section, we characterize BEC number loss for gases in a shaken optical lattice. We will discuss the loss dependence on the dimensionality of the gas and number of lattices. We perform measurements on the number loss of a BEC loaded in a shaken optical lattice. We calculate the functional form of the decay rate and extract the scaling of the loss coefficient with respect to the modulation amplitude and the scattering length experimentally.

In a two-dimensional (2D) gas system, we write down the master equation of the decay process in the following form:

$$\frac{dN}{dt} = -\alpha \int n_{3D}^2 dr = -\frac{\alpha}{\sqrt{2\pi} l_z} \int n_{2D}^2 dr = -\frac{\alpha}{\sqrt{2\pi} l_z} F, \tag{3.38}$$

where N is the BEC number, α is the loss coefficient, $l_z = 200$ nm is the oscillator length, and n_{2D} (n_{3D}) is the 2D (3D) density. With the knowledge of the trapping potential $V(r) = \frac{1}{2} m\omega^2 (x^2 + y^2)$, the function F can be defined in the following form based on Thomas-

Fermi approximation:

$$F = \frac{1}{g_{2D}^2}\int [\mu - V(r)]^2 dxdy \sim \frac{\mu^2}{g_{2D}^2}\frac{\mu}{m\omega^2}, \tag{3.39}$$

where $g_{2D} = \frac{\sqrt{8\pi}\hbar^2 a}{m l_z}$ is the interaction strength in two dimensions, a is the scattering length, μ is the chemical potential, ω is the geometric mean of the trap frequency. The scaling of the particle number to the chemical potential can also be written down explicitly:

$$N = \frac{1}{g}\int [\mu - V(r)] dxdy \sim \frac{\mu}{g_{2D}}\frac{\mu}{m\omega^2}. \tag{3.40}$$

We can then rewrite the master equation as the following:

$$\frac{dN}{dt} = -\alpha c_{2D}\frac{1}{\sqrt{2\pi} l_z}\sqrt{\frac{m\omega^2}{g_{2D}}} N^{3/2}. \tag{3.41}$$

Similar calculation can also be done in a three-dimensional (3D) system, and the result is summarized in the following:

$$\frac{dN}{dt} = -\alpha c_{3D}\left(\frac{m\omega^2}{g_{3D}}\right)^{3/5} N^{7/5}, \tag{3.42}$$

where $g_{3D} = \frac{4\pi\hbar^2 a}{m}$ is the interaction strength in three dimensions, and the numerical constant c_{2D} (c_{3D}) is 0.67 (0.57). We fit the BEC number loss with Eq. 3.41 and Eq. 3.42 and extract the loss coefficients; see Fig. 3.4.

From the measurements, we observe that the scaling of the loss coefficient with respect to the shaking amplitude Δx approaches linear fashion at large Δx. This agrees with the theoretical prediction [82, 83]. The loss rate of a 3D gas caused by 2D shaking is approximately 4 times larger than that caused by 1D shaking, and the loss rate of a 2D gas caused by 2D shaking is comparable to that of a 3D gas. Furthermore, the scaling of the loss rate to the total particle number is different between a 2D gas and a 3D gas. Although the difference

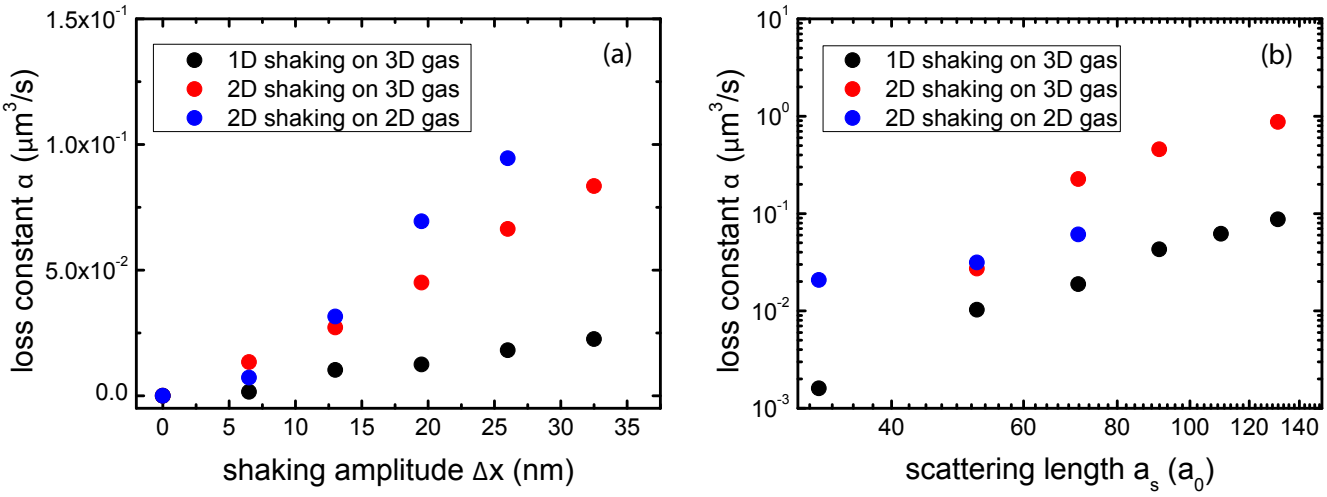

Figure 3.4: (a) Loss coefficient versus the shaking amplitude. The scattering length being used is 52 a_0. (b) Loss coefficient versus the scattering length. The shaking amplitude being used is 13 nm. Note that the loss coefficients are extracted based on the mean atomic density averaged over a unit cell. The definitions of unit cell between 1D shaking and 2D shaking experiments are different since the number of optical lattices being used is different.

is small, effect would be enormous considering the typical particle number of $15,000$. This makes the apparent lifetime of a 2D condensate even shorter.

Realizing a stable quantum gas in a shaken optical lattice allows investigation of new physical phenomena. With 1D shaking, we will introduce the creation of effective ferromagnetism, observation of stable ferromagnetic domain, and observation of roton excitation spectrum in the following chapters. There are also proposals for creating 2D spin-orbit coupling or multi-color ferromagnetism based on the 2D shaking scheme. We are looking forward to seeing all the applications based on this experimental method.

CHAPTER 4

PREPARING, PROBING AND MANIPULATING A CESIUM BEC

A machine with produces Bose-Einstein condensates can now be constructed based on a standard recipe and be ready to produce new scientific discoveries. Nevertheless, it is never trivial to setup a machine to perform a specific set of experiments, and it requires attention on the ultrahigh vacuum, electronic control, and stable lasers. A brief introduction on the system will be provided in this chapter, and a detailed description of this Cs quantum gas machine can be found in the theses of Chen-Lung Hung and Xibo Zhang.

In the later part of the chapter, we discuss implementation of tools for better characterizing our system and controlling the atoms. Three perspectives will be introduced, including characterization of the imaging system, lattice modulation, and engineering the trapping potential. For imaging, we develop the model to characterize the imaging imperfection of the system. This is helpful for upgrading and optimizing the imaging system. For the lattice, we use a pair of acousto-optical modulators (AOMs) to create an optical lattice. Through frequency modulating the driving RF signal to the AOMs, we phase modulate the lattice potential. We will discuss the calibration of the lattice depth and the modulation amplitude. For the trapping potential, we use a digital micromirror array device and a far off-resonant laser to create an arbitrary optical potential. This can be used to compensate the trap inhomogeneity from the dipole trap. With its capability of dynamic control, we perform projection Bragg spectroscopy.

4.1 Cesium atoms

We use cesium-133 atoms to create our Bose-Einstein condensate, and the condensate is prepared at $|3, 3\rangle$ the hyperfine ground state. The advantage of using Cs atoms comes from the convenient control of the atomic scattering length. The elastic scattering can be described

by s-wave scattering and be controlled with the magnetic Feshbach resonance [7]. From 17.1 G to 20 G, we can tune the scattering length from 0 a_0 to 200 a_0 with high precision. A precise model and measurement gives good estimation on the scattering length, see Fig.4.1.

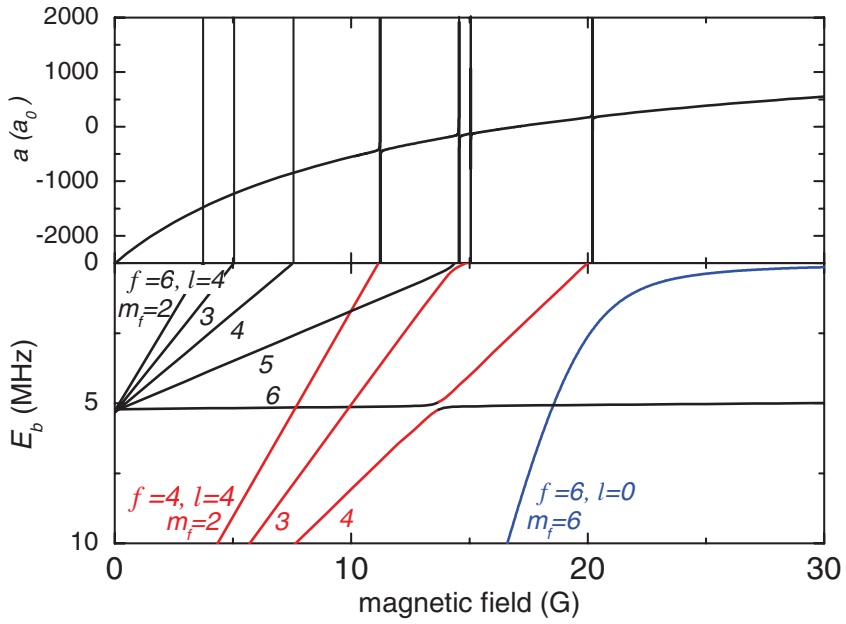

Figure 4.1: Dependence of Cs $|3,3\rangle$ state scattering length and the bound state energy on the magnetic field. Figure reprinted from Ref. [7].

In addition to elastic scattering, Cs also has inelastic scattering which leads to heating and loss. When three atoms collide, two of them can form bound state, and the released energy is converted to the kinetic energy and leads to particle loss from the trap. The loss rate can be modeled in the following equation:

$$\dot{n} = L_3 n^3, \tag{4.1}$$

where L_3 is the loss coefficient and n is the atomic density. The loss coefficient L_3 scales with the scattering length to the fourth power $L_3 = 3C\hbar a^4/m$, where C describes the deviation from the a^4 dependence. Efimov physics contributes to most of the deviation. As was shown in Fig.4.2, a significant enhancement of loss at -850 a_0 which comes from the coupling of three

free atoms to an Efimov trimer. On the positive side, there is a recombination loss minimum at 210 a_0 caused by a destructive interference of decay pathways. This loss minimum is useful for us to keep the atomic cloud stable.

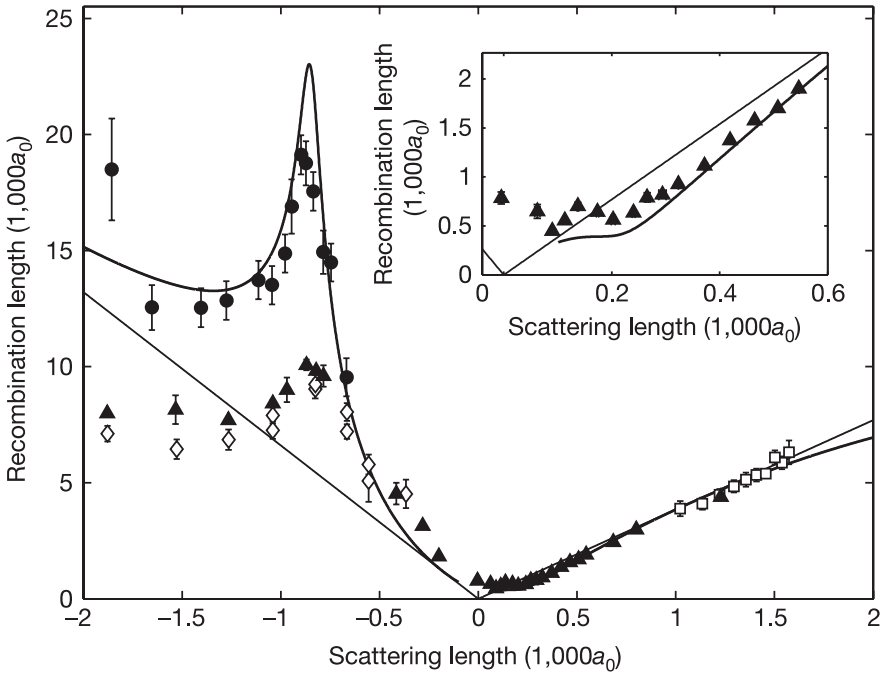

Figure 4.2: Three-body recombination strength of Cs $|3,3\rangle$ state. The recombination strength has a^4 trend with enhanced loss at ~ -850 a_0 due to the Efimov physics. Figure reprinted from Ref. [24].

For laser cooling, we rely on the electronic transitions. The electronic ground state $6^2S_{1/2}$ has two hyperfine state $F = 3, 4$, and the energy difference is 9.19 GHz. The hyperfine splitting is used as frequency standard in an atomic clock. The first electronic transitions are $6^2S_{1/2}$ to $6^2P_{3/2}$ (D2) and $6^2S_{1/2}$ to $6^2P_{1/2}$ (D1), and the corresponding wavelengths are 852 nm and 890 nm. D2 transition is preferred to be used in the laser cooling because of its larger scattering rate. We use the cycling transition $F = 4$ to $F' = 5$ in the magneto-optical trap and absorption imaging. In the scattering process, some atoms fall to the $F = 3$ state. To drive atoms falling into the $F = 3$ state, we use $F = 3$ to $F' = 4$ transition for repumping.

4.2 Hardware

We will go through the concept of the design in the following sections.

4.2.1 Vacuum system

Our vacuum system is composed of a Cs oven, a Zeeman slower, and a science chamber, see Fig.4.3. The Cs oven contains cesium metal and is heated to 60 °C in order to give enough vapor pressure and atomic flux. In between the oven and the Zeeman slower, we have a cold finger to collect atoms with the unwanted directionality. The cold finger is composed of a nipple cooled by a TE cooler. A water cooled thermal reservoir is used to remove the heat generated by the TE cooler. A pair of 1-mm-radius apertures before and after the nipple are used to select the directionality of the atomic beam.

Our vacuum is maintained by two ion pumps. One is connected to the intermediate chamber which bridges the Zeeman slower and the cold finger. It serves to remove atoms which desorb from the surface of the cold finger. The vacuum in the intermediate chamber is below 1×10^{-10} torr which is limited by the sensitivity of the detection. There is also an additional independent ion pump is used to maintain the vacuum of the science chamber. The science chamber pressure is maintained to be less than 3×10^{-12} torr.

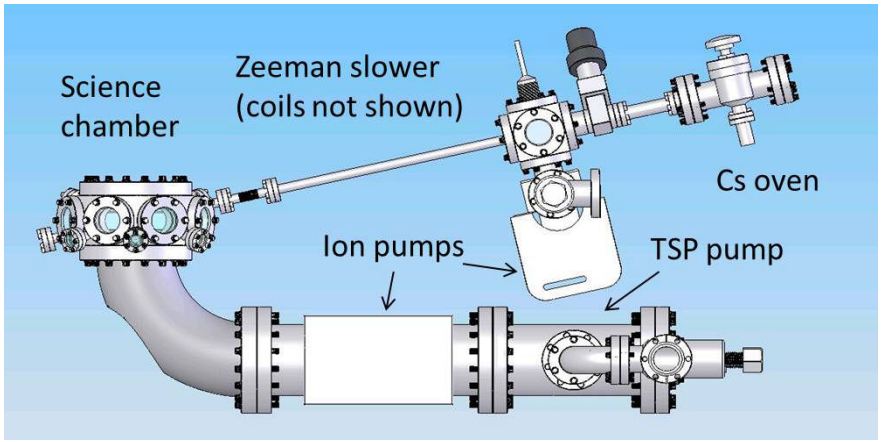

Figure 4.3: Design of the vacuum system.

During the course of 6 year operation, the ion pump connected to the intermediate

chamber is polluted. Cesium metal deposits between the two electrodes of the ion pump and causes electric shorting. The leakage current is larger than the limit of the controller output, and the controller fails. With the assistance of an external turbo pump, we tried baking the ion pump as well as burning the deposited cesium with a current source (hi-potting). These methods do not work as expected, and we decide to maintain the vacuum with an additional ion pump.

In several months, we find the additional ion pump fails due to the possible migration of cesium to the new pump. During the maintenance, we discover that the ion pump resume to work after an exposure to the atmosphere. The potential mechanism is that the cesium metal is oxidized by the air during the exposure.

The science chamber is designed to have a versatile optical access. The top and bottom 6-inch flanges are reserved for the high resolution imaging. The window is recessed into the chamber to give the maximum numerical aperture. Eight $2-3/4$ flanges are designed for dipole trap beams. Eight staggered $1-1/3$ flanges are used by Zeeman slower beam, Raman sideband cooling beams, and its optical pumping beam.

4.2.2 Diode lasers

Diode lasers are the main tools we use for cooling. We have five diode lasers including reference laser (REF) which provides absolute frequency standard based on spectroscopy, magneto-optical trap laser (MOT) which performs cooling by driving the atoms through cycling transition, repumper laser (REP) which recycles atoms falling into the unwanted hyperfine state, and sideband cooling lasers (dRSC master and dRSC slave). We use grating feedback for the first four lasers to achieve a narrow linewidth of about 300 kHz. The last one serves as an amplifier and is frequency stabilized by injecting with RSC master.

The REF laser is used as a frequency reference with the help of polarization spectroscopy which converts the frequency information to the rotation of laser polarization. We send a linearly polarized probe beam through a Cs vapor cell. A counter propagating circularly

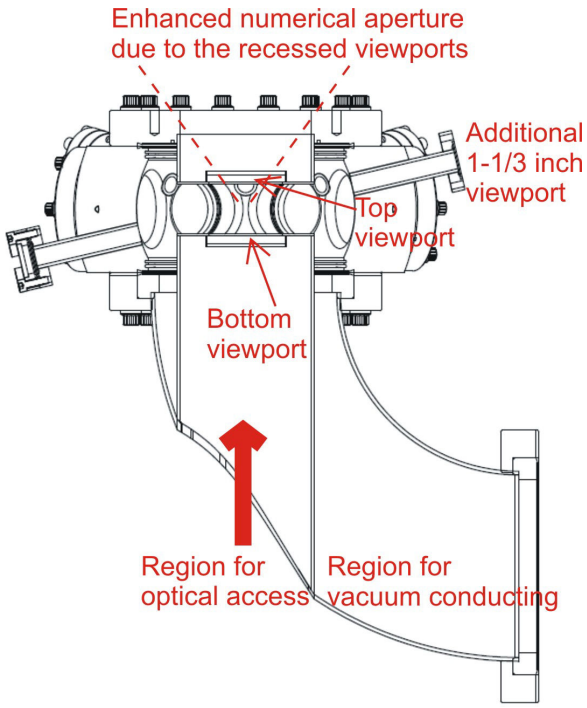

Figure 4.4: Optical access of the science chamber.

polarized pump beam breaks the symmetry of the probe beam polarizations. When the probe beam is frequency detuned from the resonance, it experiences circular birefringence. We use a polarization detector to measure the amount of birefringence. Our REF laser is locked to the cesium $4 \rightarrow 5'$ transition but frequency detuned by 320 MHz. The frequency offset is designed to accommodate the operation range of the MOT and REP feedback circuits.

MOT laser frequency is feedback controlled based on the beatnote signal with the REF laser on a fast photodiode (Hamamatsu S5873). The beatnote signal is frequency divided by 1020 (RF Bay, FPS-1020-4) and further by 4 (74HC393) down to 100 kHz range. We use a phase lock loop circuit (LM565) to convert the frequency signal into a DC voltage signal for the feedback. MOT laser's frequency is locked around $4 \rightarrow 5'$ transition. For REP laser, the beatnote signal is fist mixed with a 9.1 GHz local oscillator (Jersey Microwave, PLDRO-9100-1210) which is referenced to the 10 MHz rubidium clock (SRS, FS725). REP laser's frequency is locked around $3 \rightarrow 4'$ transition.

dRSC master is a free running laser without frequency stabilization. It's frequency is

set to be -20 GHz detuned from the $3 \rightarrow 4'$ transition. The drift is much smaller than the detuning and can be ignored.

In order to have a narrow laser linewidth, the output of the grating feedback laser is operated around 30 mW (5 mW for the dRSC master). dRSC slave is set to output 120 mW. Power broadening is not an issue since its linewidth is determined by the linewidth of the injection laser. The laser power would be enough for imaging (1 mW) and optical pumping (2 mW). However, it would not be enough for creating a magneto-optical trap (60 mW) and Zeeman cooling (20 mW). We amplify the laser power with a taper amplifier (Sacher TEC400). With an injection power of 20 mW MOT laser and 1 mW REP laser, we get an output of 240 mW with both frequency components.

All the diode lasers are fiber coupled to the optical table of the main chamber. By doing this, we can modularize the laser system. Maintenance of the laser system would not disturb the alignment in the main system.

4.2.3 Optical dipole trap

We use three 1064 nm Nd:YAG laser beams for optical trapping, including x-, y-dipole trap beams and a light sheet beam. The laser frequency is far detuned from the cesium transition line, so the heating caused by light scattering can be suppressed. In addition, commercial high power laser is available at this wavelength. The beam waist of the dipole trap beams is 300 μm, and the purpose is to provide weak confinement in the xy-plane. A pair of acousto-optical modulators (AOMs) are used to control the intensity of the retro-reflection. By turning on the RF signal feeding to the AOMs, we create an additional optical lattice on top of the dipole trap.

A light sheet beam enters the chamber with a 45° angle with respect to x-, y-dipole traps. Its purpose is to provide a strong optical force to hold the BEC against the gravity. In order to create a potential gradient which is strong enough, we focus the beam in the z-direction with a cylindrical lens. The beam size is 45 μm in the z-direction and 270 μm in the xy

plane. With contribution from all the dipole trap beams, we achieve trap frequencies of (10, 30, 60) Hz in x'-, y'-, z-directions.

For ground state cesium atoms, there are two main transitions to consider. The ground state light shift weighted by the line strengths of $D1$ and $D2$ line can be written in the following:

$$V(r) = \frac{3\pi c^2}{2}\left(\frac{1}{3}\frac{\Gamma_1}{\omega_1^3\Delta_1} + \frac{2}{3}\frac{\Gamma_2}{\omega_2^3\Delta_2}\right), \tag{4.2}$$

where $\Gamma_1 = 2\pi \times 4.56$ MHz and $\Gamma_2 = 2\pi \times 5.22$ MHz are the natural line widths of the D_1 and D_2 lines, $\omega_1 = 2\pi \times 335.1$ THz and $\omega_2 = 2\pi \times 351.7$ THz are their transition frequencies. With a laser wavelength of 1064 nm we use for the dipole trap, we have $\Delta_1 = -2\pi \times 53.34$ THz and $\Delta_2 = -2\pi \times 69.94$ THz. The corresponding polarizability is $\alpha = -k_B \times 2.35$ nK $\cdot$ cm^2/W.

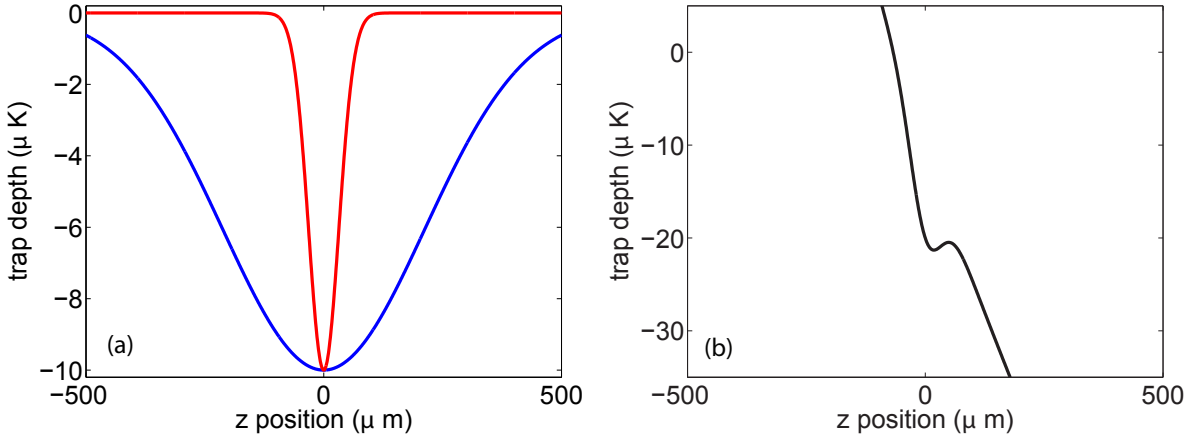

Figure 4.5: Calculation of trap depth with (right) and without (left) the magnetic field gradient. The red curve calculates the optical potential from the light sheet while the blue represents the contribution from the crossed dipole trap. Gravity is steep enough to almost open the trap.

With a typical laser power of 2 W, the crossed dipole trap has a trap depth of $V_0 = k_B \times 10$ μK. The 600 mW light sheet beam also gives a trap depth around 10 μK. Moreover, the steep potential gradient in the vertical direction given by the light sheet beam is strong enough to hold atoms against the gravity.

With a full magnetic levitation, the total trap depth from three beams is about 20 μK. Without the magnetic levitation, the trap depth is only 0.8 μK. We control the strength of

magnetic field gradient for evaporation.

There are two reasons for using the magnetic levitation to compensate the gravity. One is for trapping. Given the Cs mass, one can immediately calculate the dependence of the potential on the vertical position U_{grav} = 1568 μK $\cdot$ z/cm, where z is the vertical position. For a mm size cloud with a temperature of about 10 μK after MOT cooling, the potential difference across the cloud caused by the gravity would be 15 times larger than the the temperature which is considered to be the required energy scale for trapping. With magnetic levitation, the required laser intensity for the dipole trapping could be lowered significantly. In addition to trap, magnetic levitation can also keep the atom center-of-mass steady while letting the atoms free expand. With a 70-ms TOF duration, atoms falls by 2.4 cm which is far out of the imaging field-of-view or depths-of-focus. The magnetic dipole moment of Cs at $|3,3\rangle$ state is $\mu = \frac{-3}{4}\mu_B$. To hold the atoms against the gravity, one would need a magnetic field gradient of $\frac{\partial B}{\partial z} = \frac{4mg}{3mu_B}$ = 31.3G/cm, where m = 133 amu is the Cs atomic mass and g is the gravity.

4.2.4 Control system

We use a computer control system to automate the experimental sequences. With digital and analog outputs, we can turn on/off the shutter, trigger the CCD camera, change the laser frequency through tuning the laser current in a feedback circuit, tune the AOM RF frequency and power to change the laser intensity and frequency, and we also change the strength of magnetic field and magnetic gradient.

Four National Instrument PCI cards are implemented in the control computer, including one 32-channel digital output (PCI-6534), two 8-channel analog output (PCI-6713), and one 32-channel analog output (PCI-6723).

We generate a table of operation to the on-board FIFO memory. The output of all the analog boards would be synchronized by trigger signal from the digital board.

4.3 Laser cooling

We introduce the laser cooling sequences we use for preparing a degenerate quantum gas. Starting from Zeeman slowing and magneto-optical trap, we collect 40 million atoms at a Doppler-limit temperature of 40 μK. The molasses cooling allow further reducing the temperature to sub-Doppler-limit at 10 μK. We then perform degenerate Raman sideband cooling to cool atoms down to 2 μK. To reach a degenerate gas, one needs to use evaporation as the cooling method. We will introduce our evaporation sequence in the next section.

The limitation of creating a BEC with all optical cooling usually resides on the detrimental effect from the cooling laser when the atomic density is high. So the phase space density won't be able to exceed the critical value. Recently, laser cooling to degeneracy has been experimentally demonstrated by applying a transparency laser beam [79]. Through applying an additional laser beam to shift the transition frequency locally, the atom density in that local region can be free from the detrimental effect while keeping a low temperature.

4.3.1 Zeeman slowing

We use Zeeman slower to decelerate the velocity of Cs beam from the oven. The 40 cm long slower tube is composed of four sections. The magnetic field in the slower tube is designed to range from 100 G to 0 G. With an optimized slower laser detuning of -93 MHz, we collect atoms with a velocity ranging from 50 to 205 m/s. The maximum number of scattered photons can be more than 50 000. The atomic flux saturates at a laser power around 25 mW.

4.3.2 Magneto-optical trap and optical molasses

We use a magneto-optical trap (MOT) to collect atoms which have been Zeeman slowed. The laser we use is derived from a single fiber output with a total power of 60 mW. The laser frequency is tuned to the $4 \rightarrow 5'$ transition with a weak component of $3 \rightarrow 4'$ transition

as the repumper. The laser is split into three beams which enter the science chamber in the x-, y-, and z-directions and are retro-reflected.

At an oven temperature of 60 °C, we get an atomic flux of 2×10^8 atoms/s. With a laser detuning of -14 MHz and a magnetic field gradient of B' = 15 G/cm, the atom number saturates at 4×10^7 in 2 s. The temperature of the cloud is around 40 μK.

After the MOT loading stage, we turn off the Zeeman slower laser and currents in the Zeeman slower coils. We spend 30 ms to compress the cloud using a laser detuning of -27 MHz and a magnetic field gradient of B' = 27 G/cm.

Finally, we perform molasses cooling by turning off the magnetic field gradient and detune the laser frequency to -110 MHz. In 2 ms, the cloud reaches a temperature of 10 μK with a peak density around 10^{11} cm^{-3}. At the end of molasses, we turn off the REP beam before turning off the MOT beam. While it is on alone, the MOT beam polarizes the spin of the atoms to $|3, 3\rangle$ state.

4.3.3 Degenerate Raman Sideband Cooling (dRSC)

Degenerate Raman Sideband Cooling (dRSC) allows fast and efficient cooling. The cooling cycle can be decomposed into three stages, including Raman coupling, optical pumping, and spontaneous emission. Through applying the optical pumping, atoms go through the cycling process which reduces a quantum of vibrational energy each time till reaching the ground state as illustrated in Fig. 4.6.

Before explaining the cooling mechanism, we first go through the setup. Atoms are confined in deep three-dimensional optical lattices. The optical lattices serve to provide trapping as well as Raman coupling between $|m_F, \nu\rangle$ and $|m_F \pm 1, \nu \pm 1\rangle$ where ν is the vibrational quantum number in the individual lattice site. A bias magnetic field is applied to bring degeneracy between these two states. The lattice is deep enough to make the optical pumping operated in the Lamb-Dicke regime, meaning the vibration quantum energy is much larger than the recoil energy ($E_R = 2\pi \times 2$ kHz for Cs), and the electronic state is decoupled

from the motional state. The optical pumping beam has $\sigma+$ polarization and drives atoms from $|F = 3, m_F, \nu\rangle$ to $|F = 2', m_F + 1, \nu\rangle$, followed by spontaneous emission to the $|F = 3, \nu\rangle$ state. For atoms falling to $|F = 3, m_F + 1, \nu\rangle$ state and complete the cycle to go back to $|F = 3, m_F, \nu - 1\rangle$ through Raman coupling, the vibrational quantum number is reduced.

Atoms keep going through the same process and eventually arrive $|F = 3, m_F = 2, \nu = 0\rangle$ state. With a weak π component in the optical pumping, atoms are pumped to $|F = 2', m_F = 2, \nu = 0\rangle$ and could spontaneously fall into the dark ground state $|F = 3, m_F = 3, \nu = 0\rangle$. Atoms would then remain in the dark ground state with little chance to be excited by the optical pumping.

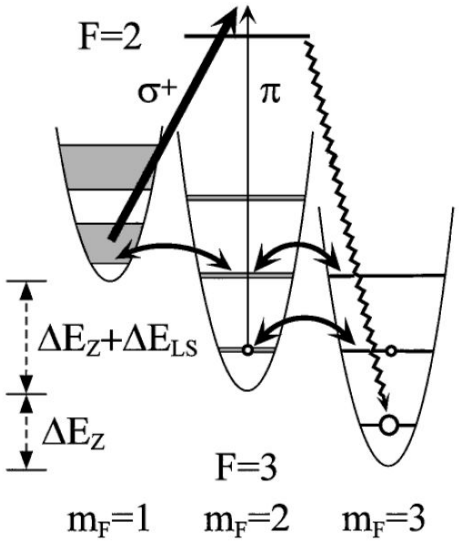

Figure 4.6: Illustration of the mechanism of degenerate Raman sideband cooling. Combination of optical pumping $\sigma+$ and Raman coupling (double-sided arrows) remove the vibrational energy of the atoms. A weak π component in the optical pumping beam drives atoms to the dark state. ΔE_z is the Zeeman shift and ΔE_{LS} is the light shift from the optical pumping. Figure reprinted from Ref. [80].

We apply dRSC to further cool down atoms. dRSC constrains a 3D optical lattice and an optical pumping beam [80]. The lattice laser beam is 20 GHz red detuned from the $3 \to 4'$ transition. With a total power of 70 mW and a 1 mm $1/e^2$ beam diameter, we estimate the geometric averaged trap frequency to be $\sim 2\pi \times 50$ kHz in the individual lattice site. A weak

magnetic field $(B_x, B_y, B_z) \sim (200, 560, 20)$ mG is applied to bring $|m_F, \nu\rangle$ and $|m_F \pm 1, \nu \pm 1\rangle$ into degeneracy. The magnetic field provides a Zeeman splitting $\Delta E = 1/4\mu_B B$ which equals to the vibration energy splitting $\hbar\omega$ in the optical lattice, where ω is the trap frequency. With a 3 ms cooling time followed by a 500 ms equilibration time, atom temperature reduces to 1 μK, and we still have 10 million atoms remaining in the optical dipole trap.

4.4 Evaporation

Laser cooling bring the phase space of the cold atom to close to one, but there is still a gap toward degeneracy. To fill in the gap, most people use evaporative cooling.

We perform forced evaporation by linearly decreasing the magnetic field gradient B' from 31.3 G/cm to 14.6 G/cm in 1 s, and to 6.7 G/cm in 1 s, and then to 0 G/cm in 1 s. The trap depth decreases from 20 μK next to 4.5 μK, and to 2 μK, and finally to 800 nK with the gradient completely removed. The magnetic field is ramped from 56 G to 24 G in the first 500 ms of the evaporation, and from 24 G to 20.7 in the final stage of the evaporation. During the evaporation we keep the scattering length large (300 a_0) for faster thermalization. After evaporation, we keep the scattering length to 200 a_0 which has a local three-body loss minimum due to the Efimov physics. The dipole trap strength is kept the same throughout the process. In the end, we achieve a BEC of 30,000 atoms with a temperature of 15 nK. The cloud size of the gas in the vertical direction is around 5 μm which can be reasonably held by the optical dipole traps against the gravity with magnetic levitation.

Note that 1D evaporation is supposed to be much more inefficient compared with 3D evaporation. Our cooling efficiency turns out to be quite close to the 3D efficiency. Possible mechanisms could be the inseparable potential and stochastic single particle motion [78]. In a realistic model, stochastic motion may be induced by the intensity irregularities in the trapping potential.

A brief table summarizes the performance at different cooling stages.

Table 4.1: Summarizing the cooling performance

cooling stage	Duration	atom number	temperature	atom density
MOT	2 s	40 M	40 μK	NA
CMOT	50 ms	40 M	40 μK	NA
Molasses	2 ms	40 M	10 μK	10^{11} cm^{-3}
dRSC	30 ms	20 M	2 μK	10^{12} cm^{-3}
Plain evaporation	500 ms	10 M	1 μK	10^{12} cm^{-3}
Forced evaporation	2 s	40 k	15 nK	10^{13} cm^{-3}

4.5 Preparation of 2D quantum gases with an optical lattice

To create a two-dimensional quantum gas, we confine the condensate in two dimensions with an one-dimensional optical lattice. The optical lattice is created by interfering two shallow angle incident 1064 nm lasers, see Fig. 4.7. With a crossing angle of 15°, the lattice period is 4 μm which is comparable and longer than the size of the condensate in the vertical dimension. With careful alignment, we can guarantee all the atoms to be loaded in a single lattice site.

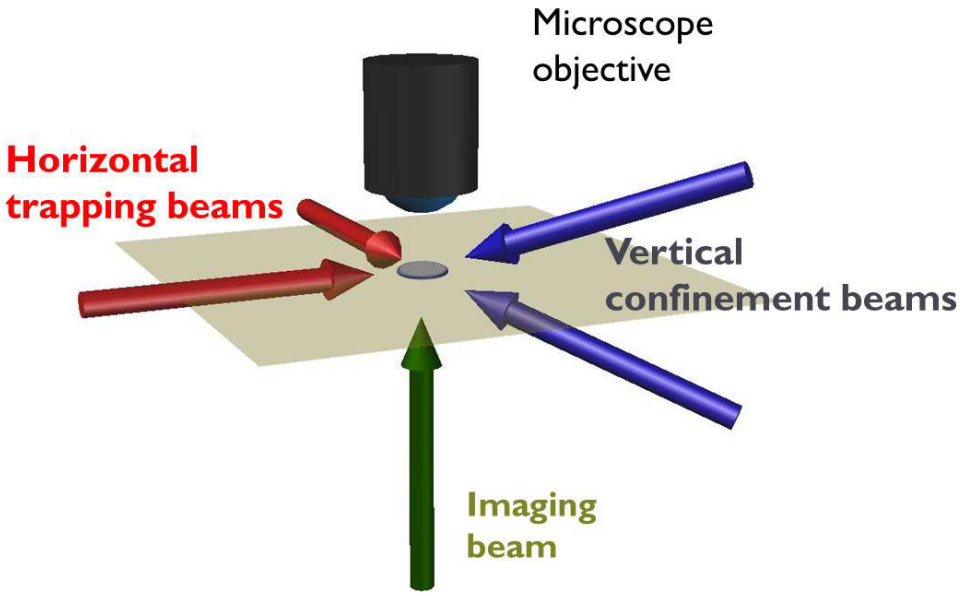

Figure 4.7: Optical setup for creating the 2D gas. The BEC is compressed by the lattice formed with two shallow angle incident laser beams. A crossed dipole trap provides horizontal confinement. We perform absorption imaging by illuminating the atoms with resonant imaging beam from below and probing with a high resolution objective from above.

The beam waists are 700 μm horizontally and 120 μm vertically. With a maximum power of 900 mW, we get a trap frequency of 1.8 kHz vertically in a single lattice site. The horizontal trap confinement is weaker than the trapping force from the crossed dipole trap.

We use the light sheet strength to fine tune the vertical position of the condensate in order to load all the atoms in a single layer of the lattice. To check whether the gas distributes in multiple layers, we perform microwave tomography. We apply a magnetic field gradient of 50 G/cm in the vertical direction, and the microwave transition frequency from $|3,3\rangle$ to $|4,4\rangle$ is shifted by 50 kHz between the neighboring lattice sites. This allows us to excite atoms in a specific layer and probe the atom number.

4.6 Probing the atoms

Our experiment relies heavily on the absorption imaging technique. It gives us the information of atomic density distribution. With *in situ* imaging, we extract thermodynamic quantities such as the equation of state. By allowing atoms to freely expand, we can also examine the momentum space the system, such as the temperature and the atomic dispersion. We will introduce the concept of absorption imaging, design of the imaging system, and the characterization of its performance.

4.6.1 Absorption imaging

We perform absorption imaging on the ultracold atomic cloud to measure the density distribution. For a homogenous light beam propagating in the z-direction, the intensity of the light beam reduces after passing through a dissipative sample. Assuming a dilute sample with a density distribution of $n(x,y,z)$ and a scattering cross section σ, the light beam intensity I attenuation can be estimated by Beer-Lambert law:

$$\frac{dI}{dz} = -n(x,y,z)\sigma I. \tag{4.3}$$

The column density $n_c(x,y)$ of the sample can be inferred from the attenuation of the light beam:

$$n_c(x,y) = \int n(x,y,z)dz = \int \frac{-1}{\sigma}\frac{dI}{I} = \frac{-1}{\sigma}\ln\frac{I_{out}}{I_{in}}, \tag{4.4}$$

where $I_{out}(I_{in})$ is the final (incident) intensity, and $\ln\frac{I_{in}}{I_{out}}$ corresponds to the optical density of the sample. With a spatial resolution of the light beam profile, we could also extract the spatial distribution of $n_c(x,y)$.

For the scattering process between atom and laser light, the scattering cross section depends on the laser intensity:

$$\sigma(I) = \frac{\sigma_0}{1 + I/I_{sat}}, \tag{4.5}$$

where $\sigma_0 = 3\frac{2\pi c^2}{\omega_0^2}\frac{A_{21}}{\Gamma}$ is the resonant cross section, ω_0 is the transition frequency, Γ is the transition linewidth, A_{21} is the rate of the spontaneous emission for the excited state, and $I_{sat} = \hbar\omega_0^3\Gamma/12\pi c^2$ is the saturation intensity. With an imaging beam intensity comparable to I_{sat}, the Beer-Lambert law is modified as the following form:

$$n_c(x,y)\sigma_0 = -\ln\frac{I_{out}(x,y)}{I_{in}(x,y)} + \frac{I_{in}(x,y) - I_{out}(x,y)}{I_{sat}}. \tag{4.6}$$

4.6.2 Imaging system

In our experiment, we illuminate atoms with a resonant laser beam from below. By comparing images with and without scattering from atoms, we determine the atomic density distribution. A custom-made objective (Special Optics, 54-26-26-852nm) with a numerical aperture of 0.5 and a working distance of 25.4 mm is implemented. Its material is non-metal in order to avoid eddy current. The objective is infinite conjugated and works together with an eye piece (Special Optics, 54-26-640-852nm) to give an imaging magnification factor of 21.8.

We use a CCD camera (Andor DU-434-BRDD) to measure the intensity profile of the laser beam for the absorption imaging. The camera chip is divided into three regions. Only

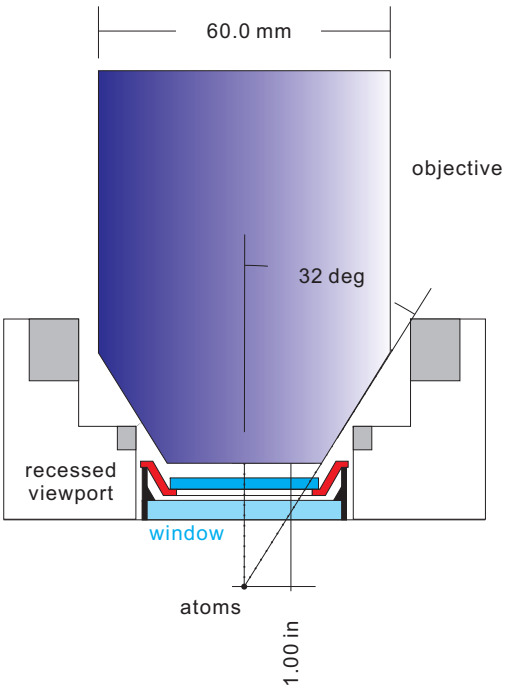

Figure 4.8: Design of the objective. The working distance of the objective is 25.4 mm, and the numerical aperture is 0.5. Between the objective and the atoms, there is a vacuum window and a composite optics allowing the imaging beam to transmit and reflecting the MOT beam. The objective is designed to compensate the aberration caused by the optics.

the top one-third of the area is used to exposure. The remaining two-thirds of the space are used for storing the signal before readout. The purpose is to perform two exposures separated by a short amount of time (20 ms). One exposure is made with atoms scattering the laser, and the other one is made without. Fringes caused by the multiple reflections in the optics can be problematic. Thus, it's crucial to keep the two exposures as close as possible in order to get a consistent fringe pattern for computing the image. The readout process takes about 1 s. The readout noise and the noise from the dark current are much smaller compared to the photon shot noise of the exposure.

Between the objective and the chamber window, we have a piece of custom-made optics. It contains a dichroic mirror, a polymer quarter waveplate, and a polarizer. The purpose is to integrate the imaging system with the magneto-optical trap. Three pieces are bound together with index-matching glue. The dichroic mirror reflects 1064 nm light and allows 852 nm light to pass. It's for future experiments which require an even tighter vertical confinement. A

vertical optical lattice can form by retro-reflecting the laser from the dichroic mirror. The versalight polarizer (Meadowlark Optics, VLR-100-NIR) is made of a thin layer of aluminum microwires on a glass substrate. It reflects 852 nm light with polarization aligning along the grid and allows light with orthogonal polarization to pass. The quarter wave plate turns the imaging laser polarization to the transmissive polarization of the versalight, and it makes MOT beam reflected by the versalight.

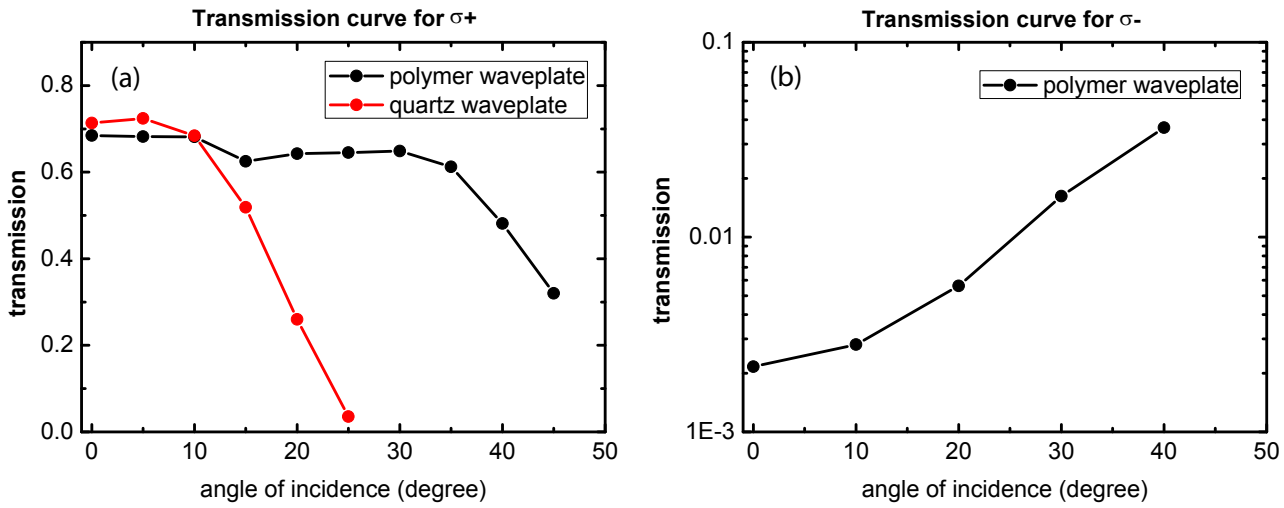

Figure 4.9: Calibration of transmission of the composite optics for different polarizations. $\sigma+$ corresponds to the imaging beam, and $\sigma-$ corresponds to the MOT beam. The comparison of the composite optics made of polymer waveplate and the regular waveplate is also shown on the left, and the polymer waveplate gives a larger working angle.

The polymer waveplate has very good optical properties, and its operation angle covers up to 35° without noticeable degradation. The overall transmission efficiency from this custom-made optics at different angles is shown in Fig.4.9. At the objective cutoff collection angle of 30°, we still have 60% transmission.

4.6.3 Modulation transfer function

The imaging imperfection limits the resolution as much as the numerical aperture does. We tried our best to optimize the imaging system. First, the objective is designed to compensate the aberration caused by the chamber window and the optics. We also characterize the

modulation transfer function of the imaging system. Based on the measurement, we remove the astigmatism and compensate the remaining aberration with defocusing. In the end, we get a resolution of 1 μm.

The imperfection of the imaging system leads to image distortion. A point object in the object plane would have a finite size in the image plane. The response function is known as the point spread function $P(r_i - r)$ which maps the original density distribution $n(r)$ to a convoluted measurement $n_{exp} = \int dr n(r) P(r_i - r)$.

One may also come to the Fourier space to examine the response function more carefully. With the help of convolution theorem, we rewrite the relation between the original density distribution and the measurement as $n_{exp}(k) = n(k)P(k)$, where $n_{exp}(k)$, $n(k)$ and $P(k)$ are the Fourier transform of $n_{exp}(r)$, $n(r)$ and $P(r_i - r)$.

In Fourier optics, the objective performs optical Fourier transform. $P(k)$ is equivalent to the exit pupil function and can be written as

$$P(\rho, \theta) = U(\rho, \theta) e^{i\Theta(\rho,\theta)}, \tag{4.7}$$

where $U(\rho, \theta)$ is the transmittance function and $\Theta(\rho, \theta)$ is the waveform distortion function. U can be modeled as $U(\rho) = H(1 - \rho)e^{-\rho^2/\tau^2}$, and $H(x)$ is the Heaviside step function. The lowest few orders of the aberration function include

$$\Theta(\rho, \theta) \approx S_0 \rho^4 + \alpha \rho^2 \cos(2\theta - 2\phi) + \beta \rho^2, \tag{4.8}$$

where S_0 is the aberration coefficient, α is the astigmatism coefficient with ϕ corresponding to the azimuthal angle of the misaligned axis, and β is the defocusing coefficient.

One approach to measure the $P(k)$ would be measuring the noise power spectrum of the gas:

$$\langle |\delta n_{exp}(k)|^2 \rangle = N S(k) M^2(k), \tag{4.9}$$

Table 4.2: Aberration function coefficients of the system

systems	cutoff (k_L^{-1})	aberration (k_L^4)	astigmatism (k_L^2)	defocusing (k_L^2)
old system	0.33	966	9.1	42
new system (tilted)	0.62	33	3.1	5
new system	0.63	45	0.5	4

where $\delta n_{exp}(k)$ is the Fourier transform of $\delta n_{exp}(r) = n_{exp}(r) - \bar{n}_{exp}(r)$, $\bar{n}_{exp}(r)$ is the mean density averaged over multiple shots, N is the total particle number, S is the structure factor of the gas, and $M(k) = |P(k)|$ is the modulation transfer function of the imaging system.

In the absorption imaging, atoms scatter the photons of the incident field. With an incident field strength E_0, one can model the scattering by introducing a coherent dark field $\Delta E \propto e^{i\delta_s} E_0$ which interferes with fields of the original plane wave. δ_s accounts the dispersive effect given by the off-resonant scattering. The corresponding transmission is $t^2 = |E_0 + \Delta E|^2/|E_0|^2 \sim 1 + 2R[\Delta E/E_0]$, where $R[.]$ refers to the real part. From the earlier section, we have $n_{exp} \sim -\ln(t^2) + (1 - t^2) I_0/I_{sat}$, where I_0 is the incident laser intensity and I_{sat} is the saturation intensity. One then finds that $n_{exp} \sim -2(1 + I_0/I_{sat}) R[\Delta E/E_0]$, and the point spread function is proportional to the amplitude of the scattered field.

We use a two-dimensional thermal gas to characterize our imaging system. The gas is supposed to be structureless, and $S(k) = 1$. Fig.4.10 shows the analysis of the image response function. The first one corresponds to the performance with a commercial NA = 0.28 objective (Tech-specialties, OKHNL10). The second one shows the MTF of a custom made objective. The azimuthal variation is caused by a 0.6° tilt of the objective. After compensating the tilt, we arrive the third one which is only dominated by the aberration. We fit the experimental measurement with the model introduced above. The overall result can be found in Table. 5.1.

To get a quantitative understanding of the coefficient, we use a simple illustration to analyze the origin of the aberration, see Fig.4.11. Consider a light beam passing through an optics with a thickness l and index of refraction n, the optical path difference caused by the optics depends on the propagating angle θ with respect to the optical axis and can be

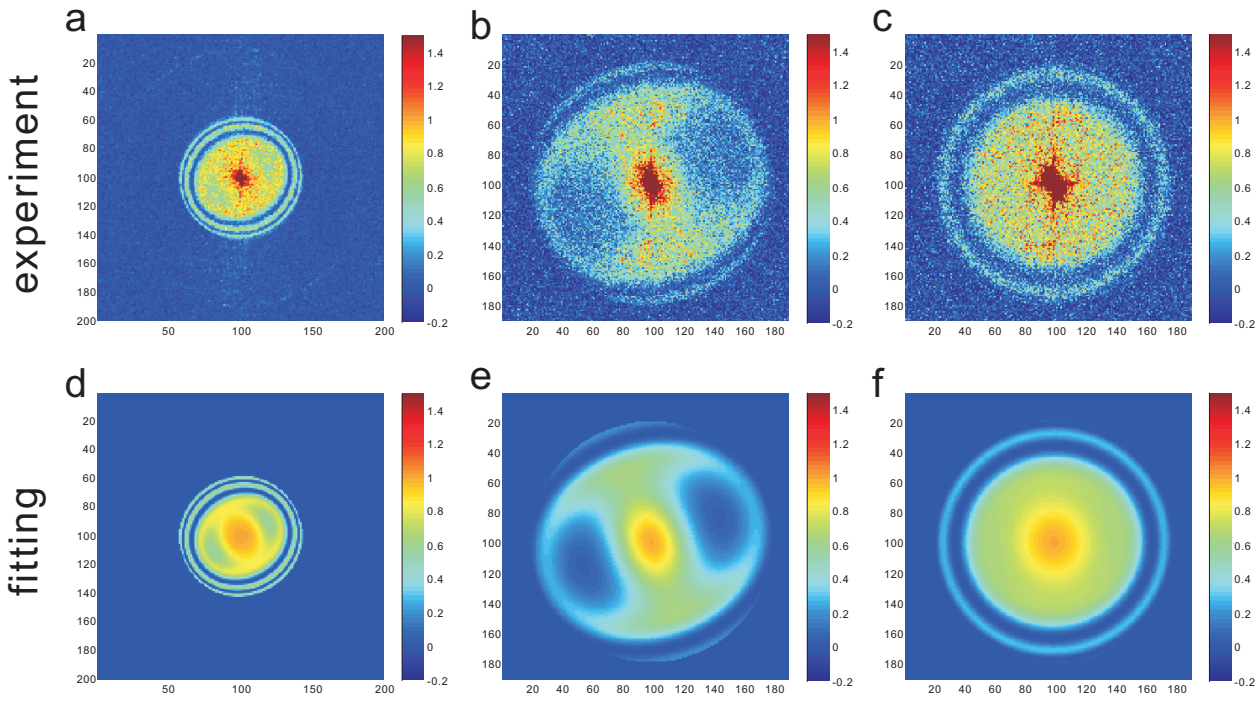

Figure 4.10: We measure the modulation transfer function, our model allows us to determine the defocusing with 1μm precision. (a) corresponds to the MTF of using the commercial objective with a NA equal to 0.28. (b) is the MTF after upgrading the system with a custom-made aberration cancellation objective. The NA is 0.5. The dipole pattern is originated from the astigmatism of the tilted imaging system. (c) is the astigmatism compensated MTF. The remaining aberration still limits the maximum resolvable frequency component in space. (d) to (f) correspond to the fitted parameters of the experimental measurements. The space is between $-\pi/d$ and π/d, where d is the pixel size of the image and it defines the highest spatial frequency we can resolve from the image. The result can be found in the Table. 5.1.

written as

$$\begin{aligned}\frac{\lambda}{2\pi}\cdot d\phi &= \frac{f-l}{\cos\theta}+\frac{nl}{\cos\theta'}-[(f-l)\tan\theta+l\tan\theta]\cdot\frac{1}{\sin\theta}\\ &= \frac{nl}{\cos\theta'}-\frac{l}{cos\theta}\cdot\frac{\sin\theta'}{\sin\theta}\approx(nl-\frac{l}{n})\cdot[1+\frac{1}{2}\cdot(\frac{\sin\theta}{n})^2+\frac{3}{8}(\frac{\sin\theta}{n})^4+...],\end{aligned} \tag{4.10}$$

where λ is the wavelength, $d\phi$ is the accumulated phase difference, f is the projection plane, and $\sin\theta' = n\sin\theta$ given by the Snell's law. Since the absorption imaging technique works by having the dark field interfering with the original field, the light beam propagating with angle θ is linked to spatial information with a wavevector of $k_L\sin\theta$. Setting the waveform

distortion function in unit of $k_L = 2\pi/\lambda$, we then have

$$S_0 = \frac{2\pi}{\lambda} l(n - \frac{1}{n})\frac{3}{8}\frac{1}{n^4}. \tag{4.11}$$

With an index of refraction $n = 1.452$ for fused silica, we estimate the remaining aberration is contributed by an uncertainty of 160 μm material in our original design.

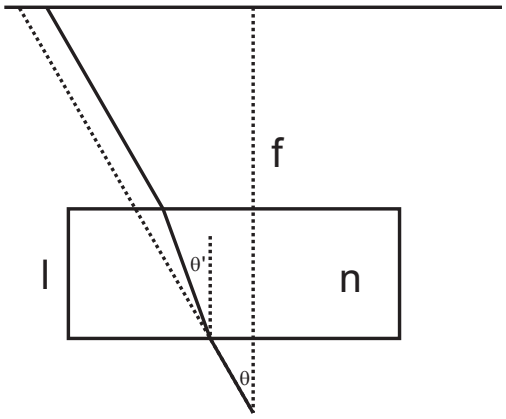

Figure 4.11: Illustration for estimating the aberration coefficient from a material with a thickness l and an refraction index of n.

4.7 Optical lattice

Our optical lattice is formed by interfering the dipole trap laser and its retro-reflection as shown in Fig. 4.12. The beam passes through two acousto-optical modulators (AOMs) powered by the same frequency source. We select the opposite diffraction orders, so the laser frequency remains the same. A lens focuses the dipole trap laser on the end mirror and collimates the beam after the reflection. The pointing of the beam could remain the same even if we adjust the RF frequency drifts [81], and the interference standing wave can be kept stable. However, changing the RF frequency would change the relative phase of the acoustic waves in the two AOMs due to the finite electrical cable length difference. The phase of the optical lattice would be shifted.

Experimentally, we calibrate the lattice depth by measuring the band gap between the

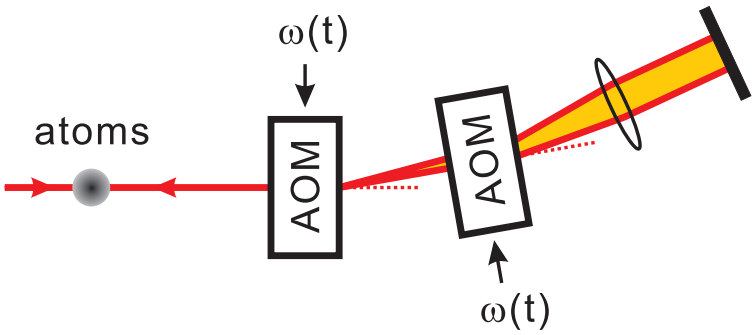

Figure 4.12: The lattice beam passes through two AOMs operating at the same frequency (from the same source), passing each AOM twice. The total frequency shift is zero so the return beam can make a lattice with the incoming beam. The lens is positioned so that the AOM frequency can change while maintaining the retro-reflection condition. When the AOM frequency changes, a phase shift develops due to the phase difference of two RF signals caused by the cable length difference. The phase shift of the laser beam leads to a phase change of the optical lattice.

ground band and first excited band at zero quasi-momentum. By quickly displacing the phase of the optical lattice, we excite part of the cloud to the first excited band. The wavefunction evolves at different rate and can be written as

$$|\Psi(\tau)\rangle = \sum_{n=0}^{\infty} a^n e^{iE_0^n \tau/\hbar} |\phi_0^n\rangle, \tag{4.12}$$

where τ is the evolution time, and $a^n = \langle \phi_0^n | \hat{X} | \phi_0^0 \rangle$. The perturbation we provide produces combination of ϕ_0^0 and ϕ_0^1.

When projecting the wavefunction to free space, these two wavefunctions can interfere in the basis of the plane wave. The composition of the Bragg diffraction orders would depend on the phase difference accumulate between two states. From the oscillation of Bragg peaks' strength at different wait time, we can determine the band gap and the corresponding lattice depth.

To calibrate the amplitude of the phase modulation, we apply the same technique we used to measure the lattice depth. We measure the interference of Bragg peaks. Instead of varying the probe time, we use a fixed the wait time and vary the amount of displacement. When the displacement is a multiple of lattice constant, the matter wave remain undisturbed.

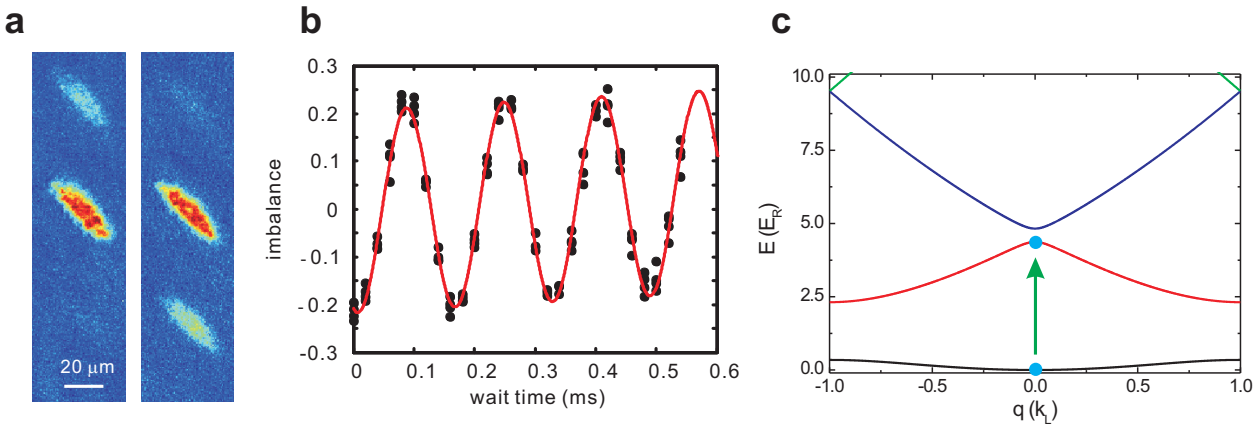

Figure 4.13: We calibrate the lattice depth by displacing the lattice phase. It couples some atoms from the ground band to the first excited band. They interfere when we project the gas to the free space. (a) shows the diffracted Bragg peaks. (b) shows the peak imbalance. The calibrated frequency is 6.21 kHz which corresponds to a lattice depth of 4 E_R. (c) shows the illustration of the coupling.

4.8 Projecting system

We setup another optical system to project an optical potential on the atomic cloud. The projection system is integrated with the imaging system with a dichroic mirror which reflects the imaging beam while allowing the projecting beam to transmit. We use blue-detuned 789 nm diode laser to create a repulsive optical potential. One of our goals is to create a quantum gas with homogeneous density distribution. A flat-bottom trap can be created by canceling the trap curvature from the harmonic confinement with the repulsive dipole potential.

We have implemented a digital micromirror device (DMD: Texas Instruments, DLP LightCrafter 3000) to tailor dynamic optical potentials for probing the dispersion. The DMD consists of a 608×684 array of 7.6 μm square mirrors. Each mirror flips individually to one of two angles, separated by 12°. A mirror at the "on angle will reflect light towards the atom cloud, while the "off" angle reflects light into a beam dump. We reflect a blue-detuned 789 nm laser off of the DMD and use a high-resolution objective lens to project the real space pattern of mirrors in the "on" state onto the plane of the atom cloud. We use additional lenses to demagnify the pattern by a factor of 36. The resolution of the resulting patterns

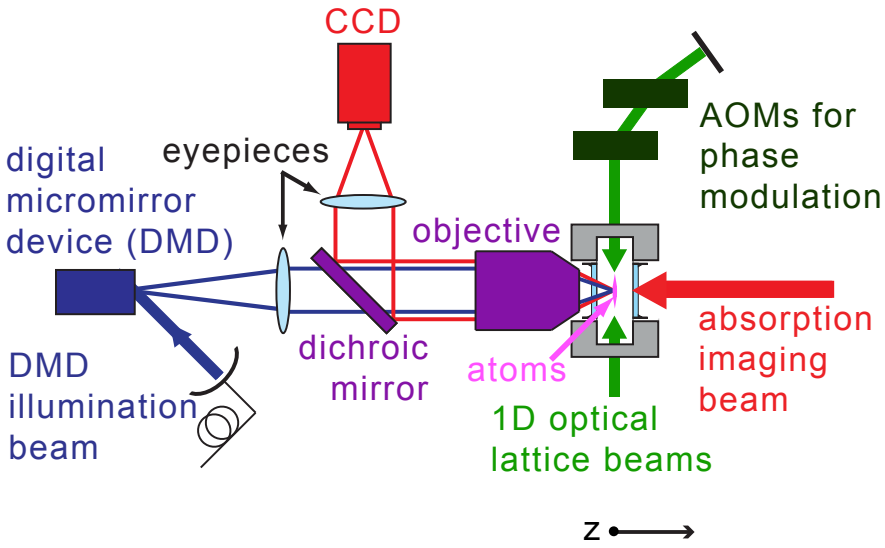

Figure 4.14: Our optical setup is based on a single high resolution objective lens, which allows us both to perform absorption imaging and to project arbitrary patterns from the DMD onto the atoms (see supplemental text for details). The 1D optical lattice is formed by retro-reflecting one of the 1064 nm dipole trap beams after passing it through two acousto-optic modulators (AOMs), which can be used to phase modulate the lattice [161].

is limited by the objective lens to ~1 μm, approximately 5 micromirrors across. By having many micromirrors in each resolution sized area we can generate intermediate intensities in static patterns even though the state of each micromirror is binary. The programmed pattern of "on" mirrors can be updated up to 4000 times per second, allowing us to create motion in the projected patterns.

With a 50 mW laser power out of the fiber focusing in an area of 100 μm-by-100 μm, one gets a trap depth of 2.3 μK. Considering the diffraction efficiency from the DMD (10 %) and the transmission efficiency through the dichroic mirror (90 %) and 3-in-1 optics (40 %), this is still comparable to the trap depth variation in a 10 Hz dipole trap (80 nK).

In the projection setup for the DMD, there is also a steering mirror between the eye piece and the dichroic mirror (not shown). The purpose is to cancel the day-to-day drift of the laser pointing. Empirically, we only need a fine tuning to compensate a drift of few μm on the daily basis.

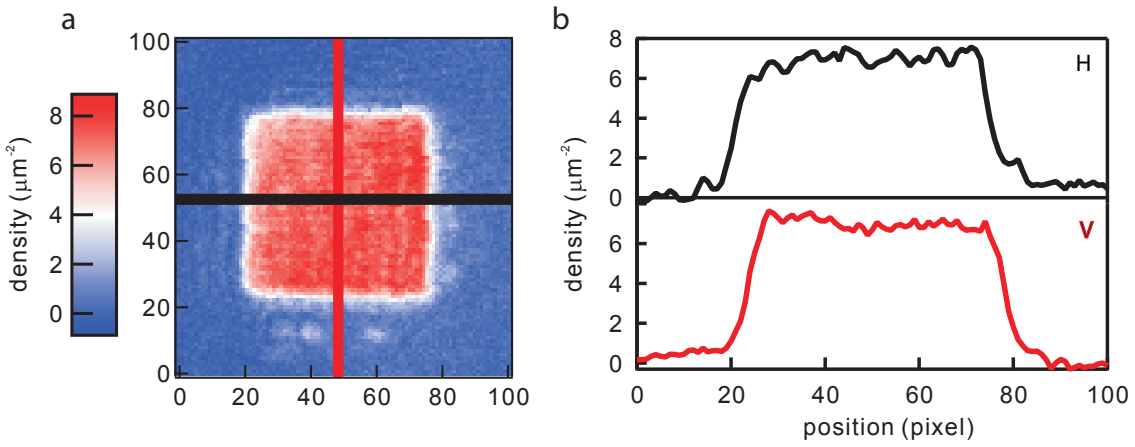

Figure 4.15: We use a 789 nm laser to compensate the harmonic confinement from the optical dipole trap. (a) shows the image of the gas trapped in a combined trap from a vertical lattice, crossed dipole trap, and the blue detuned beam. The blue detuned beam is composed of a square well and a gaussian potential within the well for cancelling the harmonic confinement. (b) shows the homogeneity of the gas density along different line cuts.

4.8.1 Projection Bragg spectroscopy

Bragg spectroscopy of a condensate can be performed by imposing a periodic traveling wave potential on the atoms. One can achieve this by illuminating the atomic cloud with two laser beams which have wave vectors of k_1 and k_2 and frequency difference ω. Atoms can undergo stimulated light scattering by absorbing one photon from a laser beam and emit one to the other. In the process, atoms gain momentum transfer of $\hbar q = \hbar(k_1 - k_2)$ and energy difference of $\hbar\omega$. The excitation happens resonantly when atoms have excitation state which satisfies the energy and momentum conservation.

We create an optical lattice by projecting atoms with a laser diffracted off the DMD whose pattern is a one-dimensional periodic structure. The wavelength and phase of the DMD pattern can be programmed easily. By dynamically changing the phase of the pattern, one realizes a moving optical lattice with a single laser.

In order to create a moving lattice with a single-wavevector for Bragg spectroscopy, we add additional beam selection masks in front of the DMD as shown in Fig. 4.16. The DMD pattern is only an approximation of sinusoid, higher order harmonics show up upon diffraction. By allowing only two diffracted beams to transmit through a mask we ensure

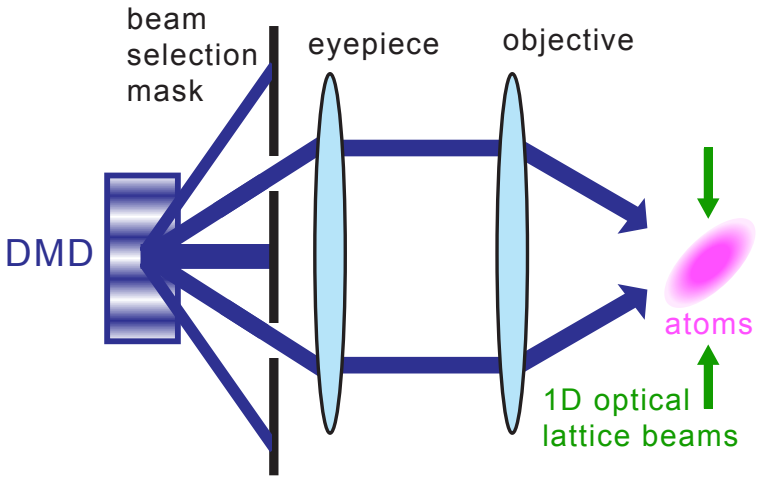

Figure 4.16: In order to project clean optical potentials for probing dispersion, beam selection masks transmit only the two desired beams diffracted from the DMD. In this way the interference pattern on the atoms contains no confounding wavevectors.

that the projected optical potential contains only the desired wavevector for probing the atoms. Shifting the pattern of the "on" mirrors translates the projected potential by the same amount regardless of the blocking mask.

An additional advantage of using the selection mask is to double the maximum projected wavevector. By blocking the 0'th order diffraction and selecting the ±1'st, we create a projected lattice with a spatial frequency twice larger than what is given by the DMD. That wavevector is limited by the objective lens to approximately $k = 0.55\ k_L$. Once the 0'th order beam is blocked, the interference between the 1'st and -1'st dominates, which raises the maximum projected wavevector to approximately $k = 1.1\ k_L$ and is sufficient for our experiments.

For any wavevector of the projected potential, the quasiparticle excitation frequency corresponds to the rate at which the pattern's phase shifts by 2π. We typically use sets of 9 lattice patterns, so that each pattern switch corresponds to a phase change of $2\pi/9$. We scan the excitation frequency by changing the rate at which we trigger the DMD to cycle through the set of patterns. To make the movement smoother for probing the small excitation frequencies, we use sets of 20 patterns instead.

The dispersion relation corresponds to the points in wavevector and frequency space at

which we observe resonant heating of the atom cloud. We determine those points by probing the atomic sample at a fixed wavevector and scanning the DMD triggering frequency. We typically apply the exciting optical potential to the cloud for 40 ms, and then perform 30 ms time of flight (TOF) to determine the number of atoms remaining in the condensate. When the excitation is resonant, atoms are excited out of the condensate, which we can observe as a depletion of the atom number in the momentum state of the condensate after TOF. Fig. 4.17 shows an example loss curve. The fit is to a Gaussian whose center we take to be the resonance frequency. The resonance frequency is not sensitive to the particular fit function chosen: fitting to a Lorentzian instead of a Gaussian typically shifts resonances by tenths of Hz.

The example images in Fig. 4.17 show the difference between the full and depleted clouds. For this excitation, which at $k = 0.44\ k_{\mathrm{L}}$ is near the roton momentum, the atoms missing from the main condensate peak (inside the solid white circles) appear at the right side of the image in a location corresponding to the roton momentum after TOF (inside the dashed white circle). For applied potentials with wavevectors far from the roton minimum, the excited atoms do not always appear in a predictable place. However, the depletion of the condensate remains a consistent signal for all excitation measurements and therefore we use it for determination of the atomic excitation spectrum.

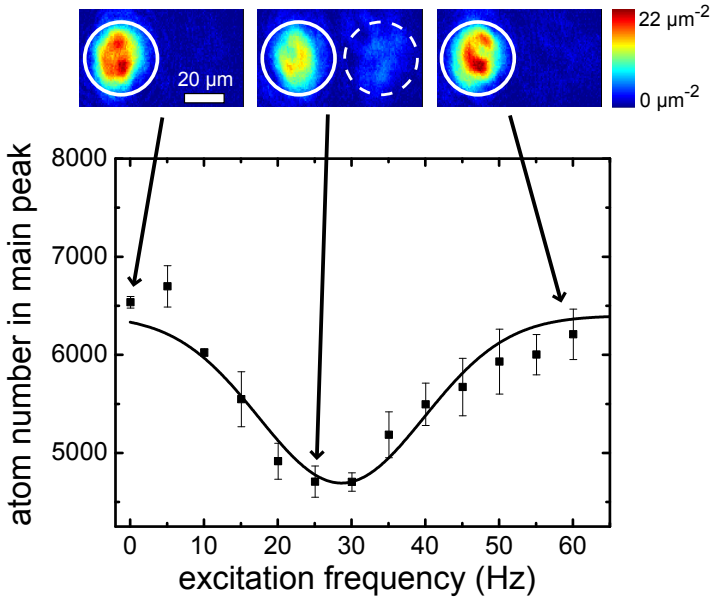

Figure 4.17: This plot shows the atom number detected in the main peak after applying an excitation of varying frequency with k = 0.44 k_{L} to an atomic sample with a = 13 a_0. Example images (each the average of 4 or 5 experimental trials) illustrate the TOF results. Diffraction peaks from the lattice are outside of the field of view. The atom number is determined by integrating the signal present in the solid white circle. The central image, corresponding to a near-resonant frequency, has a clearly depleted main peak. The dashed white circle indicates the location where atoms transferred to the roton minimum appear after TOF. The solid curve in the plot is a Gaussian fit which yields the excitation frequency of 29(3) Hz.

CHAPTER 5

STRONGLY INTERACTING TWO-DIMENSIONAL BOSE GASES

We prepare and study strongly interacting two-dimensional Bose gases in the superfluid, the classical Berezinskii-Kosterlitz-Thouless (BKT) transition, and the vacuum-to-superfluid quantum critical regimes. A wide range of the two-body interaction strength $0.05 < g < 3$ is covered by tuning the scattering length and by loading the sample into an optical lattice. Based on the equations of state measurements, we extract the coupling constants as well as critical thermodynamic quantities in different regimes. In the superfluid and the BKT transition regimes, the extracted coupling constants show significant down-shifts from the mean-field and perturbation calculations when g approaches or exceeds one. In the BKT and the quantum critical regimes, all measured thermodynamic quantities show logarithmic dependence on the interaction strength, a tendency confirmed by the extended classical-field and renormalization calculations.

5.1 Introduction

Two-dimensional (2D) Bose gases are an intriguing system to study the interplay between quantum statistics, fluctuations, and interaction. For noninteracting bosons in 2D, fluctuations prevail at finite temperatures and Bose-Einstein condensation occurs only at zero temperature. The presence of interaction can drastically change the picture. With repulsive interactions, fluctuations are reduced and superfluidity emerges at finite temperature via the Berezenskii-Kosterliz-Thouless (BKT) mechanism [68, 69]. Interacting Bose gases in two dimensions and BKT physics have been actively investigated in many condensed matter experiments [85, 86, 84, 87, 88]. In cold atoms, the BKT transition and the suppression of fluctuations are observed based on 2D gases in the weak interaction regimes [89, 90, 91, 53].

Extensive theoretical research on 2D Bose systems addresses the role of interactions in

the superfluid phase [92, 70, 93, 94, 95, 96] and near the BKT critical point [71, 72]. In the weak interaction regime, the classical ϕ^4 field theory [71, 72] predicts the logarithmic corrections to the critical chemical potential $\mu_c = k_B T(g/\pi)\ln(13.2/g)$ and the critical density $n_c = \lambda_{dB}^{-2}\ln(380/g)$ for small two-body interaction strength $g < 0.2$. Here $k_B T$ is the thermal energy and λ_{dB} is the thermal de Broglie wavelength. The classical-field predictions are consistent with weakly interacting 2D gas experiments [97, 90, 91, 53].

Intriguing dependence on the interaction strength g is also predicted in the ground state properties of interacting 2D Bose gases. Popov showed that the ground state chemical potential μ deviates from the mean-field result $\mu_{MF} = \hbar^2 g n/m$ logarithmically [70]. Here, m is the mass of the boson, n is the density, and $2\pi\hbar$ is the Planck constant. Defining the superfluid coupling constant as $G = m/(\hbar^2\kappa)$, where $\kappa = \partial n/\partial\mu$ is the compressibility, we can summarize the perturbation expansion result of G as [92]

$$G = \frac{g}{1 + Ag\ln g + Bg + Cg^2\ln g + Dg^2 + ...}, \tag{5.1}$$

where $A = -1/4\pi$ [70], $B = (\ln 4 - 2\gamma - 2)/4\pi$ [93], $C = -1/16\pi^2$ [92], the value of D remains controversial [94, 95], and γ is Euler's constant. To the best of our knowledge, there is no systematic experimental study testing Eq. (5.1).

Beyond perturbation, calculations based on the renormalized classical Ginzburg-Landau theory [98, 99] at finite temperature yield the result $G = \frac{2\pi g}{2\pi + g}$ [100]. A recent nonperturbative renormalization-group (NPRG) calculation also provides complete thermodynamic calculations. Near the vacuum-to-superfluid quantum critical point, where the chemical potential $\mu = 0$ and the temperature $T = 0$, dimensionless pressure $\tilde{P}$ is approximated to be $\tilde{P} = g_2(e^{-(g/9.1)W(9.1/g)})$, where $g_2(x) = \sum_{k=1}^{\infty} x^k/k^2$ is the Bose function. $W(x)$ is the Lambert function satisfying $W(x)e^{W(x)} = x$, and the dimensionless density is $\tilde{n} = -\ln(1 - e^{-(g/3.8)W(3.8/g)})$ [102, 101].

In this Chapter, we extend our previous work on weakly-interacting 2D Bose gases [53] into the strong interaction regime. We test the above theoretical predictions in different

regimes (see Fig. 7.1) and our measurements show significant deviations from the mean-field theory as well as the logarithmic dependence on the interaction strength.

A continuous evolution of a 2D quantum gas from the weak interaction ($g \ll 1$) to the strong interaction ($g \gtrsim 1$) regime is achieved by tuning the magnetic field near a Feshbach resonance [7] and by combining experiments with and without an optical lattice. Optical lattices enhance the interaction strength by increasing the on site density and the effective mass m^*. The definition of g for a 2D gas (no lattice) is given in Refs. [103, 104, 105] and for a 2D lattice gas given in Ref. [106]. Both definitions are mutually consistent and can be connected to the 2D interaction strength $g = 4\pi/|\ln na_{2\mathrm{D}}^2|$, where $a_{2\mathrm{D}}$ is the scattering length in two dimensions [107].

5.2 Experiment

We start our experiment by preparing a degenerate Bose gas of cesium atoms in a two-dimensional optical trap [53, 106]. The atoms are polarized in the lowest hyperfine ground state $|F = 3, m_F = 3\rangle$, where F is the total angular momentum and m_F is its projection. The radial and axial angular trap frequencies are $(\omega_x, \omega_y, \omega_z) = 2\pi \times (8, 10, 1900)\,\mathrm{Hz}$. The sample contains 2×10^4 atoms with temperature $T = 13 - 20\,\mathrm{nK}$, well below the excitation energy in the z direction such that the sample is in the quasi-2D regime [103]. We use a magnetic field to tune the atomic scattering length $a = 40 - 580\,a_0 \ll l_z$ near a low field s-wave Feshbach resonance where scattering length crosses zero at 17 G [108]. Here, a_0 is the Bohr radius and $l_z = 200\,\mathrm{nm}$ is the harmonic oscillator length in the z direction. The corresponding interaction strength is $g = 0.05 - 0.77$. Sample images are shown in Fig. 5.1.

To further enhance the interaction, we load the 2D gas into an optical lattice. A 2D square lattice is formed with a lattice constant of 532 nm, and the depth is set to be $V = 7.1\,E_{\mathrm{R}} = k_{\mathrm{B}} \times 450\,\mathrm{nK}$, where the tunneling energy is $t = k_{\mathrm{B}} \times 2.5\,\mathrm{nK}$, the effective mass is $m^* = 2.9(1)\,m$, E_{R} is the recoil energy, and k_{B} is the Boltzmann constant. At this lattice depth, the system is far from the unity-filling Mott insulator phase and, for all interaction strengths we study,

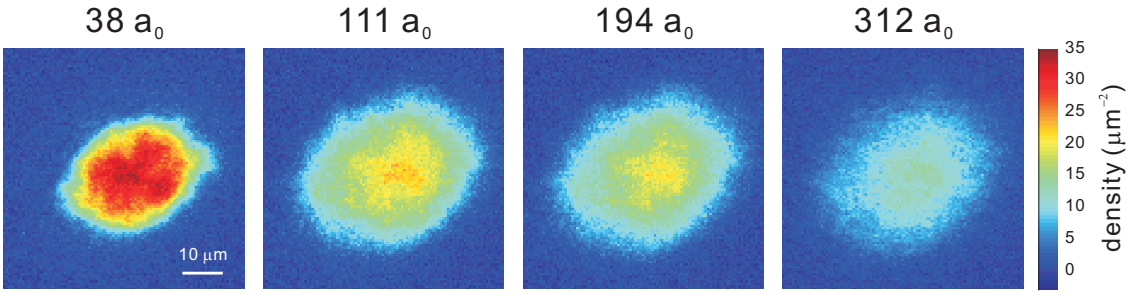

Figure 5.1: Averaged *in situ* images of 2D gases with different scattering lengths.

the ground state of the system remains in the superfluid phase. For 2D lattice gases, we can tune the interaction strength up to $g = 2.8$.

To ensure thermal equilibrium, we prepare the gases at different interaction strengths by adiabatically ramping the magnetic field and the lattice potential. For all 2D gas experiments, we use a 200 ms magnetic field ramp which is slow compared to the time scale of the radial motion. For the 2D lattice experiments, we adopt an adiabatic lattice potential ramp of 400 ms [109]. The magnetic field ramp is performed within the first 200 ms of the lattice ramp. For both the 2D gas and the 2D lattice gas, we monitor the subsequent density distribution for up to 200 ms after the ramp and observe no detectable dynamics and insignificant atom loss [110].

5.3 Equation of state measurement

5.3.1 Determinating the chemical potential and temperature

We determine the equations of state by measuring *in situ* atomic density profiles based on absorption imaging with a high resolution objective (numerical aperture = 0.5). Imaging aberrations are carefully characterized [111]. As a result, we achieve a spatial resolution of 1.0 μm. The atomic density is calibrated by the number fluctuation of a normal gas [53]. The measured density profiles are then converted into the equation of state $n(\mu, T, g)$ based on local density approximation [112], where μ and T are determined by fitting the density tail [113, 53, 106]. Note that we define the zero of the chemical potential to be the energy of

the lowest available single particle state in order to compare the equations of state of both 2D gases and 2D lattice gases.

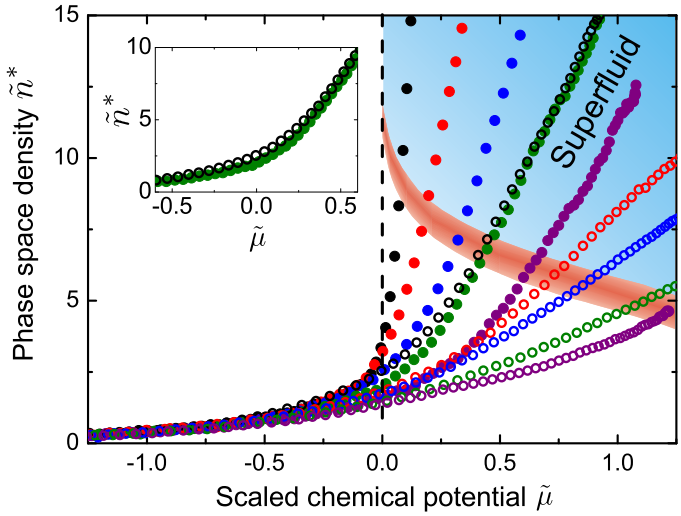

Figure 5.2: The filled circles represent measurements of 2D gases with (from left to right) $g = 0.05$ (black), 0.15 (red), 0.24 (blue), 0.41 (green), and 0.66 (purple). The open circles represent measurements of 2D lattice gases with (from left to right) $g = 0.45$ (black), 0.85 (red), 1.2 (blue), 1.9 (green), and 2.8 (purple). The upper blue shaded area is the superfluid regime, and the red boundary corresponds to the BKT transition regime. The black dashed line $\tilde{\mu} = 0$ indicates where we evaluate the density and pressure for a vacuum-to-superfuid quantum critical gas. The inset compares the equations of state of a 2D gas and a 2D lattice gas with an almost identical $g \approx 0.4$.

We plot the equations of state of 2D gases and 2D lattice gases in the dimensionless form $\tilde{n}^*(\tilde{\mu})$, where $\tilde{n}^* = n\lambda_{\mathrm{dB}}^{*2}$ is the phase space density, $\lambda_{\mathrm{dB}}^* = h/\sqrt{2\pi m^* k_{\mathrm{B}} T}$ is the thermal de Broglie wavelength, and $\tilde{\mu} = \mu/k_{\mathrm{B}}T$ is the dimensionless chemical potential [114]. For 2D gases, the effective mass is $m^* = m$. Samples of the measured equations of state are shown in Fig. 1. In particular, two equations of state with a similar $g \approx 0.4$, one from a 2D gas with $a = 310\,a_0$ and one from a 2D lattice gas with $a = 40\,a_0$, are compared in the inset of Fig. 7.1. The overall matching behavior of the two equations of state justifies our use of optical lattices to enhance the interaction. The small discrepancy near $\tilde{\mu} \approx 0$ will be discussed below.

5.4 Extraction of the coupling constants

In the superfluid regime, we extract the coupling constant $G_{\rm SF} = m^*/(\hbar^2\kappa)$ by evaluating the superfluid compressibility $\kappa = \partial n/\partial\mu$; see Fig. 7.2. The coupling constants show significant down-shifts from the mean-field prediction when the system enters the strong interaction regime. Similar tendency is also shown in the Ginzburg-Landau calculation [99] as well as in a recent work [115] which includes effective three-body interactions.

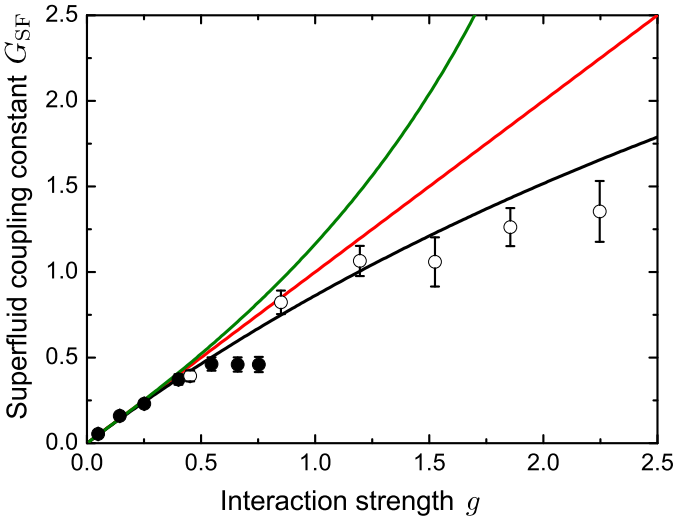

Figure 5.3: We determine $G_{\rm SF}$ by fitting the slope of the equations of state in the superfluid region for 2D gases (filled circles) and 2D lattice gases (open circles). Extensions of theoretical predictions into the strong interaction regime based on the third-order perturbation expansion [92] (upper green line) [see Eq. 5.1], the mean-field theory (middle red line), and the Ginzburg-Landau theory [99] (bottom black line) are shown for comparison. The error bars are dominated by the uncertainty of the density calibration.

In the BKT transition regime, we use the universal critical behavior of the equations of state to determine the critical parameters [53, 106]. By rescaling and overlapping [116] all the equations of state in the transition regime according to

$$\tilde{n}^* - \tilde{n}^*_{\rm c} = H(\frac{\tilde{\mu} - \tilde{\mu}_{\rm c}}{G_{\rm c}}), \tag{5.2}$$

we obtain the critical phase space density $\tilde{n}^*_{\rm c}$, the critical chemical potential $\tilde{\mu}_{\rm c}$, and the

critical coupling constant G_c; see Fig. 7.3. $H(x)$ is a generic function that describes the universal behavior near the BKT transition regime [53]. Remarkably, equations of state of all 2D gas and 2D lattice gas measurements overlap excellently; see Fig. 7.3 (a) inset.

The extracted critical coupling constants G_c are consistently lower than the mean-field values $G = g$. On the other hand, the extracted scaled critical chemical potentials $\tilde{\mu}_c$ and scaled critical densities $\tilde{n}_c^*$ follow the logarithmic dependence on g predicted by the classical-field calculations [71, 72, 99]. Our results confirm the crucial role of interactions in 2D Bose gases and suggest that the extensions of the above theories into the strong interaction regime capture the general behavior of the thermodynamic quantities.

Finally, we investigate the pressure and density in the quantum critical regime. In the lattice, atoms reach the vacuum-to-superfuid quantum critical regime when the chemical potential matches the lowest single particle state, and when the thermal energy is below the ground band bandwidth [106]. We extend the definition of quantum criticality to 2D gases [104]. To determine the pressure, we integrate the density over the chemical potential, $\tilde{P}_0^* = \int_{-\infty}^{0} \tilde{n}^* \mathrm{d}\tilde{\mu}$. The extracted $\tilde{P}_0^*$ in 2D gases and 2D lattice gases are compared with the mean-field and NPRG calculations [101]; see Fig. 7.5 (a). Here, we observe overall agreement between experiment and theories. For lattice gases, in particular, the slightly higher $\tilde{P}_0^*$ even in the weak interaction regime is discussed in Ref. [101] as the result of finite temperature effect. The densities in the quantum critical regime $\tilde{n}_0^*$ also show the expected logarithmic dependence on the interaction strength. Here, we observe small systematic deviations from the theories.

5.5 Conclusion

To conclude, we report the preparation and thermodynamic study of stable strongly interacting 2D gases. Dimensionless coupling constant g as high as 2.8 is reached by Feshbach tuning in an optical lattice. In the strong interaction regime, coupling constants show clear deviations from the mean-field theory. Other thermodynamic quantities in the classical and

quantum critical regimes show strong dependence on g and can be captured well by extensions of the classical-field theories and the NPRG calculation. Our results provide new insight into the crucial role of interactions in the thermodynamics of 2D gases as well as potential connections to other 2D condensed matter systems such as 2D Bose-Einstein condensates of spin triplets [84] and superfluid helium films [85]. Further enhancement of the interaction strength can potentially lead to crystallization of the 2D gas [117]. Investigation on the fluctuation and correlation of strongly interacting 2D gases will be reported elsewhere.

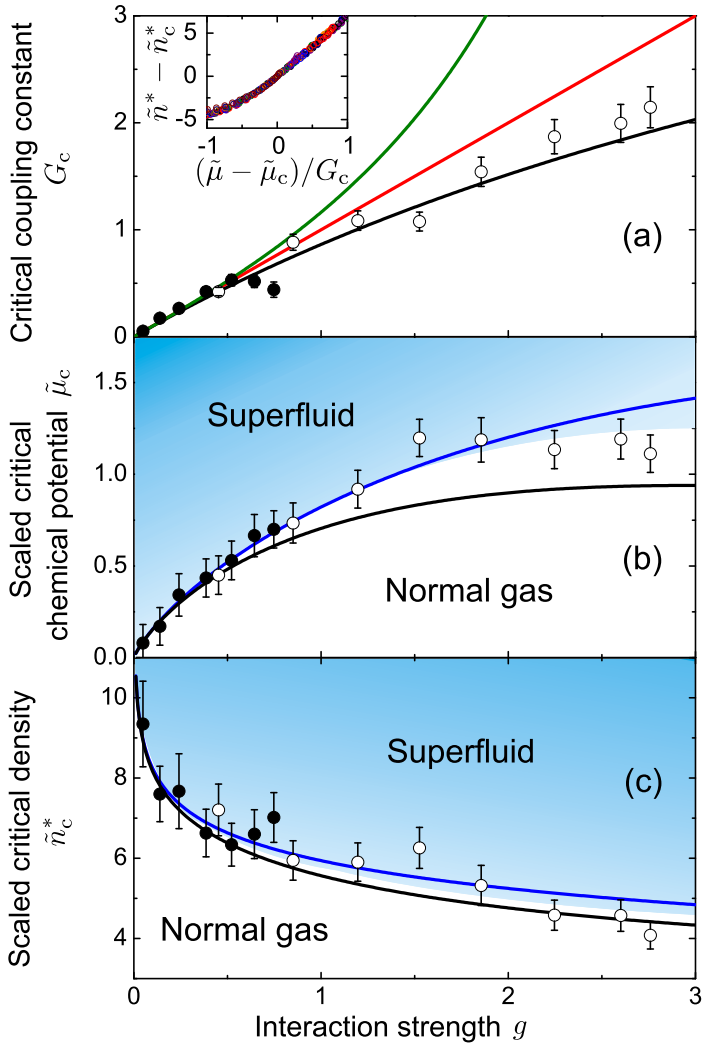

Figure 5.4: By overlapping all scaled equations of state in the transition regime, shown in the panel (a) inset, critical parameters are determined from Eq. (5.2). The results from 2D gases (filled circles) and 2D lattice gases (open circles) are compared to the predictions from the mean-field theory (red line), the perturbation theory [92] (green line), the classical-field theory [71] (blue line), and the Ginzburg-Landau theory [99] (black line).

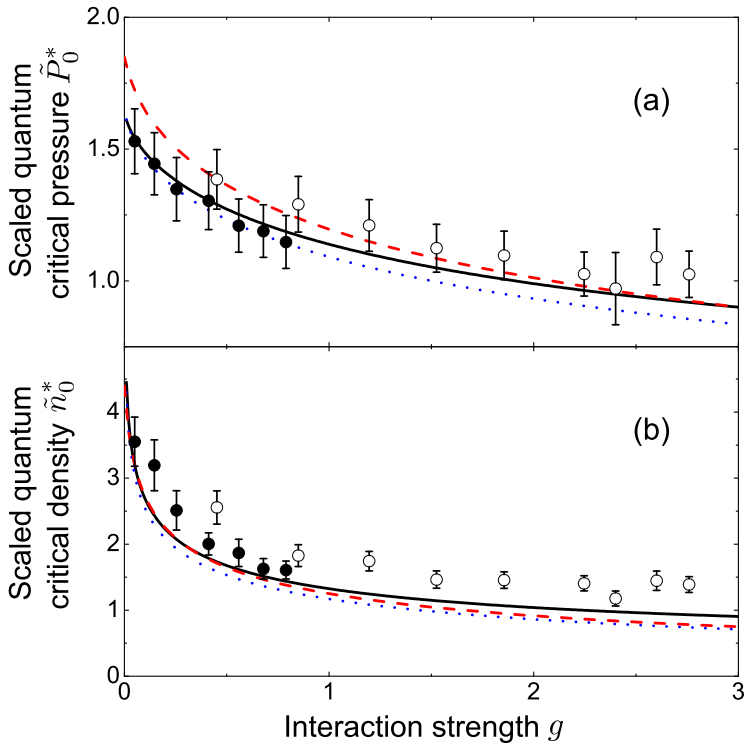

Figure 5.5: The measurements based on 2D gas (filled circles) and 2D lattice gas (open circles) at temperatures between $T = 11 - 15$ nK are compared with NPRG theory [101] (black solid line), mean-field theory for a 2D gas [118] (blue dotted line) and for a 2D lattice gas [119] (red dashed line) at 13 nK.

CHAPTER 6

DIRECT OBSERVATION OF EFFECTIVE FERROMAGNETISM

6.1 Introduction

One of the intriguing properties of quantum many-body systems is the emergence of long-range order from particles with short-range interactions. For example, magnetism, which underlies many digital storage technologies, involves the long-range ordering of electron spins. Systems of ultracold atoms are rapidly emerging as precise and controllable simulators of magnetism and other phenomena. Spinor condensates [120, 121] are a powerful tool in this regard, however, the spin interaction is typically weak and only accessible when multiple atomic internal states are collisionally stable. Here we demonstrate a novel lattice shaking technique to hybridize Bloch bands in optical lattices to introduce a strong effective spin interaction and the formation of large ferromagnetic domains. Our band hybridization method is independent of the atomic internal state, and can be widely applicable to quantum simulators to explore novel magnetic phases in optical lattices with tunable band structure.

In ultracold atomic systems, much effort has focused on reaching conditions where inter-particle interactions are capable of generating long-range ordered phases. Efforts to simulate ferromagnetism using spinor Bose gases [120, 121, 122, 123, 124] have taken advantage of contact and dipole interactions to form domains [121] and spin textures [125, 126, 127]. The resulting magnetic structure can be revealed by spin-dependent imaging techniques. However, the reliance on spin-dependent interactions [128, 129] leads to long characteristic timescales, so that equilibrium can be reached only under limited conditions [130].

An alternative approach is to engineer stronger interactions by coupling atoms to a light field. For example, long-range order has been introduced using cavity photons to mediate interactions [131], and by tilting an optical lattice [132]. With the recent development of more exotic lattices such as hexagonal [133] and kagome [134], as well as occupation of

higher bands [135], complicated band structures are possible where spin can be modeled using band properties rather than internal states. In this work we have developed a lattice shaking and imaging technique, which allows us to form large domains of cold atoms with strong ferromagnetic interactions and to fully map the domain structure. Complicated band structures can also be achieved by dynamically modulating the lattice [55, 56, 41, 136]. Experiments using this technique have created band structures with negative or near-zero tunneling coefficients [56], or with multiple minima at high-symmetry points in the Brillouin zone [41], which has allowed for the simulation of ferromagnetic systems [57]. Double-well dispersions have also been obtained in the continuum by introducing Raman-dressed spin-orbit coupling [137], and proposed to generate spatially ordered phases [138, 139].

6.2 Experiment

Our experiment begins by evaporating and loading a ^{133}Cs BEC into a three dimensional optical dipole trap with trapping frequencies of 8.6, 19.1, and 66.9 Hz in three directions, with the tightest trapping in the direction of gravity and imaging [143]. The atoms are then loaded into a one-dimensional optical lattice at 35° to the in-plane trapping directions, where the final atom number is between 20,000 and 30,000 at a temperature of 7 nK. Our optical lattice is formed by reflecting one of the dipole trap beams back on itself after passing through two oppositely oriented acousto-optic modulators (AOMs). For our experiments we use a laser wavelength λ_L = 1064 nm (lattice spacing 532 nm) and lattice depth V = 7.0 E_R, where $E_R = h^2/2m\lambda_L^2$ is the lattice recoil energy.

After the atoms are loaded into the optical lattice, a sinusoidal shaking is turned on with a linear ramp of between 5 and 100 ms. After the shaking is ramped on, we shake the atoms for 50-100 ms before performing an *in situ* image or extinguishing all lattice and trapping light for a time-of-flight image. When the lattice is removed abruptly for time-of-flight, the atoms in different spin states are projected back to plane waves with different momenta, giving us an effective Stern-Gerlach measurement. Moderate heating is observed during the

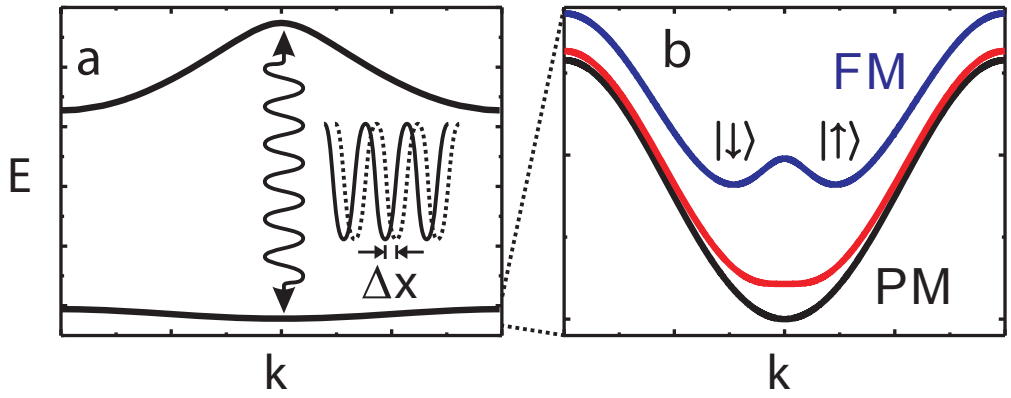

Figure 6.1: **a**, Dispersion $E(k)$ of the first two bands in an optical lattice, hybridized using near-resonant shaking. **b**, Expanded view of the hybridized ground band in the paramagnetic case with no shaking (black), the ferromagnetic case with strong shaking (blue), and the critical case (red).

lattice shaking, resulting in evaporation which leads to a $1/e$ lifetime of 1 s for the particle number. Nonetheless, BEC can be maintained for > 1 s.

The lattice modulation is accomplished by frequency modulating the driving radio frequency (around a carrier of 80 MHz) for the paired AOMs, which changes the relative phase, and therefore the optical path length, between the AOMs. To realize a double-well dispersion, we use a sinusoidal shaking of the optical lattice at a frequency near the ground band to first excited band transition at zero quasi-momentum. This shaking allows the two bands to mix, creating a competition between the positive curvature of the ground band and the negative curvature of the excited band, as shown in Fig. 6.1. Our zero momentum band gap is 5.0 E_R, with an effective mass 2.9 times the bare mass. We apply the shaking at a slightly blue-detuned frequency of 7.3 kHz = 5.5 E_R/h, which gives the least heating when the double-well dispersion is formed. Shaking near the transition allows us to obtain significant hybridization with only a small shaking amplitude, reducing the heating. The solid black curves in Fig. 6.1b show the lowest two bands without shaking in the dressed atom picture. To confirm that the bands will mix to create a double-well potential, we have numerically computed the hybridized Floquet states for several different shaking amplitudes and the results agree well with the experiment.

6.3 Observation of bifurcation

Our experiment is based on a cesium Bose-Einstein condensate (BEC) of 25,000 atoms loaded into a one dimensional optical lattice. Using lattice shaking at a frequency near the ground-to-first-excited transition, we create a hybridized band structure with two distinct energy minima at wavevectors $k = \pm k^*$, with k^* incommensurate to the lattice (see Fig. 6.1. By adjusting the amplitude of the lattice shaking we can tune the dispersion from one with a single minimum to one with two distinct minima. We perform absorption images after time-of-flight (TOF) to determine the momentum distribution; see Fig. 6.1c for sample images. We also average over many shots to create a histogram, shown in Fig. 6.1d. For no shaking up to a shaking amplitude of about 15 nm we observe a single, narrow momentum distribution centered at zero, consistent with a regular BEC. As the shaking amplitude is increased further, we observe a bifurcation and the momentum distribution develops a two-peak structure. Comparing to the calculated position of the minima from numerical diagonalization (white line in Fig. 6.1d), we find good overall agreement despite the fact that the calculations do not include interactions or the effect of the confining potential. In a spin analogy, with momentum playing the role of magnetization, the transition from one to two minima corresponds to a quantum analog of the paramagnetic (PM) to ferromagnetic (FM) transition.

In the ferromagnetic phase, the majority of shots feature all of the atoms in one state or the other, that is, fully magnetized samples. This observation suggests that interactions are important and create a preference for occupation of a single minimum. At length scales greater than $\pi/k^* = 1.5$ μm we can expand around the minima and treat the system as a two-mode BEC, with the minima labeled as spin-up and spin-down. For a uniform system, this yields an effective Hamiltonian,

$$H = \sum_{\sigma=\uparrow,\downarrow} \epsilon_\sigma N_\sigma + \frac{g}{2} N_\uparrow^2 + \frac{g}{2} N_\downarrow^2 + 2g N_\uparrow N_\downarrow, \tag{6.1}$$

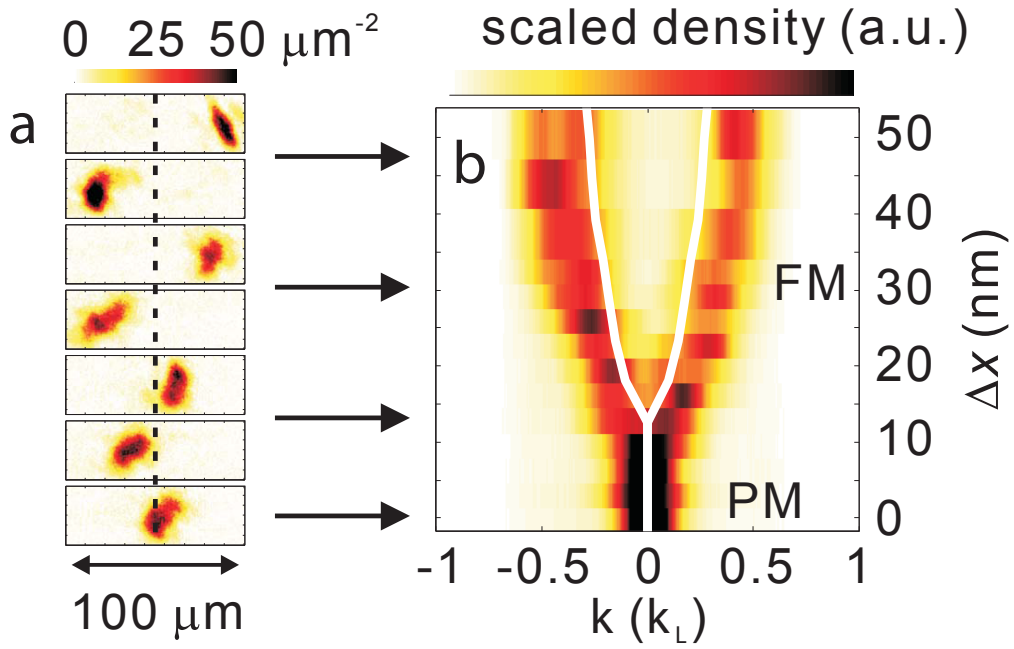

Figure 6.2: **a**, Single shot images (at 30 ms TOF) of ~ 25,000 Cs atoms in the lattice with different shaking amplitudes. **b**, Momentum distribution along the lattice direction as a function of peak-to-peak shaking amplitude Δx, averaged over 10 trials at each amplitude. Imbalances between the two minima are due to statisical uncertainties. The TOF position is used to determine the momentum in lattice units $k_L = 2\pi/\lambda_L$, where $\lambda_L/2 = 532$ nm is the lattice constant. The white line is the calculated location of the dispersion minimum. We ramp on the shaking amplitude linearly over 50 ms followed by an additional 50 ms of constant shaking.

where ϵ_σ represents the single particle energy of each spin state, $N_\uparrow$ ($N_\downarrow$) is the number of up (down) spins, and $g = 4\pi\hbar^2 a/mV$ is the interaction strength in terms of the scattering length a, the mass m, the effective trap volume V, and the Planck constant $h = 2\pi\hbar$. The factor of two in the interspecies interaction arises from inclusion of both Hartree (direct) and Fock (exchange) interactions. The exchange term, unique to systems with atoms in the same internal state, results in a ferromagnetic interaction for positive scattering length $a > 0$. Introducing the collective spin $\vec{J}$ representation [140], we find the Hamiltonian for an easy-axis magnet,

$$H = \frac{\epsilon_\uparrow + \epsilon_\downarrow}{2} N + \frac{3g}{4} N^2 + (\epsilon_\uparrow - \epsilon_\downarrow) J_z - g J_z^2 \tag{6.2}$$

where $J_z = \frac{1}{2}\left(N_\uparrow - N_\downarrow\right)$ is the magnetization, and $N = N_\uparrow + N_\downarrow$ is a constant of motion. Our ferromagnetic interaction derives from the large energy cost to maintain density waves, making it strong and comparable to the interaction between like spins.

6.4 Susceptibility measurement

We investigate the magnetization process by testing its sensitivity to an explicit energy imbalance $(\epsilon_\uparrow - \epsilon_\downarrow)J_z$ [57], see Fig. 6.3. This is realized by providing the condensate a small initial velocity v relative to the lattice that acts as a synthetic field $b = -v = (\epsilon_\uparrow - \epsilon_\downarrow)/2\hbar k^*$. For a ferromagnet the susceptibility will be infinite, and we expect to be able to fully magnetize the sample even for energy imbalance $\epsilon_\uparrow - \epsilon_\downarrow$ much less than our temperature scale or chemical potential. To quantify the sensitivity we assume atoms populate the two spin states according to a Boltzmann distribution with an effective temperature T_{eff}. When the lattice shaking is slowly ramped into the ferromagnetic regime over 100 ms , we find a very sharp transition with an effective temperature of 0.7 nK, well below the actual temperature of 7 nK and chemical potential ~ 20 nK determined from fitting the low density tails of *in-situ* profiles [141]. In terms of susceptibility, the transition is also 8 times sharper than what would be expected in the unshaken case based on the effective mass. When ferromagnetism is ramped on more quickly, the sensitivity is reduced, which is the expected behavior of a quenched ferromagnet. When the scattering length is reduced from 1.9 nm to 1.4 nm via a Feshbach resonance [7], we observe a less sensitive transition, which confirms that spin interactions depend on the scattering length.

6.5 Observation of domain

When a ferromagnet is cooled rapidly in the absence of an external bias field, domain formation is expected. Here we observe that with rapid ramping of the ferromagnetic interaction, domains are formed. When the shaking is weak, the barrier in the dispersion between the

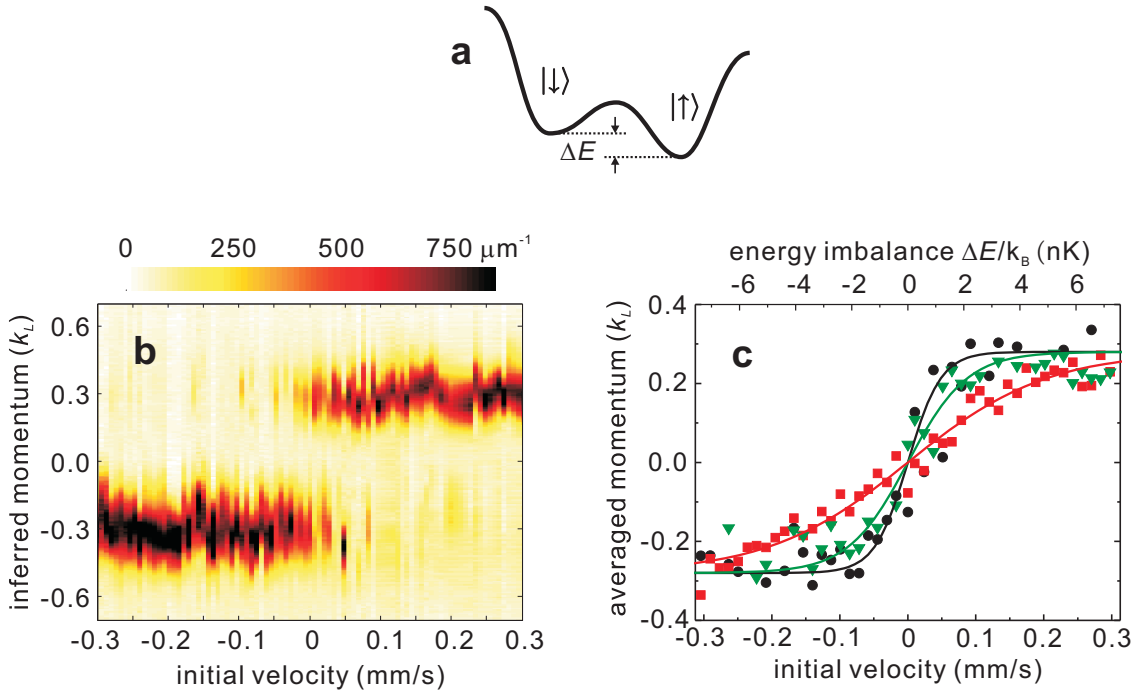

Figure 6.3: **a**, We control the energy imbalance ΔE with a small initial velocity v of the atoms relative to the lattice. For short times the imbalance is given by $\Delta E = 2\hbar k^* v$. **b**, Average density profile along the lattice direction as a function of imbalance with 100 ms ramping time and scattering length a = 1.9 nm. **c**, Average momentum as a function of imbalance under three different conditions: ramping time 100 ms with a = 1.9 nm (filled black circles) or a = 1.4 nm (green triangles), and ramping time 10 ms with a = 1.9 nm (red squares). The solid lines are fits to a thermal distribution, with effective temperatures T_{eff} of 0.7, 1.2, and 2.9 nK. The sample has temperature T = 7 nK and chemical potential $\mu/k_B \approx 20$ nK. Atoms were held at constant shaking amplitude Δx = 32 nm for 100 ms following the ramp.

minima is non-existent or small, and the confining potential (which does not conserve quasi-momentum) can move particles between the minima. Once the shaking amplitude is well above the critical value, the barrier forbids exchange of particles between the two minima, and the total magnetization (i.e. total quasi-momentum) will be conserved. Figure 6.4 shows typical single-domain and multi-domain samples. A detailed reconstruction of the original domain structure can be accomplished by taking advantage of the information in the Bragg peaks. Figure 6.4b shows the relative weight between the main cloud and the lowest two Bragg peaks for single domain samples with known magnetization. Because the atoms are physically oscillating synchronously with the shaking, both wells possess the same averaged

(physical) momentum at any point in the cycle. Therefore the weights between the satellite Bragg peaks must be different in order to compensate for the $2k^*$ difference in momentum of the central peak. Using these weights as a "fingerprint", we can assign to any pixel a fraction of the density as spin-up density and the remainder as spin-down density. To do this we project the vector representing the relative Bragg weights onto the axis distinguishing spin-up from spin-down. Figure 6.4d shows a histogram of projected values. Using these values to identify the spin components allows a complete reconstruction of the original density and magnetization.

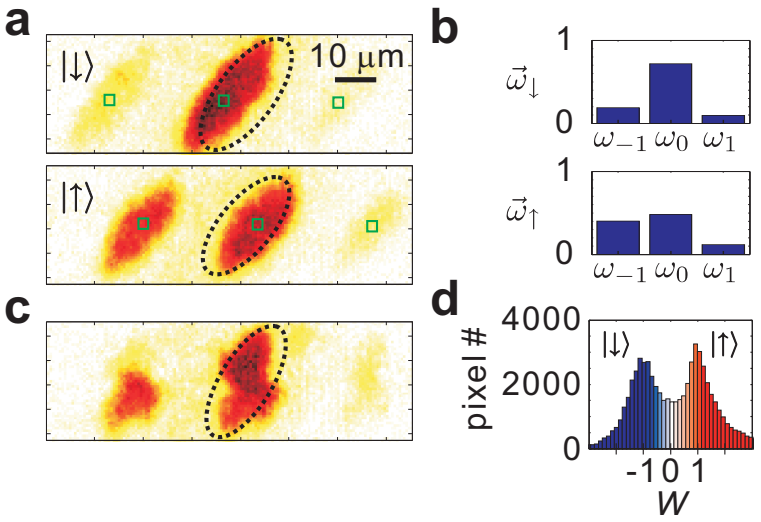

Figure 6.4: **a**, Images at 5 ms TOF for two oppositely oriented single domain samples. **b**, Vectors $\vec{\omega} = (\omega_{-1}, \omega_0, \omega_1)$ signifying relative weights between the -1^{st}, 0^{th}, and 1^{st} order Bragg peaks, corresponding to the regions in **a** identified by boxes. **c**, Image at 5 ms TOF for a two-domain sample. **d**, Histogram (over 19 images) of pixel-wise projection onto $\vec{\omega}_\uparrow - \vec{\omega}_\downarrow$, denoted W. The two peaks indicate the majority of the atoms are either spin-up or spin-down. The dashed circles in **a** and **c** show the position of the samples before TOF.

The reconstruction scheme reveals rich domain structures under different ramping paths, see Fig. 6.8. In the presence of domains, kinetic energy terms in all directions should be added to the Hamiltonian in Eq. (6.2) to describe the spatial pattern. When ferromagnetism is ramped on slowly over 100 ms, we observe larger domains, with boundaries typically oriented in the direction of the short axis of the trap (Fig. 6.7a). When the ramping is done as a quench, over 10 ms, we observe a greater number of smaller domains with less predictable

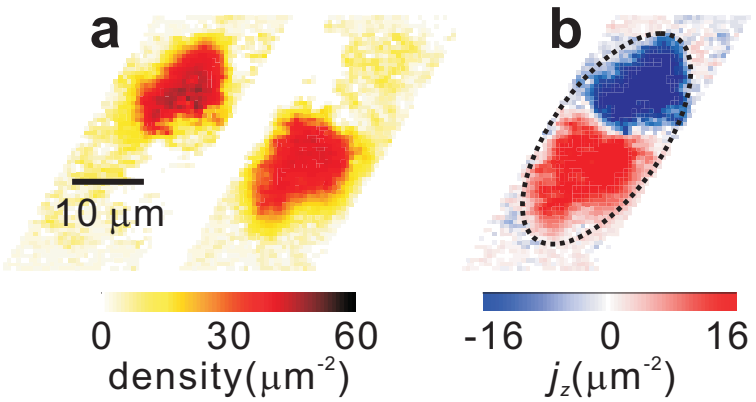

Figure 6.5: **a**, The extracted density of spin-down (left) and spin-up (right) atoms. **b**, The extracted density distribution of magnetization j_z. We ramp on the shaking amplitude over 100 ms followed by an additional 100 ms of constant shaking. The scattering length is 1.9 nm.

orientation (Fig. 6.7b). Our result is consistent with the Kibble-Zurek mechanism in the sense that faster ramps yield shorter range correlations.

6.6 Domain reconstruction

The two peaks of the histogram in Fig. 6.4d are used to define pure spin-up or spin-down, and intermediate values indicate the presence of both spin components. With the spin components isolated, we can adjust for the physical displacement accumulated during the 5 ms TOF due to the momentum $\pm k^*$ and determine the original density and spin distributions, see Fig. 6.5a-b. Our imaging is limited to density and magnetization projections along the imaging axis, however, the sample is much thinner perpendicular to the imaging axis (~ 4 μm), and we expect few domain walls perpendicular to the imaging direction.

In images taken with 5 ms TOF the domain structure is visible in the center of the image, as portions of the cloud move in opposite directions. On either side of the main cloud are higher momentum Bragg peaks induced by the lattice, which has been abruptly turned off along during the expansion. True *in situ* images cannot distinguish the domains, while for longer TOF the shape of the domains is distorted too much during the expansion. To leading order atoms in both spin states respond to the lattice shaking with the same phase, so the

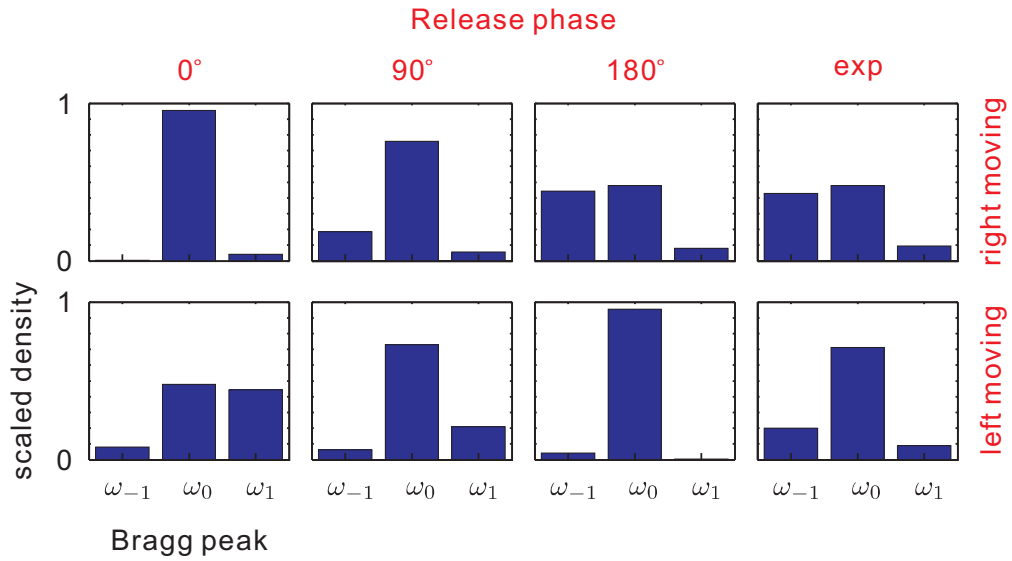

Figure 6.6: Calculated momentum weights at several values of the applied shaking phase, along with the experimentally determined momentum weights. The zero of phase corresponds to maximum rightward velocity.

physical motion (in the lab frame) for either must be the same. If the atoms are released when traveling to the right, the spin-up atoms can have mostly momentum k^*, with only small amounts of higher Bragg peaks at $k^* \pm 4\pi/\lambda_L$. By contrast, spin-down atoms must have a large fraction at $-k^* + 4\pi/\lambda_L$ in order to be physically moving right. Thus, the relative strength of the center and side two Bragg peaks forms a signature that identifies the spin state of each section of the image. Figure 6.6 shows a comparison of the theoretically computed Bragg peak weights with the experimentally determined values. Again we note that the computations include only single particle physics with no confinement. We define a three-dimensional vector which is proportional to the density at each Bragg peak, $\vec{\omega} = (\omega_{-1}, \omega_0, \omega_1)$ (Fig. 6.4). The vector is defined pixel-wise and is normalized to sum to one. Using images which can be identified clearly as fully spin-up or spin-down, we determine typical vectors $\vec{\omega}_\uparrow = (0.43, 0.48, 0.09)$ and $\vec{\omega}_\downarrow = (0.20, 0.71, 0.09)$. Then when analyzing multi-domain images, we compute the population fraction of different components in each pixel by projecting the vector along the $\vec{\omega}_\uparrow - \vec{\omega}_\downarrow$ axis. A histogram of the resulting projection, which we denote as W, is shown in Fig. 6.4. We associate the peaks of this histogram with spin-up and spin-down,

and values in between with fractional population according to the value of W. Values of W beyond the histogram peaks are assumed to be fully magnetized. The vectors $\vec{\omega}$ as well as the histogram peaks depend on the phase of the lattice modulation at the TOF release time, and we calibrate both under different experimental conditions. After determining the pixel-wise spin density of a 5 ms TOF image, we shift each image back by the expected travel distance during the TOF (left or right, depending on spin) and reconstruct the number and magnetization densities at the time of release. In a typical case near the center of our cloud, the experimental uncertainty (from all sources) is 4% of the total density. After projecting onto a unit vector on the $\vec{\omega}_\uparrow - \vec{\omega}_\downarrow$ axis, we scale up by a factor of 4 to get the fraction of spin up. Our magnetization fidelity is given by the resulting uncertainty in spin fraction of 16%. The resolution of magnetization density is set by the depth-of-focus-limited imaging resolution (1.5 μm), and the expansion and distortion of the domains during TOF. The latter may be estimated by $\ddot{R} = \mu/mR$ for short TOFs, where R is the radius of the condensate. For ^{133}Cs in 5 ms this gives $\Delta R = 1.5$ μm, small compared to our cloud size of 10 μm by 20 μm.

6.7 Domain correlation

To quantify difference in domain size and shape, we compute the density-weighted magnetization correlator [121],

$$G(\delta\mathbf{r}) = \frac{\langle \int j_z(\mathbf{r}) j_z(\mathbf{r}+\delta\mathbf{r}) d\mathbf{r} \rangle}{\langle \int n(\mathbf{r}) n(\mathbf{r}+\delta\mathbf{r}) d\mathbf{r} \rangle}, \tag{6.3}$$

where n and j_z denote number and magnetization densities, $\mathbf{r}$ and $\delta\mathbf{r}$ denote position coordinates, and angle brackets denote an average over multiple trials. We distinguish between single and multiple domain samples. For fully polarized domains we expect $G(0) = 1$, however, we obtain $G(0) = 0.6$ for single-domain samples, which can be explained by our $\sim 16\%$ fidelity for state identification. $G(0)$ is even lower for samples with domains due to the

observed domain wall size, which is limited by atom dynamics during the 5 ms TOF. Along the short trap axis, the correlations in samples with slow ramping are both stronger (indicating fewer domain boundaries) and longer range (indicating larger domains) compared with quenched samples. In quenched samples the correlations are roughly isotropic due to the random orientation of domains. In samples with slow ramping and multiple domains, the correlation along the long trap axis drops off abruptly at about 10 μm or 20 lattice spacings, see Fig. 6.8b. Our analysis of $G(r)$ demonstrates that long-range spin correlations can be established, and that domain boundaries prefer to align along the short trap axis when ferromagnetism is turned on slowly. The effective mass along the shaking direction with 32 nm shaking is only 1.1 times the bare mass, making the system nearly isotropic. Therefore the domain orientation is more likely related to minimizing the domain boundary area, and suggests that the system is in a low temperature state. We note that even a rapidly quenched domain structure can quickly relax by exchanging energy with other degrees of freedom, for example kinetic energy in the non-lattice directions.

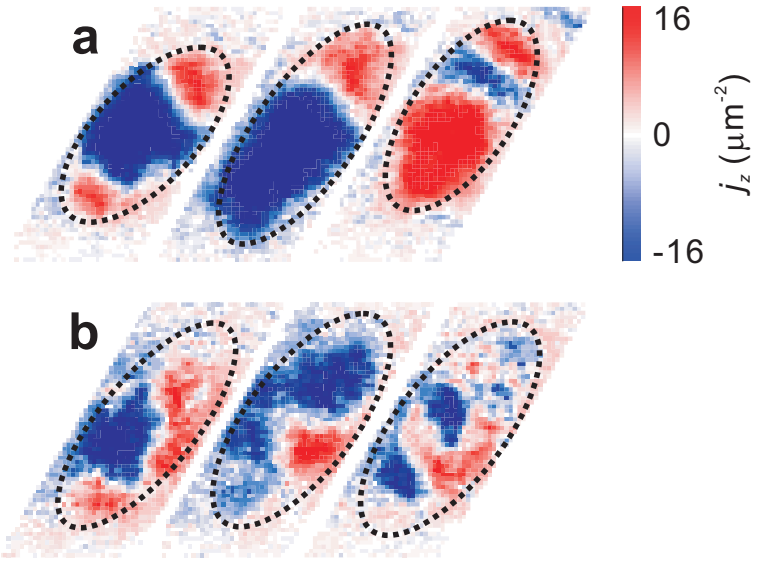

Figure 6.7: **a**, Three representative magnetization images with 100 ms ramping time. **b**, Three representative magnetization images with 10 ms ramping time.

Using lattice shaking to tune band structure has important implications for the simulation of various ordered states in solid systems, where Fermi surface shape and topology can play a

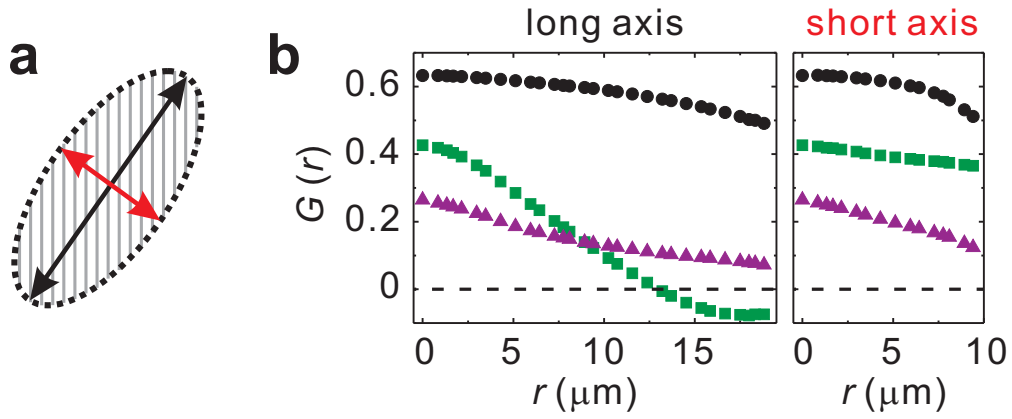

Figure 6.8: **a**, Illustration showing trap geometry and axes. **b**, Density-weighted magnetization correlator $G(r)$ along the long and short trapping directions: The average of 12 single domain samples with 100 ms ramping time (filled black circles), 11 multi-domain samples with 100 ms ramping time (green squares), and 19 multi-domain samples with 10 ms ramping time (purple triangles). Atoms were held at constant shaking amplitude $\Delta x = 32$ nm for 100 ms following the ramp. The scattering length was 1.9 nm.

very important role. The same double well used here would have a nested Fermi surface and be expected to undergo a charge density wave transition [142], for example. Furthermore, the near-resonant shaking technique is easily extendable to two or three dimensions, or other atomic species, which can be fermionic and/or contain multiple accessible internal states. Thus near resonant shaking opens the door to a variety of exciting possibilities for quantum simulation.

6.7.1 Correlation analysis

In the correlation analysis, we distinguish multi-domain samples as those with a nearly equal amount of population in different states. We choose those where the sum of magnetization divided by the sum of density is smaller than 0.275, where 0.5 is the theoretical value for a fully polarized sample. This corresponds roughly to having less than 77.5% of the sample in the same state. For the analysis of fully magnetized sample, we select images with this ratio larger than 0.305, or more than 80.5% in the same state. Although this threshold may seem low, our determination of the magnetization has associated error, and empirically these numbers correctly distinguish the single- and multi-domain cases.

6.8 Effective paramagnetic and ferromagnetic phases

The 1D optical lattice in the z–directon has a lattice depth of $U_0 = 7\ E_R$, the ^{133}Cs atoms at scattering length of 1.4 ~ 1.9 nm in the lattice are well in the superfluid regime. The Hamiltonian of the system is given by

$$H = \sum_{\mathbf{p}} \epsilon_{\mathbf{p}} a^\dagger_{\mathbf{p}} a_{\mathbf{p}} + g \sum_{\mathbf{p}_1,\mathbf{p}_2,\mathbf{p}} a^\dagger_{\mathbf{p}_1+\mathbf{p}} a^\dagger_{\mathbf{p}_2-\mathbf{p}} a_{\mathbf{p}_1} a_{\mathbf{p}_2}, \tag{6.4}$$

where $a^\dagger_{\mathbf{p}}$ is the creation operator of a particle with momentum $\mathbf{p} = (p_x, p_y, p_z)$, $a_{\mathbf{p}}$ is the annihilation operator of a particle with momentum $\mathbf{p}$, $g = 4\pi\hbar^2 a/mV$ is the coupling constant, V is volume of the system, $\epsilon_{\mathbf{p}} = \frac{p_x^2+p_y^2}{2m} + \epsilon(p_z)$ is the kinetic energy, and $\epsilon(p_z)$ is the energy dispersion along the lattice direction.

In the zero or weak modulation regime, the lattice dispersion has one minimum $\epsilon = p_z^2/2m^*$ for low quasi-momenta p_z, where the effective mass $m^* \geq m$ is given by the positive curvature of the ground band at $p_z = 0$ where the condensate resides. In the presence of a weak effective magnetic field $b = -v$, where v is the relative velocity of the atoms to the lattice, the energy minimum is shifted to $p_z = m^* v$. The effective magnetization defined as $\langle p_z \rangle = m^* v$ shows a paramagnetic susceptibility, given by the effective mass m^*. At the critical modulation depth, the band curvature vanishes and the susceptibility diverges. Near this modulation depth, the dispersion can be approximated by $\epsilon = \alpha p_z^2 + \beta p_z^4$, where the parameter α changes sign at the critical modulation depth, and $\beta > 0$. This transition is analogous to the paramagnetic to ferromagnetic transition in Landau theory.

Beyond the critical modulation depth the lowest band develops two minima and at sufficiently low temperatures populations in one or both of the minima $\mathbf{p} = \pm(0, 0, \hbar k^*)$ dominate. The two states are admixtures of the same quasi-momentum states in the ground and the first excited bands. Mixing with higher bands are far off-resonant and thus negligible. Introducing $|\uparrow\rangle = |0, 0, \hbar k^*\rangle$ and $|\downarrow\rangle = |0, 0, -\hbar k^*\rangle$ and neglecting small populations in other

momentum states, we perform the sum in Eq. (6.4) and rewrite the Hamiltonian as

$$H = \sum_{\sigma=\uparrow,\downarrow} \epsilon_\sigma N_\sigma + \frac{g}{2} N_\uparrow^2 + \frac{g}{2} N_\downarrow^2 + 2g N_\uparrow N_\downarrow, \tag{6.5}$$

where $N_\sigma = a_\sigma^\dagger a_\sigma$ is the population in the $|\sigma\rangle$ state and ϵ_σ is the associated kinetic energy. In the presence of a weak effective field $b = -v$, the difference in kinetic energy is $\Delta E = \epsilon_\downarrow - \epsilon_\uparrow = 2\hbar k^* v$ and the effective magnetization $\langle p_z \rangle = \hbar k^*$ for $\Delta E > 0$ and $\langle p_z \rangle = -\hbar k^*$ for $\Delta E < 0$. The large and macroscopic magnetization in the presence of very small external field suggests a ferromagnetic interaction between the two pseudo-spin states. Equation (6.5) and the effective spin Hamiltonian in Eq. (2) further suggest the ferromagnetic interaction is strong, on the same order as the chemical potential and is much larger than in regular spinor condensates.

In the case of a sample with spatial inhomogeneity (i.e. domains), the kinetic energy term can become significant. To include the spatial dependence, we can expand the dispersion about the minima $\pm k^*$ to obtain an effective mass m^o in the lattice direction and m in the other directions. Using the two-component wavefunction $\Psi^\dagger = (\psi_\uparrow^\dagger, \psi_\downarrow^\dagger)$ and Eq. (6.5), we obtain the Hamiltonian

$$H = \frac{\hbar^2}{2m} \nabla_{xy} \Psi^\dagger \nabla_{xy} \Psi + \frac{\hbar^2}{2m^o} \nabla_z \Psi^\dagger \nabla_z \Psi + U(x,y,z) \Psi^\dagger \Psi + \frac{3g}{4} \left| \Psi^\dagger \Psi \right|^2 - \frac{g}{4} \left(\Psi^\dagger \sigma_z \Psi \right)^2, \tag{6.6}$$

where σ_z is a Pauli matrix, and $U(x,y,z)$ is the confining potential of the 3D trap. This Hamiltonian suggests that excitations in all directions can be generated by the spin interaction.

6.8.1 Initial velocity and effective field

To induce an effective energy imbalance we use controlled initial velocity changes by changing the relative beam powers of the trapping beams, which moves the trap center slightly and alters the initial velocity. The initial velocity changes are quantified by observing the change in momentum of a cloud with no lattice shaking during a series of control experiments taken between successive data shots. Over times much shorter than the trapping frequency, the effective energy imbalance of a given initial velocity can be quantified by performing a Galilean transformation to the atomic reference frame. This modifies the dispersion relation $E(k) \rightarrow E(k) - \hbar k v$, where v is the initial velocity. For small v this will split the spin states by $\pm\hbar k^* v$, where $\pm k^*$ corresponds to the positions of the minima. Over longer periods this approximation breaks down, but it remains true that initial velocity breaks the symmetry between the two states and transformation provides an approximate energy scale. In addition to the controlled velocity, there is an uncontrolled component of the initial velocity which changes on long timescales (~5-10 shots), such that several successive shots can be acquired under similar conditions. In order to measure the initial velocity sensitivity as accurately as possible, we have performed several scans under each set of conditions (~40) and adjusted the 50% point of each scan to zero, essentially re-calibrating the total initial velocity every few shots to factor in the slow variations in laboratory conditions. By doing this, we estimate and correct for the slowly varying shifts of the initial velocity, as the data points near the transition midpoint are acquired within a time window shorter than the slow variations. To the extent that the midpoint of the transition is characterized by random statistics of the whole sample, this re-calibration could tend to bias us toward a sharper transition by a small amount proportional to the step size of the bias between shots (~1 nK), because the calibration can reduce some of the true uncertainty about the transition midpoint. However, because the midpoint of the transition involves domain formation, the re-calibration will have a much smaller effect on the transition width, as the region near the midpoint is uniquely identified by simultaneous population of both spin states. To determine the effective

temperature, we assume a Boltzmann distribution, where the average momentum M in terms of initial velocity v would be

$$M(v) = \hbar k^* \tanh\left(\frac{\hbar k^* v}{k_B T_{\text{eff}}}\right). \tag{6.7}$$

6.9 Quench dynamics

To fully investigate the emergence of domains from a single mode condensate, we measure the spatial and momentum distribution of the atoms after a sudden (5 ms) quench across the ferromagnetic transition. Figure 7.5a shows images at various hold times following the quench and for different TOF, revealing that immediately following the quench the atoms have not yet moved appreciably from their original momentum distribution, and are therefore in unstable equilibrium at zero momentum. Over the course of about 10 ms, the atoms displace from this maximum into the minima on either side in a complex and dissipative manner, eventually completely depopulating the zero momentum state, see Fig. 7.5a. Note that this occurs faster than the in-plane trap oscillation periods of 50 and 120 ms. The dissipative dynamics indicate that energy must flow into other degrees of freedom, for example the kinetic energy in the transverse (non-lattice) directions. Observation of fast mixing between the spin and motional degrees of freedom demonstrates that our spin-spin interactions are strong and will drive the system towards equilibrium on short timescales.

Given the quantum nature of our magnetic domains, which are characterized by complex order parameters $e^{ik^*x}\Psi(x)$ and $e^{-ik^*x}\Psi(x)$, where $\Psi(x)$ is the bosonic field operator, we expect spatial interference if they were made to overlap. We do indeed see interference at intermediate hold times for *in situ* and 5 ms TOF images. Figure 7.5b shows the fast Fourier transform of the atomic density averaged over multiple 5 ms TOF images, showing a peak at wavevector $0.27k_L = 0.9k^*$, where $k_L = 2\pi/\lambda_L = 2\pi/1064$ nm is the lattice momentum. This signal, at half the expected wavevector for interference between the two domains, is consistent instead with interference between either domain and the remnant population at

zero momentum. The interference grows in strength as the hold time increases and the system relaxes from the quench, reaching a peak at ~ 10 ms. This supports our interpretation, as at longer times the system nears equilibrium, domains have formed and there is no remnant population at zero momentum. Because our three dimensional condensate is thicker than the depth of focus of the imaging system, we lack the resolution to detect interference at $2k^*$. We also note that the interference is weaker for *in situ* images compared with those taken at 5 ms TOF. This suggests that as the condensate begins to relax toward the two minima, it has already begun to break up in real space to reduce density corrugation. With a time-of-flight image, the domains pass over one and other, allowing us to visualize the quantum inference more clearly.

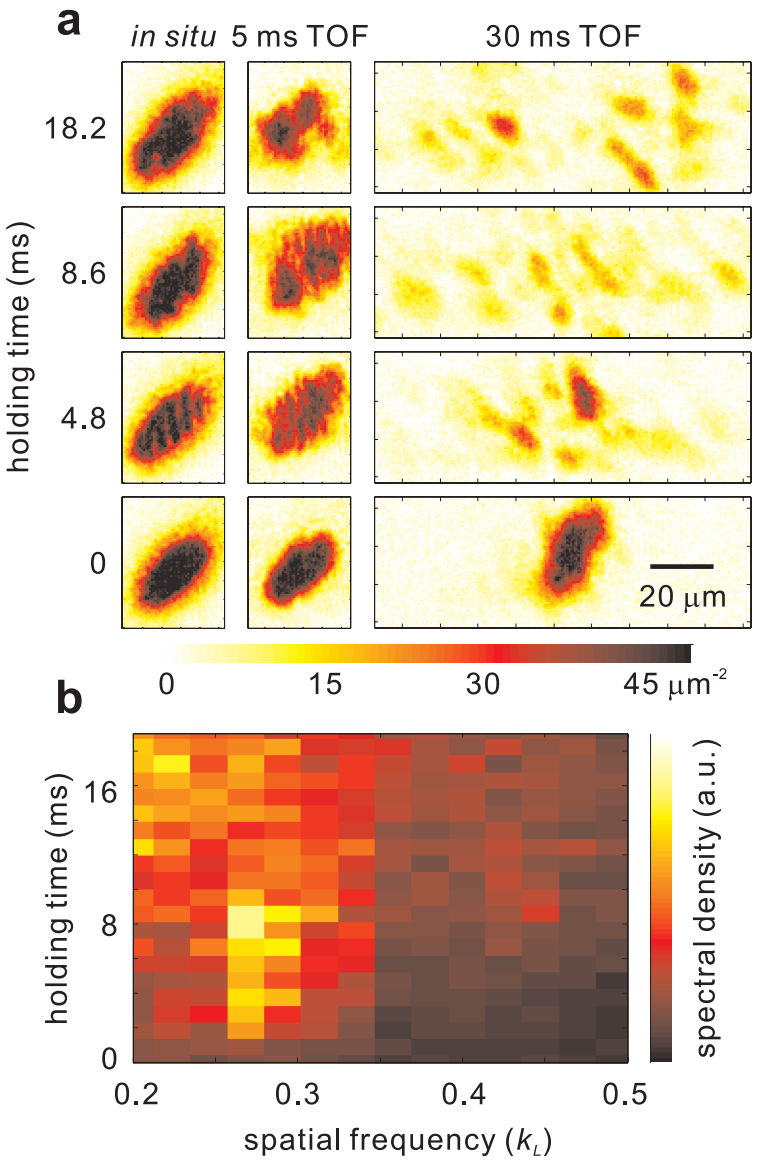

Figure 6.9: **a** Single shot images taken *in situ* and with 5 ms and 30 ms TOF, at several hold times following a 5 ms quench into the ferromagnetic state. **b** Spatial power spectrum along the lattice direction from images with 5 ms TOF, averaged over 20 shots. A peak appears at $k^* = 0.27k_L$ for the first 10 ms. The shaking amplitude was $\Delta x = 32$ nm and the scattering length was 1.9 nm.

CHAPTER 7

ROTON-MAXON EXCITATION SPECTRUM

7.1 Introduction

We present experimental evidence showing that an interacting Bose condensate in a shaken optical lattice develops a roton-maxon excitation spectrum, a feature normally associated with superfluid helium. The roton-maxon feature originates from the double-well dispersion in the shaken lattice, and can be controlled by both the atomic interaction and the lattice modulation amplitude. We determine the excitation spectrum using Bragg spectroscopy and measure the critical velocity by dragging a weak speckle potential through the condensate – both techniques are based on a digital micromirror device. Our dispersion measurements are in good agreement with a modified Bogoliubov model.

In his seminal papers in the 1940s [144, 145], L. D. Landau formulated the theory of superfluid helium-4 (He II) and showed that the energy-momentum relation (dispersion) of He II supports two types of elementary excitations: acoustic phonons and gapped rotons. This dispersion underpins our understanding of superfluidity in helium, and explains many experiments on heat capacity and superfluid critical velocity. What is now called the "roton-maxon" dispersion in He II has been precisely measured in neutron scattering experiments [146, 147] and is generally considered a hallmark of Bose superfluids in the strong interaction regime.

The roton-maxon dispersion carries a number of intriguing features that distinguish excitations in different regimes. The low-lying excitations are acoustic phonons with energy $E = pv_{\mathrm{s}}$, where p is the momentum and v_{s} is the sound speed. At higher momenta, the dispersion exhibits both a local maximum at $p = p_{\mathrm{m}}$ with energy $E = \Delta_{\mathrm{m}}$ and a minimum at $p = p_{\mathrm{r}}$ with energy $E = \Delta_{\mathrm{r}}$. The elementary excitations associated with this maximum and minimum are known as maxons and rotons, respectively. The roton excitations, in particular, are known to reduce the superfluid critical velocity below the sound speed. This is best

understood based on the Landau criterion for superfluidity in which the critical velocity set by the roton minimum $v_c \approx \Delta_r/p_r$ is lower than the sound speed v_s. The roton minimum also suggests the emergence of density wave order [148] and dynamical instability [149].

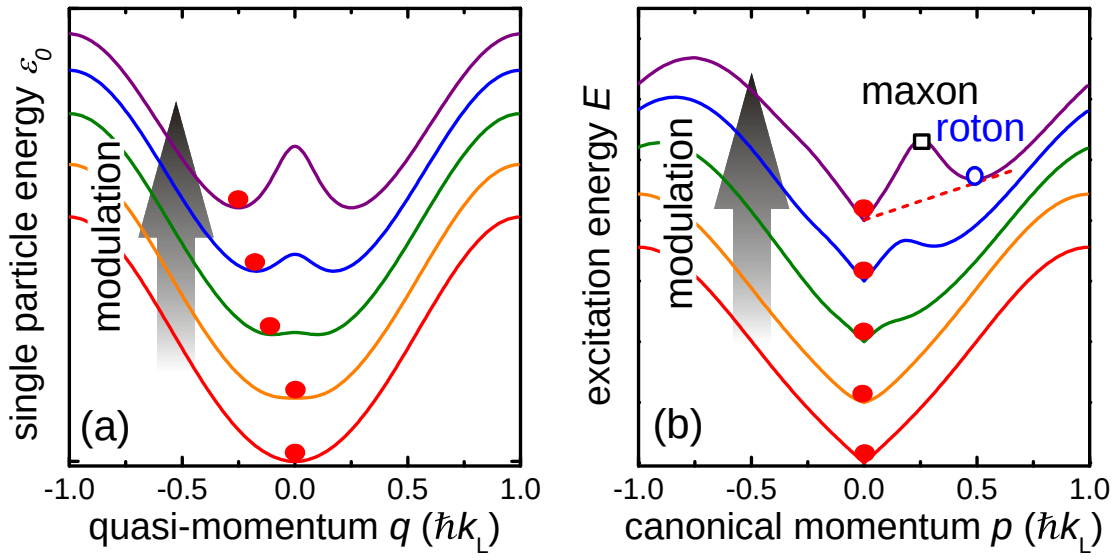

Figure 7.1: (a) For a single atom, the lattice modulation creates a double-well structure above a critical modulation amplitude (top three lines) [161]. In our experiment, the atoms are prepared at the minimum with zero or negative momentum ($q^* \leq 0$, red dot); see text. (b) With atomic interactions, a roton minimum ($\circ$) and a maxon maximum ($\square$) in the excitation spectrum can form. The dashed line indicates the critical velocity limited by the roton minimum according to the Landau criterion for superfluidity. Dispersions are upward offset with increasing modulation amplitude for clarity. The lattice reciprocal momentum is $\hbar k_L = h/\lambda$ where λ is the wavelength of the lattice beams and $h = 2\pi\hbar$ is the Planck constant.

To explore the properties of these unconventional excitations, many theoretical works have proposed schemes for producing the roton-maxon dispersion outside of the He II system. Many proposals have been devoted to atomic systems with long-range or enhanced interactions, e.g. dipolar gases [149, 150, 151], Rydberg-excited condensates [152], or resonantly-interacting gases [153]. Other candidates are 2D Bose gases [154, 155], spinor condensates [156, 157], and spin-orbit coupled condensates [158, 159]. Experimentally, mode softening resulting from cavity-induced interaction has recently been reported [160], which provides strong evidence for an underlying roton-like excitation spectrum.

In this chapter we generate and characterize an asymmetric roton-maxon excitation spectrum based on a Bose-Einstein condensate (BEC) in a one dimensional (1D) shaken optical lattice. We implement Bragg spectroscopy and identify the local maximum and minimum in the dispersion associated with the maxon and roton excitations. Furthermore, by dragging a speckle potential through the BEC we show the reduction of the superfluid critical velocity in the presence of the roton dispersion.

7.2 Modified Bogoliubov Spectrum

The shaken lattice is described by a single particle Hamiltonian

$$H_0 = -\frac{\hbar^2}{2m}\frac{d^2}{dx^2} + V\sin^2\left[k_{\mathrm{L}}\left(x - x_0\left(t\right)\right)\right] \tag{7.1}$$

where m is the mass of a particle, V is the lattice depth and $x_0\left(t\right) = \left(\Delta x/2\right)\sin\left(\omega t\right)$. In what follows we will assume an extended system and ignore the harmonic trapping potential. We use the Trotter expansion to numerically calculate the single particle spectrum $\epsilon_0(q)$ of the time-averaged Hamiltonian [161], see Fig. 7.1(a). We will henceforth work in momentum space and project into the single particle band that is adiabatically connected to the s-band in the limit of no shaking.

$$\hat{H} = \sum_p \left[\tilde{\epsilon}_0\left(p\right) - \mu\right]\hat{a}_p^\dagger\hat{a}_p + \frac{g}{2v}\sum_{q,p_1,p_2}\hat{a}_{p_1+q}^\dagger\hat{a}_{p_2-q}^\dagger\hat{a}_{p_1}\hat{a}_{p_2}, \tag{7.2}$$

where g is the interaction energy, v is the volume of the sample, μ is the chemical potential and we have applied a gauge transformation to shift the dispersion to $\tilde{\epsilon}_0\left(p\right) = \epsilon_0\left(p+q^*\right) - \epsilon_0\left(q^*\right)$. Since the single particle spectrum is asymmetric around the condensate momentum ($p = 0$), the standard Bogoliubov formula does not apply. To calculate the excitation spectrum of the system we assume a condensate at $p = 0$ and replace the annihilation operator with $\hat{a}_0 \to \sqrt{N_0}$, where N_0 is the condensate number. The Bogoliubov Hamiltonian

is found by expanding to second order in the fluctuations around the mean-field $\hat{a}_0$:

$$\hat{H}_{\mathrm{Bog}} = \sum_{p\neq 0}\left[\left(\tilde{\epsilon}_0\left(p\right)+\mu\right)\hat{a}_p^\dagger\hat{a}_p + \frac{\mu}{2}\left(\hat{a}_p^\dagger\hat{a}_{-p}^\dagger + \hat{a}_p\hat{a}_{-p}\right)\right], \tag{7.3}$$

where $\mu = N_0 g/v$ and we have neglected an overall mean-field energy shift of the condensate.

To diagonalize $\hat{H}_{\mathrm{Bog}}$ we define a new set of operators $\hat{b}_p$ and $\hat{b}_{-p}^\dagger$ implicitly through the relations

$$\begin{aligned}\hat{a}_p &= u_p\hat{b}_p + v_p\hat{b}_{-p}^\dagger, \\ \hat{a}_{-p}^\dagger &= u_{-p}\hat{b}_{-p}^\dagger + v_{-p}\hat{b}_p,\end{aligned} \tag{7.4}$$

where we assume u_p, v_p to be real. We require that the Bogoliubov Hamiltonian is diagonal when expressed in terms of the new operators:

$$\hat{H}_{\mathrm{Bog}} = \sum_{p\neq 0} E\left(p\right)\hat{b}_p^\dagger\hat{b}_p, \tag{7.5}$$

and that the new operators additionally satisfy the standard commutation relations: $\left[\hat{b}_p, \hat{b}_{p'}^\dagger\right] = \delta_{pp'}$, $\left[\hat{b}_p, \hat{b}_{p'}\right] = 0$. We then calculate the commutators $\left[\hat{a}_p, \hat{H}_{\mathrm{Bog}}\right]$, $\left[\hat{a}_{-p}^\dagger, \hat{H}_{\mathrm{Bog}}\right]$, $\left[\hat{b}_p, \hat{H}_{\mathrm{Bog}}\right]$, and $\left[\hat{b}_{-p}^\dagger, \hat{H}_{\mathrm{Bog}}\right]$. Imposing the definition of Eq. (7.4), as well as the constraint that commutation relations are preserved, results in a generalized eigenvalue equation [63]

$$\begin{pmatrix}\tilde{\epsilon}_0\left(p\right)+\mu & \mu \\ \mu & \tilde{\epsilon}_0\left(-p\right)+\mu\end{pmatrix}\mathbf{u}\left(p\right) = E\left(p\right)\begin{pmatrix}1 & 0 \\ 0 & -1\end{pmatrix}\mathbf{u}\left(p\right), \tag{7.6}$$

where $\mathbf{u}\left(p\right) = \left(u_p, v_p\right)^T$. Solving the eigenvalue equation gives the Bogoliubov dispersion shown in Eq. 7.19. The finite momentum of the condensate breaks the symmetry in momentum around $p = 0$.

The Bogoliubov transformation coefficients can be found from the generalized eigenvector:

$$\mathbf{u}(p) = \frac{1}{N(p)} \begin{pmatrix} f(p) + \sqrt{f^2(p) - \mu^2} \\ -\mu \end{pmatrix}, \tag{7.7}$$

where $N^2(p) = 2\sqrt{f^2(p) - \mu^2}\left(\sqrt{f^2(p) - \mu^2} + f(p)\right)$ and $f(p) = \bar{\epsilon}(p) + \mu$ normalizes the eigenvector such that $\mathbf{u}^{\mathrm{T}}(p) \begin{pmatrix} 1 & 0 \\ 0 & -1 \end{pmatrix} \mathbf{u}(p) = 1$.

7.2.1 Phonon, maxon, and roton excitations

As discussed in the main text, and shown in Fig. 7.1-7.3, the Bogoliubov spectrum has a linear dispersion near $p/q^* \ll 1$, followed by a maxon at $p = p_m$ and a roton at $p = p_r$. To calculate the phonon velocity we expand the Bogoliubov spectrum for small p. The dispersion near $p = 0$ is

$$E(p) \approx \sqrt{\frac{p^2}{2m^*}\left(\frac{p^2}{2m^*} + 2\mu\right)} \to \sqrt{\frac{\mu}{m^*}}|p| \tag{7.8}$$

with the effective mass

$$m^* = \left(\frac{d^2\tilde{\epsilon}_0(p)}{dp^2}\bigg|_{p=0}\right)^{-1} \tag{7.9}$$

which implies that the phonon velocity is given by $v_s^2 = \mu/m^*$.

Away from $p = 0$, and for sufficiently small $\mu \ll \tilde{\epsilon}_0(p)$, the spectrum can be approximated by expanding in $\mu/\bar{\epsilon}(p)$:

$$E(p) \approx \tilde{\epsilon}_0(p) + \mu + \mathcal{O}\left(\left[\frac{\mu}{\bar{\epsilon}(p)}\right]^2\right). \tag{7.10}$$

This implies that the roton and maxon occur near the single particle minimum and maximum respectively. The roton and maxon quasi-momenta are therefore well approximated by $p_r \approx$

$2|q^*|$ and $p_m \approx |q^*|$, with their energies

$$\Delta_r \approx \mu, \tag{7.11}$$

$$\Delta_m \approx \tilde{\epsilon}_0(-q^*) + \mu, \tag{7.12}$$

respectively. In both cases the spectrum is linear in the chemical potential, or equivalently in $(a/a_0)^{2/5}$, as was found in Fig. 7.3(b) of the main text.

7.2.2 Critical velocity by the Landau criteria

The critical velocity for a superfluid can be found by considering a superfluid moving with velocity v in a reference frame K, simultaneously moving at a velocity v. The energy of the condensate in frame K is $E = E(p)$. We apply a Galilean transformation to a reference frame K' for which the container of the superfluid is at rest. In frame K', the energy of the condensate is $E = E(p) + vp + \frac{1}{2}mv^2$. We see that in the lab frame, the superfluid is only capable of dissipating energy if $E(p) + vp < 0$. Since $E(p)$ is positive, this implies that vp must be negative with $|vp| \geq E(p)$. Furthermore, the critical velocity must occur for the first p that satisfies $|v_c p| = E(p)$. These arguments result in the celebrated Landau criteria:

$$v_c = \min_p \left| \frac{E(p)}{p} \right|, \tag{7.13}$$

where $|E(p)/p|$ is the phase speed of the excitation.

For weak shaking the single particle band structure has a single symmetric minimum at momentum $p = q^* = 0$. Since the spectrum is symmetric in quasimomentum around $q^* = 0$, the Bogoliubov dispersion has the standard form of

$$E(p) = \sqrt{\tilde{\epsilon}_0(p)^2 + 2\mu\tilde{\epsilon}_0(p)}. \tag{7.14}$$

The critical velocity in the symmetric case is found by minimizing the phase speed over all p.

Since there is no roton, the critical velocity is set by the speed of sound at small momenta:

$$v_{c0} = \sqrt{\frac{\mu}{m^*}}. \tag{7.15}$$

As the shaking amplitude increases, the dispersion near this minimum becomes increasingly flat as characterized by $(m^*)^{-1} \to 0$. At the critical shaking above which the double well structure emerges, the quadratic part of this dispersion exactly vanishes and the single particle spectrum is quartic at small p. This implies that $E(p) \propto p^2$ so $E(p)/p \to 0$ as $p \to 0$, and therefore the critical velocity must vanish. This dependence explains the dip in the critical velocity near $\Delta x = 12$nm in Fig. 7.5(b).

Above the critical shaking amplitude the condensate occupies the minimum at $q^* < 0$ and the symmetry of the Bogoliubov spectrum is broken. This asymmetry results in the condensate having two distinct critical velocities in the non-roton and roton directions. The critical velocity in the non-roton direction is set by the phonon velocity, because there is no excitation in that direction with smaller phase speed. This is found by minimizing the phase speed only for negative momenta

$$v_{c-} = v_s = \sqrt{\frac{\mu}{m^*}}. \tag{7.16}$$

In the roton direction, on the other hand, rotons can have a smaller phase speed than phonons. Once again the critical velocity is found by minimizing the phase speed, but now for only positive momenta. This function is minimized numerically to produce the dashed red line in Fig. 7.5(b) above the critical shaking value. For a sufficiently small chemical potential, such that the spectrum away from $p = 0$ is well approximated by Eq. (7.10), we indeed expect the rotons to have a smaller phase speed than the phonons. This implies the critical velocity in the roton direction is well approximated by

$$v_{c+} \approx \left| \frac{\Delta_r}{2q^*} \right|. \tag{7.17}$$

We therefore see that the limit of small chemical potential, the ratio of the two critical velocities is given by

$$\left|\frac{v_{c+}}{v_{c-}}\right| \approx \frac{\Delta_r/2|q^*|}{\sqrt{\mu/m^*}} \approx \frac{1}{\sqrt{8}}\sqrt{\frac{\mu}{q^{*2}/2m^*}}, \tag{7.18}$$

where we have used $\Delta_r \approx \mu$ and $q^{*2}/2m^* \gg \mu$ for experimentally relevant values. Therefore the critical velocity when moving in the roton direction is significantly smaller than the critical velocity in the non-roton direction. This was observed in Fig. 7.5(b).

7.3 Experimental configurations

Our experiment to detect this unusual dispersion starts with an almost pure cesium condensate of $N_0 = 30,000$ atoms loaded into a crossed beam optical dipole trap (wavelength $\lambda = 1064$ nm) with trap frequencies $(\omega_x, \omega_y, \omega_z) = 2\pi \times (9.3, 27, 104)$ Hz [161]. We turn on an additional 1D optical lattice by retro-reflecting one of the dipole trap beams in the $x-y$ plane at 40° with respect to the x-axis. The lattice depth is approximately $V = 7\ E_{\mathrm{R}}$, where $E_{\mathrm{R}} = h \times 1.325$ kHz is the photon recoil energy of the lattice beam.

We create the roton-maxon dispersion by loading a 3D Bose condensate into a 1D shaken (i.e. periodically phase-modulated) optical lattice. The lattice shaking technique has been used previously to engineer novel band structures [55, 56] and to simulate magnetism [41, 161, 162]. Here, we phase modulate the lattice to create a double-well structure in the single-particle dispersion $\epsilon_0(q)$, for which the ground state has a two-fold degeneracy; see Fig. 7.1(a) and Ref. [161]. The lattice potential is phase modulated at 7.3 kHz which is 0.7 kHz blue detuned from the ground to first excited band transition at $q = 0$. The double-well dispersion results from a near resonant coupling between the ground and first excited band through lattice shaking [161], and is a consequence of the parametric instability of a driven anharmonic oscillator [55]. The dispersion with quasimomentum q can be calculated based on a Floquet model [161]. A similar double-well dispersion can also be realized in a spin-orbit coupled system [137, 163, 164, 165, 166].

The double-well dispersion is modified by atomic interactions. We preferentially load the BEC into one of the minima by providing a momentum kick before phase modulating the lattice [161]. We define the direction of the kick as negative, and thus the BEC has a negative momentum $q = q^* < 0$ and the roton minimum is expected at $p = 2|q^*|$; see Fig. 7.1(b). We introduce the canonical momentum $p = q - q^*$ in the reference frame where the condensate has zero momentum and energy. The new dispersion is $\tilde{\epsilon}_0(p) = \epsilon_0(p+q^*) - \epsilon_0(q^*)$. One finds that the dispersion are no longer symmetric due to the existence of the other unoccupied minimum; see Fig. 7.1(b). Based on a modified Bogoliubov calculation (see Refs. [167, 57]), we diagonalize the Hamiltonian to obtain the excitation spectrum:

$$E(p) = \sqrt{\bar{\epsilon}(p)^2 + 2\mu\bar{\epsilon}(p)} + \Delta\epsilon(p), \tag{7.19}$$

where $\bar{\epsilon}(p) = [\tilde{\epsilon}_0(p) + \tilde{\epsilon}_0(-p)]/2$, $\Delta\epsilon(p) = [\tilde{\epsilon}_0(p) - \tilde{\epsilon}_0(-p)]/2$ and μ is the chemical potential. For a system with a double-well structure in $\tilde{\epsilon}_0(p)$, the theory predicts a roton-maxon structure with the roton minimum occuring near $p = -2q^*$; see Fig. 7.1(b). Creation of an "artificial roton" in the dispersion minimum of an analogous spin-orbit coupled system was theoretically proposed in Ref. [158].

7.4 Roton dispersion measurement

To probe the dispersion we perform Bragg spectroscopy [168] by illuminating the atoms with a sinusoidal potential moving along the direction of the shaken lattice. The potential is created from a programmable digital micromirror device (DMD) and a 789 nm laser, which provides a repulsive dipole force. The DMD potential with velocity v and periodicity d (see Fig. 7.2(a) inset) induces a Raman coupling between the condensate with $p = 0$ and finite momentum states with $p = h/d$. When the Raman detuning $E = pv$ matches the energy of the finite momentum state $E(p)$, a resonant transfer will remove atoms from the

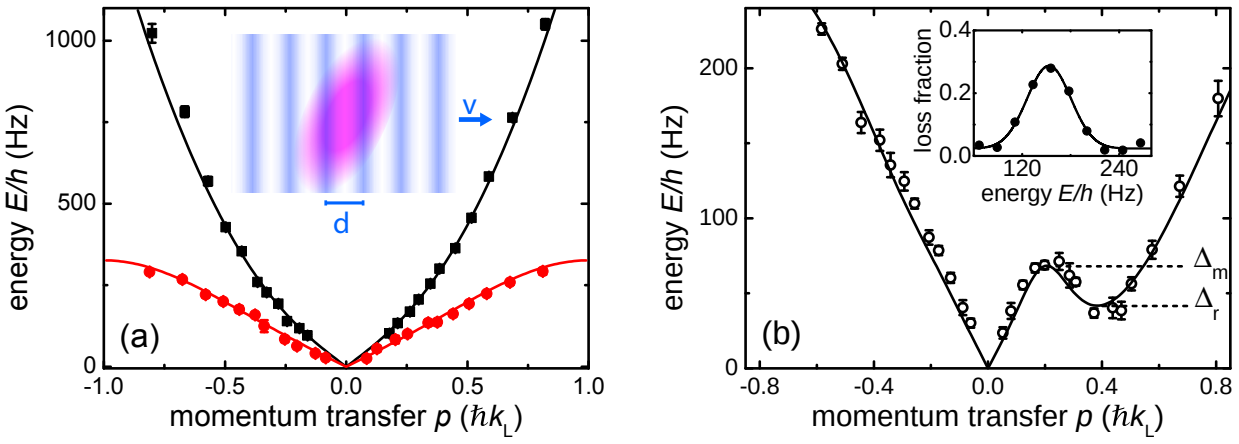

Figure 7.2: (a) We measure the excitation spectra with $N_0 = 30,000$ atoms in a harmonic trap (■) and in a stationary lattice (●) with DMD-based Bragg spectroscopy. The inset illustrates the moving optical potential with velocity v and periodicity d created by the DMD on the BEC (tilted ellipse); see text. The solid lines correspond to the Bogoliubov model with chemical potentials equal to the trap-averaged values. (b) For a BEC with $N_0 = 9,000$ atoms loaded in a shaken optical lattice, we measure the excitation spectrum along the lattice direction. The modulation amplitude (peak-to-peak) is $\Delta x = 33$ nm. The solid line is the best fit based on Eq. 7.19. The inset shows a typical atom loss spectrum taken at $k = -0.38\ k_L$. In both panels, the scattering length is $a = 47\ a_0$.

condensate. We illuminate the atoms with the moving potential for 40 ms and measure the residual condensate particle number after a 30 ms time-of-flight (TOF). The dispersion can be mapped out by finding the energy which gives the strongest reduction of atom number in the condensate for each momentum p.

To test this technique, we compare the dispersions of the BEC in a harmonic trap and that in a $V = 7\ E_R$ unshaken lattice to Bogoliubov calculations; see Fig. 7.2(a). The measurement agrees well with the Bogoliubov spectrum using the measured trap-averaged chemical potentials $\mu = h \times 120$ Hz without the lattice and $\mu = h \times 150$ Hz with the lattice.

We now consider the dispersion of a BEC in a shaken optical lattice, where the roton feature is expected. Here we observe a distinct difference between the excitations at positive versus negative momentum. We work with a modulation amplitude (peak-to-peak) of $\Delta x = 33$ nm which guarantees a strong double-well feature. Fig. 7.2(b) shows the dispersion

measurement, which contains a clear roton-maxon feature at positive momentum (hereafter the roton direction). In contrast, we do not see this feature for negative momentum (hereafter the non-roton direction).

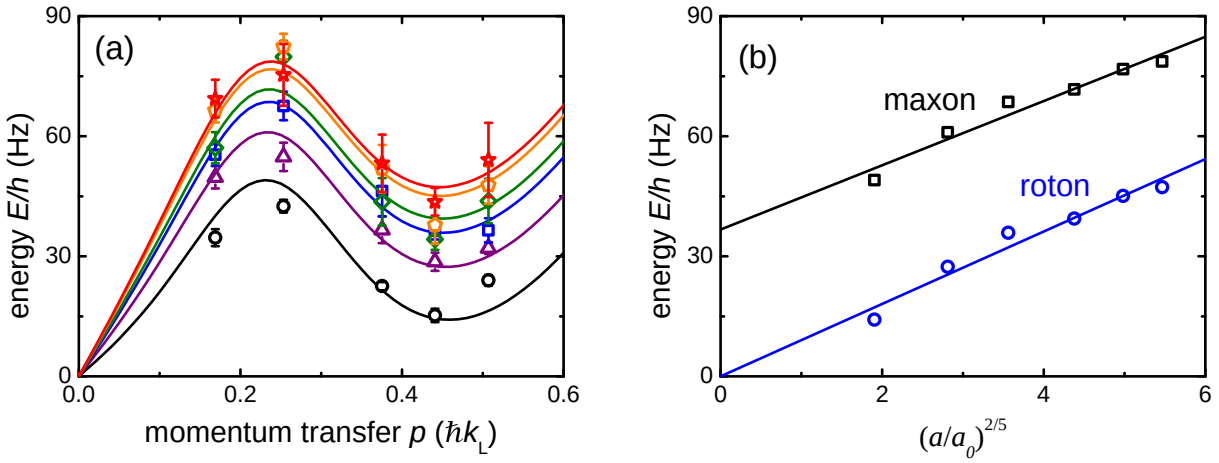

Figure 7.3: (a) We measure the excitation spectra at different scattering lengths a/a_0 = $5(\circ), 13(\triangle), 24(\square), 40(\diamond), 55(\pentagon)$ and $70(\star)$. The condensate number is $N_0 = 9,000$. Solid curves are fits based on Eq. 7.19. A global optimization procedure gives $V = 6.7(2)\ E_{\mathrm{R}}$ and $\Delta x = 43(3)$ nm. (b) Roton energies ($\circ$) and maxon energies ($\square$) extracted from the fits in panel (a) are shown at different scattering lengths. Solid curves are fits based on $\Delta_{\mathrm{r}} = A(a/a_0)^{2/5}$ and $\Delta_{\mathrm{m}} = B + C(a/a_0)^{2/5}$, from which we obtain $A = h \times 9(1)$ Hz, $B = h \times 37(9)$ Hz and $C = h \times 8(1)$ Hz.

We compare the measured roton spectrum with the model in Eq. 7.19. Constraining the model to the experimental parameters only yields qualitative agreement likely due to strong interaction effects [169] which effectively modify the modulation amplitude Δx and lattice depth V. Thus we fit the data with Eq. 7.19 and find the best fit to have $\mu = h \times 58(4)$ Hz, $V = 5.9(1)\ E_{\mathrm{R}}$ and $\Delta x = 49(3)$ nm. The low chemical potential is expected and comes from the lower condensate number as well as the weaker, momentum dependent atomic interactions in the admixed band.

The roton energy is determined by atomic interactions and can be controlled by tuning the scattering length. To demonstrate this we prepare samples with the usual procedure but at a higher scattering length $a = 70\ a_0$ followed by ramping the magnetic field to reach the desired scattering length [7]. We measure the excitation spectrum in the roton direction

with $p > 0$ at 6 different scattering lengths, shown in Fig. 7.3(a).

We adopt a global fit to the data in Fig. 7.3(a) based on Eq. 7.19 to determine the roton energy Δ_{r} and the maxon energy Δ_{m}. Our observation shows that we can experimentally tune the scattering length to vary the roton energy by a factor of 3. Furthermore, we can use scaling arguments to distinguish the behavior of rotons and maxons from the more conventional phonons. For small chemical potentials, the excitation energy for phonons is well-known to scale as $\mu^{1/2}$, while the roton and maxon energies are expected to depend linearly on μ. Furthermore, for an adiabatic ramp of the scattering length, the chemical potential should scale as $\mu = n_0 g \propto a^{2/5}$ where $g \propto a$ is the interaction strength, and the condensate density in the harmonic trap is $n_0 \propto a^{-3/5}$ [63]. Therefore, we plot the extracted roton and maxon energies as a function of $a^{2/5}$ as a proxy for chemical potential; see Fig. 7.3(b). The observed linear dependence confirms the expected scaling for rotons and maxons.

7.5 Critical velocity measurement

To measure the critical velocity of the condensate, we move a speckle pattern through the atomic sample as shown in Fig. 7.4 and determine the minimum velocity required to heat the cloud. Heating is detected using the method shown in Fig. 4.17. The speckle pattern is generated on the DMD and directly projected onto the atoms with no beam selection mask in between. However, we do use a digital mask to ensure that we apply the speckle only to the region of high chemical potential, see Fig. 7.4(a). We create a speckle pattern by randomly turning on or off 4×4 sections of micromirrors instead of individual mirrors. Each section still corresponds to an area smaller than our resolution limit but wastes less laser power into large-angle diffracted peaks that cannot be collected by our projection optics. In principle this speckle pattern should excite the gas at a broad range of wavevectors, limited on the low end by the finite size of the condensate to approximately $k_{\mathrm{min}} = 2\pi/20\mu m \approx 0.05\ k_{\mathrm{L}}$ and limited on the high end by the resolution to approximately $k_{\mathrm{max}} \approx 0.55\ k_{\mathrm{L}}$.

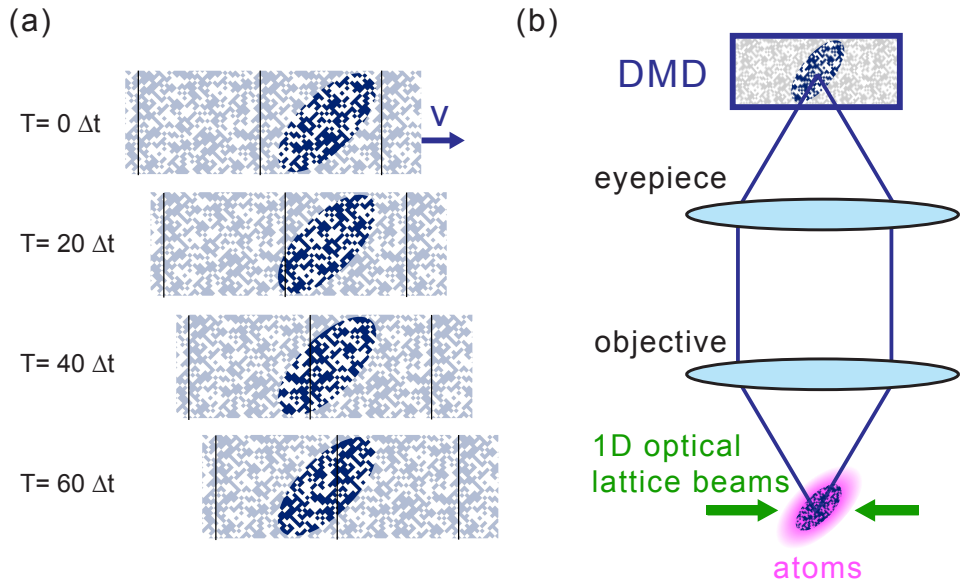

Figure 7.4: (a) For critical velocity measurements a digital speckle pattern (light gray) moves at a steady speed v across the atomic sample, but is digitally cropped with the DMD to illuminate only the central region of the sample (dark blue). We show the pattern at four different elapsed times $T = N \times \Delta t$ after the DMD has been triggered N times, where Δt is the delay between triggers. The thin vertical lines show the spatial period of the patterns. (b) Critical velocity measurements do not require a beam selection mask. We directly project the real space speckle pattern onto the atomic sample.

To move the speckle we trigger the DMD to switch to a different pattern with the same speckle but shifted by 0.3 μm in the plane of the atomic sample. The triggering rate $f = 1/\Delta t$ determines the speckle velocity $v = f \times 0.3$ μm. Because the DMD can only store up to 96 patterns, the speckle pattern is forced to repeat after 96×0.3 μm$= 29\mu$m which is larger than the width of a sample.

One significant consequence of the roton dispersion is the suppressed superfluid critical velocity v_c. We measure the critical velocity of the BEC loaded into the shaken lattice by projecting a moving speckle pattern using the DMD. Instead of using a single laser beam [171, 172, 76] or a lattice with a definite spatial frequency [170], our speckle pattern contains a broad spectrum of wavenumbers up to the resolution ($k \approx 0.55\ k_L$) of our projection system. Furthermore, the potential remains locally perturbative ($\approx h \times 1.1$ Hz) to prevent vortex proliferation [174, 175, 173]. When the velocity of the speckle pattern reaches or exceeds

the critical velocity, atoms are excited from the condensate. To prevent excitation in the low density tail [170], we digitally mask out the region of the speckle pattern which could overlap with the edge of the cloud.

We observe a clear threshold in speckle velocity above which the condensate number decreases; see Fig. 7.5(a). The experimental sequence is similar to that used for Bragg spectroscopy: we illuminate the cloud with a moving speckle pattern for 100 ms followed by a 30 ms TOF. To find the critical velocity, we fit the remaining condensate number with a constant value intersecting a linear decay. The intersection point determines the critical velocity v_c. Above a critical value, we observe the condensate fraction decreases linearly with the speckle velocity. This is consistent with a previous observation of the critical velocity in a Bose superfluid [170], along with a recent calculation [176].

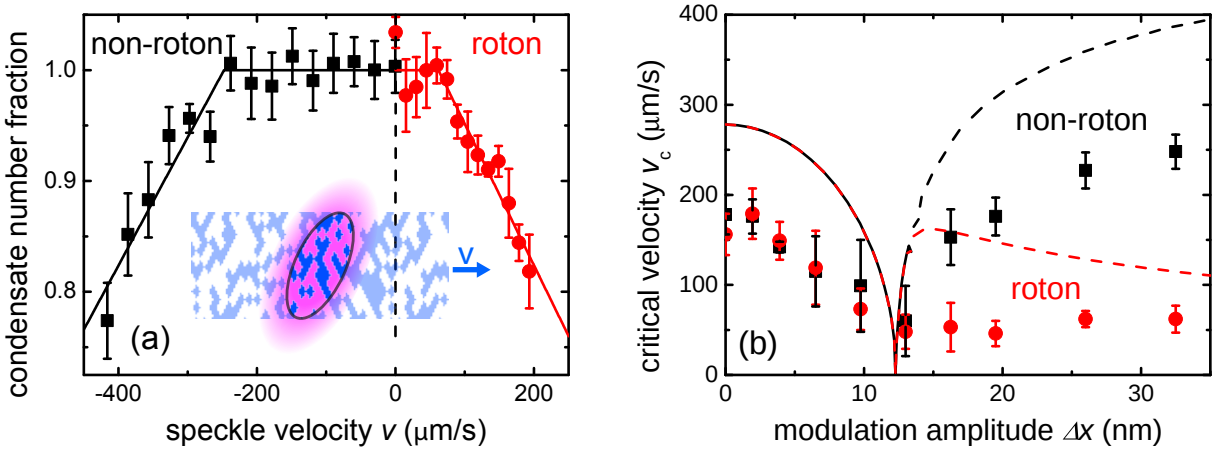

Figure 7.5: (a) We measure the residual condensate number fraction after dragging a speckle pattern through the center of the cloud at different velocities v along the roton direction ($p > 0$, solid dots) and the non-roton direction ($p < 0$, solid squares). The solid lines are fits used to determine the critical velocity. The inset illustrates the experimental scheme; see text. (b) Critical velocities as a function of modulation amplitude are shown. Above the critical modulation amplitude $\Delta x > 12$ nm, the critical velocity is significantly lower in the roton direction. Our measurement is compared with the critical velocity calculated from Eq. 7.19 using Landau criterion (dashed lines). In both panels, the scattering length is $a = 47\ a_0$ and the initial condensate number is $N_0 = 9,000$.

In order to understand the emergence of the roton-maxon dispersion, we measure critical

velocity in both the roton direction $p > 0$ and the non-roton direction $p < 0$ with increasing modulation amplitude Δx; see Fig. 7.5(b). In order to maintain similar chemical potential, we prepare the samples with a large $\Delta x = 33$ nm and slowly ramp Δx to the desired value. For small final $\Delta x < 12$ nm, v_c is the same in both directions and decreases as we approach the critical value $\Delta x_c \approx 12$ nm (phonon mode softening). When the gas enters the ferromagnetic phase ($\Delta x > 12$ nm) [161], v_c increases immediately along the non-roton direction, while in the roton direction v_c remains small.

We compare the measurement with the critical velocity based on the Landau criterion $v_L = \min|E(p)/p|$. As the experiment conditions closely resemble those in Fig. 7.2(b), we evaluate the critical velocity with $\mu = h \times 58$ Hz, $V = 5.9\ E_R$ and Δx scaled by 1.5, the parameters which best fit that dispersion measurement. The calculated v_L, shown as dashed lines in Fig. 7.5(b), displays a disparity between the roton and non-roton directions for $\Delta x >$ 15 nm, in agreement with our observation. Our critical velocities, however, are significantly lower than v_L. In early BEC experiments [171, 172], low critical velocities were observed and explained by the large obstacles that disrupt the superflow and spin off vortices [174, 175, 173]. In our experiment with weak speckle potential, a likely scenario is that the critical velocity is limited by excitations generated in the low density regions above and below the cloud along the DMD projection axis.

In conclusion, we observe a roton-maxon dispersion of a BEC in a shaken 1D optical lattice based on three pieces of evidence: the many-body excitation spectrum, the dependence of the excitation energies on the atomic interactions, and the superfluid critical velocity measurement. Our results agree well with the Bogoliubov calculation and suggest the roton/maxon excitations are distinct from acoustic phonons. Our experiment demonstrates that shaken optical lattices are a convenient platform to generate new types of quasi-particles in a dilute atomic gas, allowing future study on their dynamics, stability, and interactions. For instance, knowing the quasiparticle dispersion should allow a future experiment to create macroscopic numbers of rotons, leading to possible roton condensation [176, 177], and

separation of the rotons into domains. In-situ imaging would allow direct observation of the temporal evolution of such states.

CHAPTER 8

OUTLOOK

The main part of the thesis is about engineering atomic dispersion with a shaken optical lattice. Through creating a double-well dispersion, we observe effective ferromagnetism and ferromagnetic domains. We further investigate the excitation spectrum in a single domain. The many-body interaction lifts the degeneracy between the two wells and lead to a roton-maxon excitation spectrum. To continue investigating the physics in a double-well dispersive system, we propose performing *in situ* measurements of roton density order. We expect intrinsic roton excitation happening due to the thermal equilibrium in the system. We will introduce the experimental design and some preliminary results.

8.1 Density order in a shaken optical lattice

Despite the roton excitation spectrum in the superfluid helium system was predict in 1947 by Landau, the mechanism of roton formation is still under debate. Landau believes that the excitations represent a certain kind of rotation of the fluid, so it gets the name "rotons". Feynman later relates roton to local vorticity of the superfluid. Noziéres, instead, argued that it should be the superfluid helium in the proximity of crystallization which gives a natural density wave mode [178]. The notions between rotating fluid and density wave are qualitatively different. Nevertheless, it remains difficult to probe the density order in the superfluid helium system due to the limitation of the probe for resolving the microscopic physics in the system. An ultracold atomic system, however, allows *in situ* imaging technique for direct probing. In combination with the tunability of roton momentum, we are in a good position to probe the roton density order.

There has been numerous investigations on intrinsic density order in ultracold atoms, including crystallization of vortex lattice which is protected by the topology of the excitation has been predicted and observed [38]. A soliton train is also protected by the phase difference

between individual solitons. Recently, Kadau *et al.* observe Rosensweig instability and find condensate droplet in three-dimensions [179]. In our system, roton density order resembles matter wave interference. Unlike what has been observed that two wave packets pass through each other, the roton density order can remain present due to its zero group velocity given by the dispersion.

8.1.1 Structure factor and susceptibility in the 2D gas

The quantum phase of a given system is characterized by the order parameter and its correlation function. The density structure factor $S(k)$ represents the Fourier transform of the density-density correlation function $S(k) = \int dr e^{-ikr}\nu(r)$, where $\nu(\mathbf{r'}) = \bar{n}^{-1}\langle\delta n(\mathbf{r})\delta n(\mathbf{r}+\mathbf{r'})\rangle$ calculates the density-density correlation. At thermal equilibrium, $S(k)$ in the BEC is related to the excitation spectrum $\epsilon(k)$ in the following way:

$$S(k) = \frac{\hbar^2 k^2}{2m\epsilon(k)} \coth \frac{\epsilon(k)}{2k_B T}. \tag{8.1}$$

Based on the above equation, we calculate the structure factor from the roton excitation spectrum given by the Floquet model. Given the limitation from the imaging resolution (k_{cutoff} = 0.63 k_L), we optimize the shaking parameters to make the roton correlation prominent. We use a 4 E_R lattice to maximize the contrast between roton and maxon in the structure factor. At a shaking frequency of 6.2 kHz, we now have a critical shaking amplitude of Δx_c ~5 nm. When operating at a shaking amplitude of Δx = 39 nm, the roton momentum locates at $2k^*$ = 0.30 k_L which can be observed in our system.

To get a larger area for analysis and a higher resolution in the momentum space, we deliberately use a weaker confinement in the experiment. We analyze the central 20-by-40 pixels of the cloud and find a distinct difference between structure factors in two directions. In the lattice direction, we find dramatic enhancement of correlation at $2k^*$ in the structure factor analysis. While the orthogonal direction shows monotonic decay at a large wavevector.

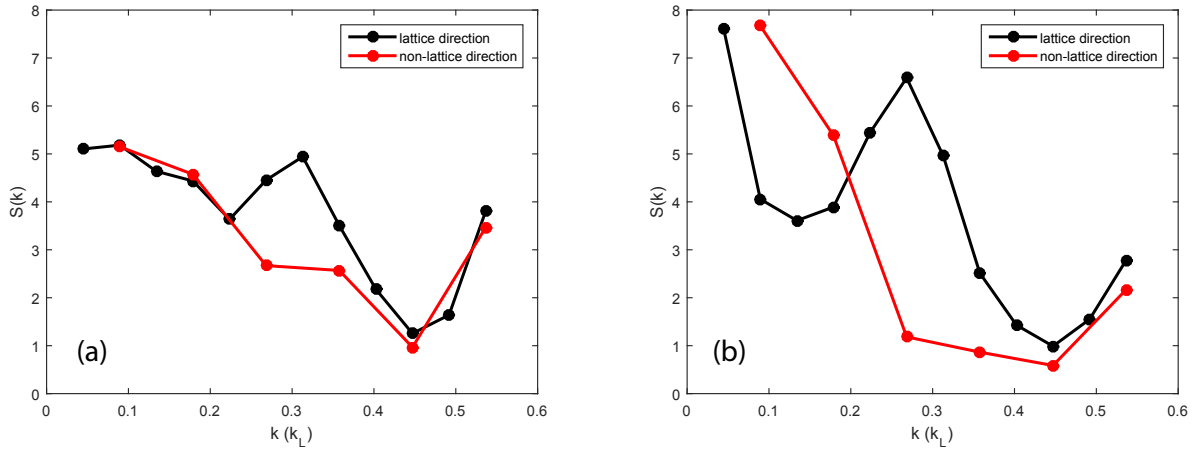

Figure 8.1: We compare structure factors measured in two different scattering length. In the individual measurement, we compare the results analyzed along different directions. In the lattice direction, the signal is significantly enhanced. The left figure shows measurement performed with a scattering length of 52 a_0 while the right one is done at 19 a_0. In the 19 a_0 experiment, the corresponding roton energy is lower. Thus the excitation and density-density correlation becomes stronger. The MTF of the imaging system is highly suppressed at a large wavevector, and the signal at the highest wavevector is less reliable.

As was mentioned in the earlier chapter, the roton energy depends on the chemical potential of the system. The structure factor, however, depends on the excitation energy exponentially. We compare the structure factors measured at different scattering length and confirm an enhanced signal at a smaller scattering length.

In the proximity of the critical point, we assume that the quadratic term scales with the shaking amplitude linearly while the quartic term remains the same. The roton momentum would then scale with the shaking amplitude as $p* \sim (\Delta x - \Delta x_c)^{1/2}$. To confirm this, we perform measurements of the structure factors at different shaking amplitude and compare the result with the theoretical prediction. We find good agreement as shown in Fig.8.2.

To further characterize the property of the roton, we measure the susceptibility of the gas at different shaking amplitudes. We apply an additional lattice potential generated from the DMD and measure the contrast of the density corrugation. A higher contrast suggests that the cloud is more susceptible to the wavelength of the additional lattice. Given the low kinetic energy of the roton excitation, the cloud shows enhanced susceptibility at $2k*$. The

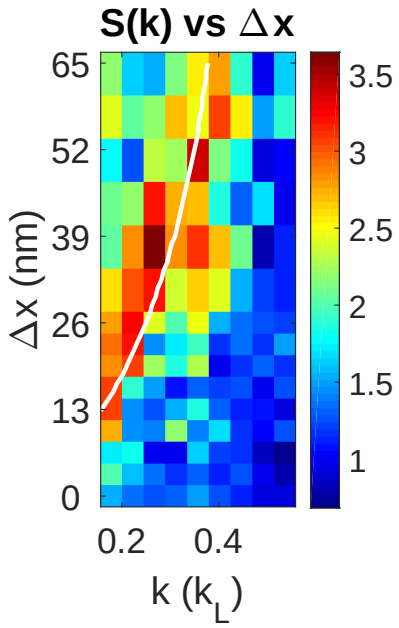

Figure 8.2: S(k) dependence on the Δx.

experimental measurement is compared with theoretical prediction in Fig.8.3.

The above mentioned observations are consistent with our expectation that thermal excitation can lead to roton population in the atomic cloud. However, we find further evidence that could rule out our hypothesis. When the cloud is biased to one of the well, the density order can hardly be observed. It suggests that thermal excitation might not be the main reason for the density order. Instead, the excitation of the roton could be originated from the excitation in the preparation. In the next section, we switch to a three-dimensional system which has a much smaller heating compared to the two-dimensional system.

8.1.2 Density order in the 3D gas

The technical difficulty of probing density order in a 3D gas is the limited sensitivity on the high optical density. When the probe beam intensity is too weak, the optical density could be saturated and sensitive to the photon shot noise. To mitigate the effect, we use a detuned image beam (δ = 6.7 MHz).

Using a detuned imaging beam, we also modify the modulation transfer function (MTF).

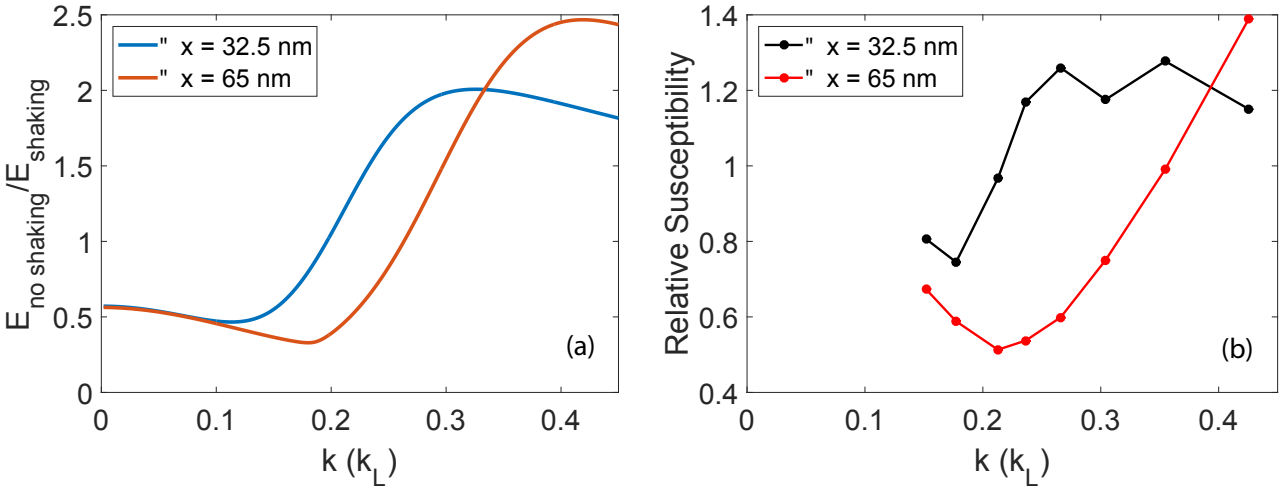

Figure 8.3: (a) shows the normalized susceptibility to non-shaking experiment at different shaking amplitude. The calculation is based on the theoretical dispersion relation and Gross-Pitaevskii equation. The density susceptibility of the gas to an external potential depends on the wavevector. (b) We illuminate atoms with an additional lattice potential created by the DMD. With a fixed lattice intensity, we compare the density corrugation amplitudes at different lattice shaking amplitudes.

The dispersive effect from the off-resonant imaging alters the overall phase difference between the scattered field and the incident field. The phase shift changes the point spread function and consequently the MTF significantly, see Chap.4. In the new configuration, we enhance the imaging sensitivity at the roton momentum.

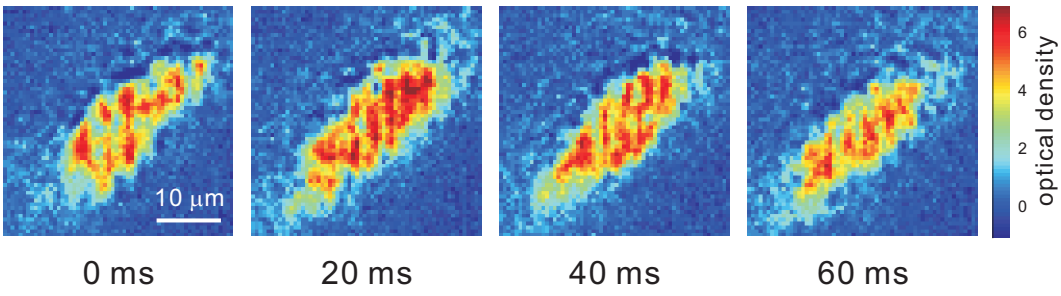

Figure 8.4: *In situ* measurement of the roton density order.

To quantitatively measure the strength of the density order, we analyze the Fourier power spectrum, see Fig.8.5(a). The spectrum shows the difference between a shaken experiment and an unshaken experiment. The signal given by the difference is contributed from the roton with the background noise being subtracted. To estimate the lifetime, we show the integrated

signal between 0.2 and 0.4 k_L in Fig.8.5(b), and a clear signal of long-lived density order is observed. The lattice depth is 5 E_R, the shaking frequency is 6.5 kHz, and the shaking amplitude is 26 nm.

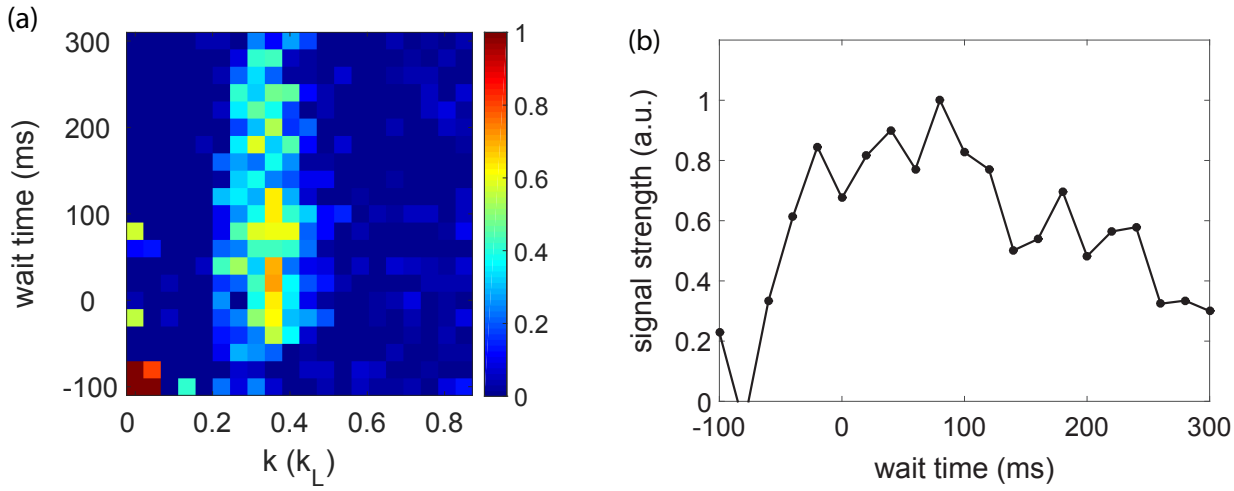

Figure 8.5: Roton density order lifetime. (a) shows the enhancement of density corrugation from lattice shaking. (b) integrates the Fourier space between 0.2 and 0.4 k_L and plot out the temporal evolution.

One interesting feature is the long coherence length of the density order. Among the whole cloud, the phase of the density order remains constant. In our earlier observation [161], we found formation of effective ferromagnetic domains due to the unstable nature of the density order. It's unclear how the density wave and the domain coexist or compete with each other. Further investigation on the domain existence and its effect remain interesting.

REFERENCES

[1] M. H. Anderson, J. R. Ensher, M. R. Matthews, C. E. Wieman, and E. A. Cornell. Obervation of Bose-Einstein condensation in a dilute atomic vapor. *Science*, **269**, 198, (1995).

[2] K. B. Davis, M.-O. Mewes, M. R. Andrews, N. J. van Druten, D. S. Durfee, D. M. Kurn, and W. Ketterle. Bose-Einstein condensation in a gas of sodium atoms, *Phys. Rev. Lett.*, **75**, 3969, (1995).

[3] D. S. Jin, M. R. Matthews, J. R. Ensher, C. E. Wieman, and E. A. Cornell, Temperature-Dependent Damping and Frequency Shifts in Collective Excitations of a Dilute Bose-Einstein Condensate, *Phys. Rev. Lett.*, **78**, 764, (1997).

[4] D. M. Stamper-Kurn, H.-J. Miesner, S. Inouye, M. R. Andrews, and W. Ketterle, Collisionless and Hydrodynamic Excitations of a Bose-Einstein Condensate, *Phys. Rev. Lett.*, **81**, 500, (1998).

[5] J. Stenger, S. Inouye, A. P. Chikkatur, D. M. Stamper-Kurn, D. E. Pritchard, and W. Ketterle, Bragg Spectroscopy of a Bose-Einstein Condensate, *Phys. Rev. Lett.*, **82**, 4569, (1999).

[6] D. M. Stamper-Kurn, A. P. Chikkatur, A. Grlitz, S. Inouye, S. Gupta, D. E. Pritchard, and W. Ketterle, Excitation of Phonons in a Bose-Einstein Condensate by Light Scattering, *Phys. Rev. Lett.*, **83**, 2876, (1999).

[7] C. Chin, R. Grimm, P. Julienne, and E. Tiesinga, Feshbach resonances in ultracold gases. *Rev. Mod. Phys.* **82**, 1225 (2010).

[8] E. A. Donley, N. R. Claussen, S. L. Cornish, J. L. Roberts, E. A. Cornell and C. E. Wieman, *Nature* **412**, 295 (2001).

[9] L. Khaykovich *et al.*, *Science* **296**, 1290 (2002).

[10] K. E. Strecker, G. B. Partridge, A. G. Truscott, and R. G. Hulet, Formation and propagation of matter-wave soliton trains, *Nature* **417**, 150 (2002).

[11] H. J. Lewandowski, D. M. Harber, D. L. Whitaker, and E. A. Cornell, Simplified System for Creating a Bose-Einstein Condensate, *J. Low Temp. Phys.* **132**, 309 (2003)

[12] http://www.strontiumbec.com/

[13] I. Bloch, J. Dalibard, and W. Zwerger, Many-body physics with ultracold gases, *Rev. Mod. Phys.* **80**, 885 (2008).

[14] J. P. Brantut, J. Meineke, D. Stadler, S. Krinner, T. Esslinger, Conduction of ultracold fermions through a mesoscopic channel, *Science* **337**, 1069 (2012).

[15] S. Krinner, D. Stadler, D. Husmann, Jean-Philippe Brantut, and Tilman Esslinger, Observation of quantized conductance in neutral matter, *Nature* **517**, 64 (2015).

[16] R. P. Feynman., Simulating Physics with Computers, *Int. J. Theor. Phys.* **21**, 467 (1982).

[17] T. W. B. Kibble, Topology of cosmic domains and strings. *J. Phys. A* **9**, 1387 (1976).

[18] T. W. B. Kibble, Some implications of a cosmological phase transition. *Phys. Rep.* **67**, 183 (1980).

[19] W. H. Zurek, Cosmological experiments in superfluid liquid helium? *Nature* **317**, 505 (1985).

[20] W. H. Zurek, Cosmological experiments in condensed matter systems. *Phys. Rep.* **276**, 177 (1996).

[21] G. Lamporesi, Simone Donadello, Simone Serafini, Franco Dalfovo and Gabriele Ferrari, Spontaneous creation of KibbleZurek solitons in a BoseEinstein condensate, *Nat. Phys.* **9**, 656 (2013).

[22] L. Chomaz *et al.*, Emergence of coherence via transverse condensation in a uniform quasi-two-dimensional Bose gas, *Nat. Commun.* **6**, 6162 (2014).

[23] N. Navon, Alexander L. Gaunt, Robert P. Smith and Zoran Hadzibabic, Critical dynamics of spontaneous symmetry breaking in a homogeneous Bose gas, *Science* **347**, 167 (2015).

[24] T. Kraemer et al., Evidence for Efimov quantum states in an ultracold gas of caesium atoms, *Nature* **440**, 315 (2006).

[25] S.-K. Tung, K. Jimnez-Garca, J. Johansen, C. V. Parker, and C. Chin, Geometric Scaling of Efimov States in a Li6-Cs133 Mixture, *Phys. Rev. Lett.* **113**, 240402 (2014).

[26] V. Efimov, Energy levels arising from resonant two-body forces in a three-body system, *Phys. Lett. B* **33**, 563 (1970).

[27] S. E. Pollack, D. Dries, and R. G. Hulet, Universality in Three- and Four-Body Bound States of Ultracold Atoms, *Science* **326**, 1683 (2009).

[28] N. Gross, Z. Shotan, S. Kokkelmans, and L. Khaykovich, Observation of Universality in Ultracold Li7 Three-Body Recombination, *Phys. Rev. Lett.* **103**, 163202 (2009).

[29] M. Zaccanti, B. Deissler, C. D'Errico, M. Fattori, M. Jona-Lasinio, S. Mller, G. Roati, M. Inguscio, and G. Modugno, Observation of an Efimov spectrum in an atomic system, *Nat. Phys.* **5**, 586 (2009).

[30] R. J. Wild, P. Makotyn, J. M. Pino, E. A. Cornell, and D. S. Jin, Measurements of Tans Contact in an Atomic Bose-Einstein Condensate, *Phys. Rev. Lett.* **108**, 145305 (2012).

[31] M. Berninger, A. Zenesini, B. Huang, W. Harm, H.-C. Nägerl, F. Ferlaino, R. Grimm, P. S. Julienne, and J. M. Hutson, Universality of the Three-Body Parameter for Efimov States in Ultracold Cesium, *Phys. Rev. Lett.* **107**, 120401 (2011).

[32] B. Huang, L. A. Sidorenkov, R. Grimm, and J. M. Hutson, Observation of the Second Triatomic Resonance in Efimovs Scenario, *Phys. Rev. Lett.* **112**, 190401 (2014).

[33] T. B. Ottenstein, T. Lompe, M. Kohnen, A. N. Wenz, and S. Jochim, Collisional Stability of a Three-Component Degenerate Fermi Gas, *Phys. Rev. Lett.* **101**, 203202 (2008).

[34] J. H. Huckans, J. R. Williams, E. L. Hazlett, R. W. Stites, and K. M. O'Hara, Three-Body Recombination in a Three-State Fermi Gas with Widely Tunable Interactions, *Phys. Rev. Lett.* **102**, 165302 (2009).

[35] P. Harper, *Proc. Phys. Soc. London Sect.* A **68**, 874 (1955).

[36] D. Hofstadter, Energy levels and wave functions of Bloch electrons in rational and irrational magnetic fields, *Phys. Rev. B* **14**, 2239 (1976).

[37] K.W. Madison, F. Chevy, W. Wohlleben, and J. Dalibard, Vortex Formation in a Stirred Bose-Einstein Condensate, *Phys. Rev. Lett.* **84**, 806 (2000).

[38] J. R. Abo-Shaeer, C. Raman, J. M. Vogels, and W. Ketterle, Observation of Vortex Lattices in Bose-Einstein Condensates, *Science* **292**, 476 (2001).

[39] Y.-J. Lin, R. L. Compton, K. Jiménez-García, J. V. Porto, and I. B. Spielman, Synthetic magnetic fields for ultracold neutral atoms, *Nature* **462**, 628 (2009).

[40] J. Dalibard, F. Gerbier, G. Juzeliūnas, and P. Öhberg, *Colloquium*: Artificial gauge potentials for neutral atoms, *Rev. Mod. Phys.* **83**, 1523 (2011).

[41] J. Struck *et al.*, Quantum simulation of frustrated classical magnetism in triangular optical lattices, *Science* **333**, 996 (2011).

[42] M. Aidelsburger, M. Atala, S. Nascimbéne, S. Trotzky, Y.-A. Chen, and I. Bloch, Experimental Realization of Strong Effective Magnetic Fields in an Optical Lattice, *Phys. Rev. Lett.* **107**, 255301 (2011).

[43] H. Miyake, G. A. Siviloglou, C. J. Kennedy, W. C. Burton, and W. Ketterle, Realizing the Harper Hamiltonian with Laser-Assisted Tunneling in Optical Lattices, *Phys. Rev. Lett.* **111**, 185302 (2013).

[44] M. Aidelsburger, M. Atala, M. Lohse, J. T. Barreiro, B. Paredes, and I. Bloch, Realization of the Hofstadter Hamiltonian with Ultracold Atoms in Optical Lattices, *Phys. Rev. Lett.* **111**, 185301 (2013).

[45] D. Jaksch, C. Bruder, J. I. Cirac, C. W. Gardiner, and P. Zoller, Cold Bosonic Atoms in Optical Lattices, *Phys. Rev. Lett.* **81**, 3108 (1998).

[46] M. Greiner, O. Mandel, T. Esslinger, T. W. Hänsch and I. Bloch, Quantum phase transition from a superfluid to a Mott insulator in a gas of ultracold atoms, *Nature* **415**, 39 (2002).

[47] M. Greiner, O. Mandel, T. W. Hänsch and Immanuel Bloch, Collapse and revival of the matter wave field of a BoseEinstein condensate, *Nature* **419**, 51 (2002).

[48] N. Gemelke, X. Zhang, C.-L. Hung and C. Chin, In situ observation of incompressible Mott-insulating domains in ultracold atomic gases, *Nature* **460**, 995 (2009).

[49] M. Girardeau, Relationship between systems of impenetrable bosons and fermions in one dimension, *J. Math. Phys.* **1**, 516523 (1960).

[50] E. H. Lieb and W. Liniger, Exact analysis of an interacting Bose gas. The general solution and the ground state, *Phys. Rev.* **130**, 1605 (1963).

[51] Belén Paredes et al., Tonks-Girardeau gas of ultracold atoms in an optical lattice, *Nature* **429**, 277 (2004).

[52] T. Kinoshita, Trevor Wenger and David S. Weiss, Observation of a One-Dimensional Tonks-Girardeau Gas, *Science* **305**, 1125 (2004).

[53] C.-L. Hung, X. Zhang, N. Gemelke, and C. Chin, Observation of scale invariance and universality in two-dimensional Bose gases, *Nature* **470**, 236 (2011).

[54] J. H. Denschlag et al., A Bose-Einstein condensate in an optical lattice, *J. Phys. B: At. Mol. Opt. Phys.* **35**, 3095 (2002).

[55] N. Gemelke, E. Sarajlic, Y. Bidel, S. Hong, and S. Chu, Parametric amplification of matter waves in periodically translated optical lattices. *Phys. Rev. Lett.* **95**, 170404 (2005).

[56] H. Lignier *et al.*, Dynamical control of matter-wave tunneling in periodic potentials. *Phys. Rev. Lett.* **99**, 220403 (2007).

[57] J. Struck *et al.*, Engineering ising-xy spin-models in a triangular lattice using tunable artificial gauge fields. *Nat. Phys.* **9**, 738 (2013).

[58] W. Ketterle, D. S. Durfee, D. M. Stamper-Kurn, Making, probing and understanding Bose-Einstein condensates, *arXiv:cond-mat/9904034*.

[59] S. N. Bose. Plancks Gesetz und Lichtquantenhypothese, *Z. Phys.*, *26*, 178, (1924).

[60] A. Einstein, Quantentheorie des einatomigen idealen Gases, *Sitz.ber. Preuss. Akad. Wiss.* 261, (1924).

[61] A. Einstein, Quantentheorie des einatomigen idealen Gases, *Sitz.ber. Preuss. Akad. Wiss.* 3, (1925).

[62] M. R. Andrews, C. G. Townsend, H.-J. Miesner, D. S. Durfee, D. M. Kurn, and W. Ketterle, Observation of Interference Between Two Bose Condensates, *Science* **275**, 637 (1997).

[63] C. J. Pethick and H. Smith, *Bose-Einstein Condensation in Dilute Gases* (Second Edition, Cambridge University Press, 2008).

[64] J. D. Plumhof, T. Stöferle, L. Mai, U. Scherf, and R. F. Mahrt, Room-temperature BoseEinstein condensation of cavity excitonpolaritons in a polymer, *Nat. Mater* **13**, 247 (2014).

[65] A. J. Kerman, *Raman Sideband Cooling and Cold Atomic Collisions in Optical Lattices*, PhD thesis (Stanford University 2005).

[66] J. J. Sakurai. *Modern Quantum Mechanics* (Addison Wesely, 1994).

[67] A. D. Lange, K. Pilch, A. Prantner, F. Ferlaino, B. Engeser, H.-C. Nägerl, R. Grimm, and C. Chin, Determination of atomic scattering lengths from measurements of molecular binding energies near Feshbach resonances, *Phys. Rev. A* **79**, 013622 (2009).

[68] V. L. Berezinskii, Destruction of long-range order in one-dimensional and two-dimensional system possessing a continuous symmetry group-II Quantum systems, *Zh. Eksp. Teor. Fiz.* **61**, 1144 (1971) [*Sov. Phys. JETP* **34**, 610 (1972)].

[69] J. M. Kosterlitz and D. J. Thouless, Ordering, metastability and phase transitions in two-dimensional systems, *J. Phys. C* **6**, 1181 (1973).

[70] V. N. Popov, *Theor. Math. Phys.* **11**, 565 (1972).

[71] N. Prokof'ev, O. Ruebenacker, and B. Svistunov, *Phys. Rev. Lett.* **87**, 270402 (2001).

[72] N. Prokof'ev and B. Svistunov, *Phys. Rev. A* **66**, 043608 (2002).

[73] G.-B. Jo, J. Guzman, C. K. Thomas, P. Hosur, A. Vishwanath, and D. M. Stamper-Kurn, Ultracold atoms in a tunable optical kagome lattice, *Physical Review Letters* **108**, 045305 (2012).

[74] S. A. Parameswaran, I. Kimchi, A. M. Turner, D. M. Stamper-Kurn, and A. Vishwanath, Wannier permanents and featureless bosonic Mott insulators on the 1/3 filled kagome lattice, *Physical Review Letters* **110**, 125301 (2013).

[75] N. W. Ashcroft and N. D. Mermin, *Solid State Physics* (Holt, Rinehart and Winston, 1976).

[76] R. Desbuquois *et al.*, Superfluid behaviour of a two-dimensional Bose gas, *Nat. Phys.* **8**, 645 (2012).

[77] F. Grossmann, T. Dittrich, P. Jung and P. Hänggi, Coherent Destruction of Tunneling, *Phys. Rev. Lett.* **67**, 516 (1997).

[78] E. L. Surkov, J. T. M. Walraven, and G. V. Shlyapnikov. Collisionless motion and evaporative cooling of atoms in magnetic traps. *Phys. Rev. A*, 53(5):3403, (1996).

[79] S. Stellmer, B. Pasquiou, R. Grimm, and F. Schreck, Laser Cooling to Quantum Degeneracy, *Phys. Rev. Lett.* **110**, 263003 (2013).

[80] A. J. Kerman, V. Vuletić, C. Chin, and S. Chu, Beyond Optical Molasses: 3D Raman Sideband Cooling of Atomic Cesium to High Phase-Space Density, *Phys. Rev. Lett.* **84**, 439 (2000).

[81] X. Zhang, *Observation of Quantum Criticality with Ultracold Atoms in Optical Lattices*, PhD thesis (The University of Chicago, 2012).

[82] S. Choudhury and E. J. Mueller, Stability of a Floquet Bose-Einstein condensate in a one-dimensional optical lattice, *Phys. Rev. A* **90**, 013621 (2014).

[83] S. Choudhury and E. J. Mueller, Transverse collisional instabilities of a Bose-Einstein condensate in a driven one-dimensional lattice, *Phys. Rev. A* **91**, 023624 (2015).

[84] S. E. Sebastian, N. Harrison, C. D. Batista, L. Balicas, M. Jaime, P. A. Sharma, N. Kawashima and I. R. Fisher, Geometric Frustration and Dimensional Reduction at a Quantum Critical Point, *Nature* **441**, 617 (2006).

[85] D. J. Bishop and J. D. Reppy, Study of the Superfluid Transition in Two-Dimensional He4 Films, *Phys. Rev. Lett.* **40**, 1727 (1978).

[86] A. I. Safonov, S. A. Vasilyev, I. S. Yasnikov, I. I. Lukashevich, and S. Jaakkola, Observation of Quasicondensate in Two-Dimensional Atomic Hydrogen, *Phys. Rev. Lett.* **81**, 4545 (1998).

[87] D. J. Resnick, J. C. Garland, J. T. Boyd, S. Shoemaker and R. S. Newrock, Kosterlitz-Thouless Transition in Proximity-Coupled Superconducting Arrays, *Phys. Rev. Lett.* **47**, 1542 (1981).

[88] J. Corson, R. Mallozzi, J. Orenstein, J. N. Eckstein and I. Bozovic, Vanishing of phase coherence in underdoped Bi2Sr2CaCu2O8+delta, *Nature* **398**, 221 (1999).

[89] Z. Hadzibabic, P. Krüger, M. Cheneau, B. Battelier, and J. Dalibard, BerezinskiiKosterlitzThouless crossover in a trapped atomic gas, *Nature* **441**, 1118 (2006).

[90] P. Cladé, C. Ryu, A. Ramanathan, K. Helmerson, and W. D. Phillips, Observation of a 2D Bose Gas: From Thermal to Quasicondensate to Superfluid, *Phys. Rev. Lett.* **102**, 170401 (2009).

[91] S.-K. Tung, G. Lamporesi, D. Lobser, L. Xia, and E. A. Cornell, *Phys. Rev. Lett.* **105**, 230408 (2010).

[92] G. E. Astrakharchik, J. Boronat, J. Casulleras, I. L. Kurbakov, and Yu. E. Lozovik, *Phys. Rev. A* **79**, 051602(R) (2009).

[93] A. Y. Cherny and A. A. Shanenko, *Phys. Rev. E* **64**, 027105 (2001).

[94] G. E. Astrakharchik, J. Boronat, I. L. Kurbakov, Yu. E. Lozovik, and F. Mazzanti, *Phys. Rev. A* **81**, 013612 (2010).

[95] C. Mora and Y. Castin, *Phys. Rev. Lett.* **102**, 180404 (2009).

[96] V. N. Popov, *Functional Integrals in Quantum Field Theory and Statistical Physics* (Reidel, Dordrecht, 1983).

[97] P. Krüger, Z. Hadzibabic, and J. Dalibard, *Phys. Rev. Lett.* **99**, 040402 (2007).

[98] S. Sachdev, *Phys. Rev. B* **59**, 14054 (1999).

[99] S. Sachdev and E. Demler, *Phys. Rev. B* **69**, 144504 (2004).

[100] We derive G starting from the scaled superfluid density $\tilde{n} = (6g/\mathcal{G} + \tilde{\mu})\pi/g + 2\pi F(\mathcal{G})$; see Eq. (A6) in Ref. [99]. We then use the following approximations; $\mathcal{G} \approx 6g\exp((1 + \pi/g)\tilde{\mu})/\tilde{\mu} \gg 1$ and $F(\mathcal{G}) \approx (\ln\mathcal{G})/2\pi \approx (1 + \frac{\pi}{g})\tilde{\mu}/2\pi$, in the superfluid limit and obtain $\tilde{n} = (1 + 2\pi/g)\tilde{\mu}$, or equivalently $G = 2\pi g/(2\pi + g)$.

[101] A. Rançon and N. Dupuis, *Phys. Rev. A* **85**, 063607 (2012).

[102] A. Rançon (private communication). The formula is an empirical fit to the numerical calculation within the range of our interaction strength.

[103] D. S. Petrov, M. Holzmann, and G. V. Shlyapnikov, *Phys. Rev. Lett.* **84**, 2551 (2000).

[104] S. Sachdev and E. R. Dunkel, *Phys. Rev. B* **73**, 085116 (2006).

[105] We include the logarithmic correction in the determination of g according to Refs. [103, 104].

[106] X. Zhang, C.-L. Hung, S.-K. Tung, and C. Chin, *Science* **335**, 1070 (2012).

[107] M. Schick, *Phys. Rev. A* **3**, 1067 (1971).

[108] C. Chin, V. Vuletić, A. J. Kerman, S. Chu, E. Tiesinga, P.J. Leo and C.J. Williams, *Phys. Rev. A* **70**, 032701 (2004).

[109] C.-L. Hung, X. Zhang, N. Gemelke, and C. Chin, *Phys. Rev. Lett.* **104**, 160403 (2010).

[110] For most experiments, atom loss is less than 5%. For 2D gases with $a = 500$ and $580\,a_0$, $g = 0.7$ and 0.8 respectively, the loss is $10 - 20\%$ in the first 100 ms.

[111] C.-L. Hung, X. Zhang, L.-C. Ha, S.-K. Tung, N. Gemelke, and C. Chin, *New J. Phys.* **13**, 075019 (2011).

[112] T.-L. Ho and Q. Zhou, *Nat. Phys.* **6**, 131 (2010).

[113] T. Yefsah, R. Desbuquois, L. Chomaz, K. J. Günter, and J. Dalibard, *Phys. Rev. Lett.* **107**, 130401 (2011).

[114] Throughout this chapter, we present our measurements in dimensionless form, but we do not assume scale invariance.

[115] M. S. Mashayekhi, J.-S. Bernier, D. Borzov, J.-L. Song, and F. Zhou, *Phys. Rev. Lett.* **110**, 145301 (2013).

[116] For g smaller than 1.5, the range used for overlapping is $|\tilde{\mu} - \tilde{\mu}_{\rm c}|/G_{\rm c} \leq 1.5$. For g larger than 1.5, it is $|\tilde{\mu} - \tilde{\mu}_{\rm c}|/G_{\rm c} \leq 1.0$.

[117] L. Xing, *Phys. Rev. B* **42**, 8426 (1990).

[118] Z. Hadzibabic, P. Krüger, M. Cheneau, S. P. Rath, and J. Dalibard, *New J. Phys.* **10**, 045006 (2008).

[119] X. Zhang, C.-L. Hung, S.-K. Tung, N. Gemelke, and Cheng Chin, *New J. Phys.* **13**, 045011 (2008).

[120] J. Stenger *et al.*, Spin domains in ground-state Bose-Einstein condensates. *Nature* **396**, 345 (1998).

[121] L. E. Sadler, J. M. Higbie, S. R. Leslie, M. Vengalattore and D. M. Stamper-Kurn, Spontaneous symmetry breaking in a quenched ferromagnetic spinor Bose-Einstein condensate. *Nature* **443**, 312 (2006).

[122] H. Schmaljohann *et al.* Dynamics of $F = 2$ spinor Bose-Einstein condensates. *Phys. Rev. Lett.* **92**, 040402 (2004).

[123] M.-S. Chang, Q. Qin, W. Zhang, L. You, and M. S. Chapman, Coherent spinor dynamics in a spin-1 Bose condensate. *Nat. Phys.* **1**, 111 (2005).

[124] D. M. Stamper-Kurn and M. Ueda, Spinor Bose gases: Symmetries, magnetism, and quantum dynamics. *Rev. Mod. Phys.* **85**, 1191 (2013).

[125] M. Vengalattore, S. R. Leslie, J. Guzman, and D. M. Stamper-Kurn, Spontaneously modulated spin textures in a dipolar spinor Bose-Einstein condensate. *Phys. Rev. Lett.* **100**, 170403 (2008).

[126] J. Kronjäger, C. Becker, P. Soltan-Panahi, K. Bongs and K. Sengstock, Spontaneous pattern formation in an antiferromagnetic quantum gas. *Phys. Rev. Lett.* **105**, 090402 (2010).

[127] A. Vinit, E. M. Bookjans, C. A. R. S. de Melo and C. Raman, Antiferromagnetic spatial ordering in a quenched one-dimensional spinor gas. *Phys. Rev. Lett.* **110**, 165301 (2013).

[128] T.-L. Ho, Spinor Bose condensates in optical traps. *Phys. Rev. Lett.* **81**, 742 (1998).

[129] T. Ohmi and K. Machida, Bose-Einstein condensation with internal degrees of freedom in alkali atom gases. *J. Phys. Soc. Jpn.* **67**, 1822 (1998).

[130] J. Guzman *et al.*, Long-time-scale dynamics of spin textures in a degenerate $F = 1$ ^{87}Rb spinor bose gas. *Phys. Rev. A* **84**, 063625 (2011).

[131] K. Baumann, C. Guerlin, F. Brennecke, and T. Esslinger, Dicke quantum phase transition with a superfluid gas in an optical cavity. *Nature* **464**, 1301 (2010).

[132] J. Simon *et al.*, Quantum simulation of antiferromagnetic spin chains in an optical lattice. *Nature* **472**, 307 (2011).

[133] P. Soltan-Panahi *et al.*, Multi-component quantum gases in spin-dependent hexagonal lattices. *Nat. Phys.* **7**, 434 (2011).

[134] G.-B. Jo *et al.*, Ultracold atoms in a tunable optical kagome lattice. *Phys. Rev. Lett.* **108**, 045305 (2012).

[135] G. Wirth, M. Ölschläger, and A. Hemmerich, Evidence for orbital superfluidity in the p-band of a bipartite optical square lattice. *Nat. Phys.* **7**, 147 (2011).

[136] J. Struck *et al.*, Tunable gauge potential for neutral and spinless particles in driven optical lattices. *Phys. Rev. Lett.* **108**, 225304 (2012).

[137] Y.-J. Lin, K. Jiménez-García and I. B. Spielman, Spin-orbit-coupled Bose-Einstein condensates. *Nature* **471**, 83 (2011).

[138] C. Wang, C. Gao, C.-M. Jian, and H. Zhai, Spin-orbit coupled spinor Bose-Einstein condensates. *Phys. Rev. Lett.* **105**, 160403 (2010).

[139] T.-L. Ho and S. Zhang, Bose-Einstein condensates with spin-orbit interaction. *Phys. Rev. Lett.* **107**, 150403 (2011).

[140] B. J. Dalton and S. Ghanbari, Two mode theory of Bose–Einstein condensates: interferometry and the josephson model. *Journal of Modern Optics* **59**, 287 (2011).

[141] X. Zhang, C.-L. Hung, S.-K. Tung and C. Chin, Observation of quantum criticality with ultracold atoms in optical lattices. *Science* **335**, 1070 (2012).

[142] R. Shankar, Renormalization-group approach to interacting fermions. *Rev. Mod. Phys.* **66**, 129 (1994).

[143] C.-L. Hung, X. Zhang, N. Gemelke and C. Chin, Accelerating evaporative cooling of atoms into Bose-Einstein condensation in optical traps. *Phys. Rev. A* **78**, 011604 (2008).

[144] L. D. Landau. The theory of superfluidity of Helium II. *J. Phys. USSR* **5**, 71 (1941).

[145] L. D. Landau. On the theory of supefluidity of Helium II. *J. Phys. USSR* **11**, 91 (1947).

[146] D. G. Henshaw and A. D. B. Woods, Modes of Atomic Motions in Liquid Helium by Inelastic Scattering of Neutrons, *Phys. Rev.* **121**, 1266 (1961).

[147] H. R. Glyde, *Excitations in Liquid and Solid Helium* (Clarendon, 1994).

[148] T. Schneider and C. P. Enz, Theory of the Superfluid-Solid Transition of He4, *Phys. Rev. Lett.* **27**, 1186 (1971).

[149] L. Santos, G. V. Shlyapnikov and M. Lewenstein, Roton-Maxon Spectrum and Stability of Trapped Dipolar Bose-Einstein Condensates, *Phys. Rev. Lett.* **90**, 250403 (2003).

[150] R. M. Wilson, S. Ronen, J. L. Bohn, and H. Pu, Manifestations of the Roton Mode in Dipolar Bose-Einstein Condensates, *Phys. Rev. Lett.* **100**, 245302 (2008).

[151] D. H. J. O'Dell, S. Giovanazzi, and G. Kurizki, Rotons in Gaseous Bose-Einstein Condensates Irradiated by a Laser, *Phys. Rev. Lett.* **90**, 110402 (2003).

[152] N. Henkel, R. Nath, and T. Pohl, Three-Dimensional Roton Excitations and Supersolid Formation in Rydberg-Excited Bose-Einstein Condensates, *Phys. Rev. Lett.* **104**, 195302 (2010).

[153] Y. Yunomae, D. Yamamoto, I. Danshita, N. Yokoshi, and S. Tsuchiya, *Phys. Rev. A* **80**, 063627 (2009); S. C. Cormack, D. Schumayer, and D. A. W. Hutchinson, *Phys. Rev. Lett.* **107**, 140401 (2011); R. Rota, F. Tramonto, D. E. Galli, and S. Giorgini, Phys. Rev. B. **88**, 214505 (2013).

[154] U. R. Fischer, Stability of quasi-two-dimensional Bose-Einstein condensates with dominant dipole-dipole interactions, *Phys. Rev. A* **73**, 031602(R) (2006).

[155] F. S. Nogueira and H. Kleinert, Thermally induced rotons in two-dimensional dilute Bose gases, *Phys. Rev. B.* **73**, 104515 (2006).

[156] R. W. Cherng and E. Demler, Magnetoroton Softening in Rb Spinor Condensates with Dipolar Interactions, *Phys. Rev. Lett.* **103**, 185301 (2009).

[157] M. Matuszewski, Rotonlike Instability and Pattern Formation in Spinor Bose-Einstein Condensates, *Phys. Rev. Lett.* **105**, 020405 (2010).

[158] J. Higbie and D. M. Stamper-Kurn, Periodically Dressed Bose-Einstein Condensate: A Superfluid with an Anisotropic and Variable Critical Velocity, *Phys. Rev. Lett.* **88**, 090401 (2002).

[159] W. Zheng and Z. Li, Phys. Rev. A **85**, 053607 (2012); G. I. Martone, Y. Li, L. P. Pitaevskii, and S. Stringari, *Phys. Rev. A* **86**, 063621 (2012); W. Zheng, Z.-Q. Yu, X. Cui, and H. Zhai, J. Phys. B: At. Mol. Opt. Phys. **46**, 134007 (2013).

[160] R. Mottl, F. Brennecke, K. Baumann, R. Landig, T. Donner, and T. Esslinger, Roton-Type Mode Softening in a Quantum Gas with Cavity-Mediated Long-Range Interactions, *Science* **336**, 1570 (2012).

[161] C. V. Parker, L.-C. Ha, and C. Chin, Direct observation of effective ferromagnetic domains of cold atoms in a shaken optical lattice, *Nat. Phys.* **9**, 769 (2013).

[162] G. Jotzu *et al.*, Experimental realization of the topological Haldane model with ultracold fermions, *Nature* **515**, 237 (2014).

[163] L. W. Cheuk, A. T. Sommer, Z. Hadzibabic, T. Yefsah, W. S. Bakr, and M. W. Zwierlein, Spin-Injection Spectroscopy of a Spin-Orbit Coupled Fermi Gas, *Phys. Rev. Lett.* **109**, 095302 (2012).

[164] C. Hamner *et al.*, Dicke-type phase transition in a spin-orbit-coupled BoseEinstein condensate, *Nat. Comm.* **5**, 4023 (2014).

[165] S.-C. Ji *et al.*, Experimental determination of the finite-temperature phase diagram of a spinorbit coupled Bose gas, *Nat. Phys.* **10**, 314 (2014).

[166] Z. Fu *et al.*, Production of Feshbach molecules induced by spinorbit coupling in Fermi gases, *Nat. Phys.* **10**, 110 (2014).

[167] A. Eckardt, P. Hauke, P. Soltan-Panahi, C. Becker, K. Sengstock, and M. Lewenstein, Frustrated quantum antiferromagnetism with ultracold bosons in a triangular lattice, *Europhys. Lett.* **89**, 10010 (2010).

[168] R. Ozeri, N. Katz, J. Steinhauer, and N. Davidson, *Colloquium*: Bulk Bogoliubov excitations in a Bose-Einstein condensate, *Rev. of Mod. Phys.* **77**, 187 (2005).

[169] W. Zheng, B. Liu, J. Miao, C. Chin and H. Zhai, Strong Interaction Effects and Criticality of Bosons in Shaken Optical Lattices, *Phys. Rev. Lett.* **113**, 155303 (2014).

[170] D. E. Miller *et al.*, Critical Velocity for Superfluid Flow across the BEC-BCS Crossover, *Phys. Rev. Lett.* **99**, 070402 (2007).

[171] C. Raman, M. Köhl, R. Onofrio, D. S. Durfee, C. E. Kuklewicz, Z. Hadzibabic, and W. Ketterle, Evidence for a Critical Velocity in a Bose-Einstein Condensed Gas, *Phys. Rev. Lett.* **83**, 2502 (1999).

[172] R. Onofrio, C. Raman, J. M. Vogels, J. R. Abo-Shaeer, A. P. Chikkatur, and W. Ketterle, Observation of Superfluid Flow in a Bose-Einstein Condensed Gas, *Phys. Rev. Lett.* **85**, 2228 (2000).

[173] T. Winiecki, B. Jackson, J. F. McCann, and C. S. Adams, Vortex shedding and drag in dilute Bose-Einstein condensates, *J. Phys. B* **33**, 4069 (2000).

[174] T. Frisch, Y. Pomeau, and S. Rica, Transition to dissipation in a model of superflow, *Phys. Rev. Lett.* **69**, 1644 (1992).

[175] J. S. Stießberger and W. Zwerger, Critcal velocity of superfluid flow past large obstacles in Bose-Einstein condensates, *Phys. Rev. A* **62**, 061601(R) (2000).

[176] G. Baym and C. J. Pethick, Landau critical velocity in weakly interacting Bose gases, *Phys. Rev. A* **86**, 023602 (2012).

[177] L. P. Pitaevskii, Layered Structure of Superfluid He4 with Supercritical Motion, *Pis'ma Zh. Eksp. Teor. Fiz.* **39**, 423 (1984) [*JETP Lett.* **39**, 511 (1984)].

[178] P. Noziéres, Is the Roton in Superfluid 4He the Ghost of a Bragg Spot?, *JLPT* **137**, 45 (2004).

[179] H. Kadau, M. Schmitt, M. Wenzel, C. Wink, T. Maier, I. Ferrier-Barbut, and T. Pfau, Observing the Rosensweig instability of a quantum ferrofluid, *Nature* **530**, 194 (2016).